THESIS

Presented and publicly supported for obtaining the degree of

DOCTOR from the **UNIVERSITY OF LILLE**

in Acoustics

DOCTOR from the **KU LEUVEN**

in Physics

by

Ravi VERMA

defended on December 20, 2023

Thesis title:

Interaction of ultrasonic waves with frictional defects in the context of nondestructive testing of materials

Committee members:

Supervisors:	Dr Vladislav Aleshin	CNRS researcher, IEMN, Lille
	Dr. Koen Van Den Abeele	Professor, KU Leuven, Kortrijk
President:	Dr. Nathalie Favretto-Cristini	CNRS Research Director, LMA, Marseille
Reviewers:	Dr. Cédric Payan	Professor, LMA, Marseille
	Dr. Mourad Bentahar	Associate professor, Le Mans University, Le Mans
Examiner:	Dr. Christ Glorieux	Professor, KU Leuven, Kortrijk
Invited:	Dr. Olivier Bou Matar	Professor, Central Lille, Lille
	Dr. Mathias Kersemans	Professor, Ghent University, Ghent

THÈSE

Présentée et soutenue publiquement pour l'obtention du grade de

DOCTEUR DE **L'UNIVERSITE DE LILLE**

en Acoustique

DOCTEUR DE **KU LEUVEN**

en Physique

par

Ravi VERMA

soutenue le 20 Décembre, 2023

Titre de la thèse:

Interaction des ondes ultrasonores avec les défauts de frottement dans le contexte du contrôle non destructif des matériaux

Composition du jury:

Directeur de these:	Dr Vladislav Aleshin	Chercheur CNRS, IEMN, Lille
	Dr. Koen Van Den Abeele	Professeur, KU Leuven, Courtrai
Présidente:	Dr. Nathalie Favretto-Cristini	Directrice de Recherche CNRS, LMA, Marseille
Rapporteurs:	Dr. Cédric Payan	Professeur, LMA, Marseille
	Dr. Mourad Bentahar	Maître de conférences, Le Mans Université
Examinateurs:	Dr. Christ Glorieux	Professeur, KU Leuven, Courtrai
Invité:	Dr. Olivier Bou Matar	Professeur, École Centrale Lille, Lille
	Dr. Mathias Kersemans	Professeur, Université Gent

THESIS

Voorgelegd en openbaar gepresenteerd voor het behalen van de graad

van DOCTOR van de **UNIVERSITEIT VAN LILLE**

in Akoestiek

DOCTOR **KU LEUVEN**

in de Wetenschappen: Natuurkunde

door

Ravi VERMA

verdedigd op 20 december, 2023

Titel proefschrift:

Interactie van ultrasone golven met wrijvingsdefecten in de context van niet-destructief materiaalonderzoek

Samenstelling van de jury:

Directeur onderzoek:	Dr Vladislav Aleshin	Onderzoeker CNRS, IEMN, Lille
	Dr. Koen Van Den Abeele	Gewoon Hoogleraar KU Leuven, Kortrijk
Voorzitter:	Dr. Nathalie Favretto-Cristini	CNRS Onderzoeksdirecteur, LMA, Marseille
Rapporteurs:	Dr. Cédric Payan	Hoogleraar, LMA, Marseille
	Dr. Mourad Bentahar	Universitair hoofddocent, Universiteit van Le Mans
Examinatoren:	Dr. Christ Glorieux	Hoogleraar KU Leuven, Kortrijk
Invité:	Dr. Olivier Bou Matar	Hoogleraar, École Centrale Lille, Lille
	Dr. Mathias Kersemans	Hoogleraar, Universiteit Gent

University of Lille

Doctoral school: Engineering and Systems Sciences
Department: Micro/nano/biosystems, Waves, and Microfluidics Department
Research unit: Institute of Electronics Microelectronics and Nanotechnology (IEMN – UMR 8520)
59650 Villeneuve-d'Ascq, France

KU Leuven (Katholieke Universiteit Leuven)

Doctoral school: Arenberg Doctoral School
Department: Department of physics
Research unit: Wave Propagation and Signal Processing Research Group KU Leuven Kulak
8500 Kortrijk, Belgium

Initiatives–Science Innovation Territories Economy (I-SITE)

University of Lille North-Europe (ULNE)

National Center for Scientific Research (Centre national de la recherche scientifique) - CNRS

IEMN – CENTRAL LABORATORY OF THE INSTITUTE
Cité Scientifique
Avenue Henri Poincaré
CS 60069
59 652 Villeneuve d'Ascq Cedex, France

In memory of my grandmother "अम्मा."

To my beloved parents and my uncle

Acknowledgements

This endeavor has become significantly more achievable due to the invaluable contributions of two remarkable individuals: Dr. Vladislav Aleshin and Prof. Dr. Koen Van Den Abeele. Their exceptional guidance and unwavering encouragement have left an indelible mark on this undertaking, and for their exceptional contributions, I extend my profound gratitude, which knows no bounds.

I extend my profound appreciation to the National Center for Scientific Research (Centre national de la recherche scientifique, CNRS) and the governing bodies of Initiatives for Science, Innovation, Territories, and Economy (I-SITE) for their generous financial support, which sustained my entire doctoral journey.

I reserve a special place of gratitude for the dedicated members of the IEMN laboratory for their steadfast assistance and support. I must acknowledge my exceptional colleagues, with whom I have cherished camaraderie, engaged in enlightening conversations, and shared hearty laughter. Our profound discussions, dedicated to tackling global challenges, have enriched my understanding in countless ways. My heart brims with profound gratitude towards cherished friends scattered across the globe, whose love and blessings have been a constant source of solace. I deeply value the friendships that blossomed with my colleagues from the IEMN laboratory, particularly Samir Al Mohammad and Ravindra Chutani, as we shared delightful moments over chai, lunch, and festive celebrations. Other colleagues, namely Andrea Cannizzo, Claudia Binetti, Jon Canosa Diaz, and Pinar Eribol, also left a lasting impact on my life by becoming friends.

I wish to express my deep appreciation to Dr. Pushpendra Kumar at Graphic Era (deemed to be university), Dehradun, India, and Dr. Subhash Singh at the National Institute of Technology Jamshedpur, India, for their invaluable suggestions and motivating guidance.

Friends from Lille city had a positive influence on my journey, standing by me in every good phase. I want to express my special thanks to Nagesh N. Prasad, Laila Ali, Gaurav Maheshwari, Rahul Kumar, Prakrit Saxena, Sahil Gehlawat, Ayush K. Singh, Chandan Kumar, and Anil P. Mohanan. I also had the pleasure of meeting a lovely couple who turned out to be my local guardians, named Laurent Quentin and Moy Lim.

Lastly, I extend my deepest gratitude to my family, who have been my unwavering source of support, boundless love, and enduring affection. A special acknowledgment goes to my sister, Poonam Verma, a constant pillar of support in all my decisions. Greetings to my beloved people, Babita Kukreti and Rakhi Kapruwan-Shiv Kapruwan – you transcend friendship; you

are my chosen family! The biggest support came from my brother-in-law, Tarun Garg, and my childhood friend, Sachin Sharma, for their invaluable support through their presence, filling the gap in my absence with my parents. From the very core of my being, I appreciate their role as an unending wellspring of inspiration, courage, and continuity. Every family member has played a significant role in shaping my journey, and I am grateful for their contributions. As a final note, in the face of life's trials, solace found its haven in the remarkable Monika, the lady who holds the key to my heart.

Abstract

This thesis concerns theoretical concepts, models, and experiments for elastic wave propagation and vibrations in solids containing internal contacts (cracks, delaminations, etc.) having frictional nature. The study is oriented to nondestructive testing and therefore focuses on the case where the material contains few cracks of known configuration, in contrast to microcracked solids in which a statistical ensemble of a large number of internal contacts is present.

An essential part of the work is related to a development of a method of numerical acoustics capable of imitating elastic waves in an environment containing frictional cracks/contacts. These planar defects represent a sort of inner boundaries at which appropriate boundary conditions should be set. Depending on modeling hypotheses, crack surfaces can be considered as plane or rough. Here we elaborate in detail arguments showing that roughness, although introducing additional complexification, finally results in a more compact and elegant description in comparison to plane interfaces. In particular, contact of isotropically rough surfaces can be effectively represented as contact between two axisymmetric bodies. The latter situation closely resembles Cattaneo-Mindlin (or Hertz-Mindlin) mechanics in which two spheres are mechanically excited with certain normal and tangential forces.

In the purpose of establishing boundary conditions at crack faces, the Cattaneo-Mindlin solution has been recently revisited to take into account non-spherical (but axisymmetric contact shapes) and excitation with non-constant but arbitrarily varying in time oblique action. The formulated load-displacement relationship for equivalent axisymmetric bodies is also approximately valid for rough surfaces and represents a sought-for boundary condition.

Another component of the numerical acoustics model we present here is a standard finite element description for elastic waves in solid materials (solid mechanics unit in commercial FEM packages). Technical efforts have been made to integrate a user-defined contact model as a boundary condition into the solid mechanics unit. As a result, a complete model has been obtained that incorporates wave-induced contact frictional interactions described starting from first principles of contact mechanics.

An essential progress in comparison to previous works is related to application of the elaborated model to a case that corresponds to a known technique of nonlinear acoustic nondestructive testing. The chosen technique is based on excitation of a sample with a harmonic wave that, after completion of a transient regime, results in a purely harmonic response if the sample is intact, whereas the response of a damaged one presents

anharmonicity. The generated harmonics form their own stationary wave pattern that can have a pronounced maximum around the defect. In practice, surface signal measurements are done via laser vibrometry; our modeling therefore represents an attempt to imitate the laser vibrometry NDT experiment in geometrically simplified conditions, but fully adhering to its concept.

The simplified geometry is chosen in the sake of reducing the computational effort. The most important assumption is a 2D geometry that immediately disables a quantitative comparison to experiment. Other simplifications are discussed below in greater detail. Keeping, however, the general methodology close to experimental principles, we generate a large number of synthetic nonlinear images of an isolated crack immersed into a fragment of a solid plate. We analyze in detail the influence of geometric and physical parameters of the system in the cases of single- and dual-frequency excitations. Depending on these parameters, the result of imaging procedure can range from complete success (the crack position and extent is clearly identified) to total failure (not crack is visible in an image consisting of a sequence of maxima at wrong positions). Successes and failures are consequences of a complex pattern of the nonlinear stationary waves emitted by the crack being an object with highly nonlinear mechanical properties.

Finally, we focus on the case close to real experimental conditions in terms of the sample geometry and boundary conditions selected. A preliminary qualitative theory and experiment comparison is presented.

Generally, the results of this thesis could be of interest for researchers involved in nonlinear acoustic NDT experiments as well as for those who look for applications of modern semi-analytical contact models based on Cattaneo-Mindlin principles.

Résumé

Cette thèse porte sur les concepts théoriques, les modèles et les expériences concernant la propagation des ondes élastiques et les vibrations dans les solides contenant des contacts internes (fissures, délamina**ge**s, etc.) ayant une nature frictionnelle. L'étude est orientée vers le contrôle non destructif et se concentre donc sur le cas où le matériau contient peu de fissures de configuration connue, contrairement aux solides microfissurés dans lesquels un ensemble statistique d'un grand nombre de contacts internes est présent.

Une partie essentielle du travail est liée au développement d'une méthode d'acoustique numérique capable d'imiter les ondes élastiques dans un environnement contenant des fissures/contacts à frottement. Ces défauts planaires représentent une sorte de frontière intérieure à laquelle il convient de fixer des conditions aux limites appropriées. Selon les hypothèses de modélisation, les surfaces des fissures peuvent être considérées comme planes ou rugueuses. Nous développons ici en détail les arguments montrant que la rugosité, bien qu'elle introduise une complexification supplémentaire, aboutit finalement à une description plus élégante du contact par rapport aux interfaces planes. En particulier, le contact de surfaces rugueuses isotropes peut être représenté efficacement comme un contact entre deux corps axisymétriques. Cette dernière situation ressemble beaucoup à la mécanique de Cattaneo-Mindlin (ou Hertz-Mindlin) dans laquelle deux sphères sont excitées mécaniquement par une force oblique.

Dans le but d'établir des conditions aux limites aux faces des fissures, la solution de Cattaneo-Mindlin a été récemment revisitée pour prendre en compte les formes de contact non sphériques (mais axisymétriques) et l'excitation avec une action oblique non constante mais variant arbitrairement dans le temps. La relation charge-déplacement formulée pour des corps axisymétriques équivalents est également approximativement valable pour les surfaces rugueuses et représente une condition aux limites recherchée.

Une autre composante du modèle acoustique numérique que nous présentons ici est une description standard par éléments finis des ondes élastiques dans les matériaux solides (unité de mécanique des solides dans les logiciels FEM commercials). Des efforts techniques ont été faits pour intégrer un modèle de contact défini par l'utilisateur comme condition aux limites dans l'unité de mécanique des solides. On a ainsi obtenu un modèle complet qui incorpore les interactions de frottement de contact induites par les ondes et décrites à partir des premiers principes de la mécanique des contacts.

Un progrès essentiel par rapport aux travaux précédents est lié à l'application du modèle élaboré à un cas qui correspond à une technique connue d'essais non destructifs acoustiques non linéaires. La technique choisie est basée sur l'excitation d'un échantillon avec une onde harmonique qui, après l'achèvement d'un régime transitoire, donne une réponse purement harmonique si l'échantillon est intact, alors que la réponse d'un échantillon endommagé présentera une anharmonicité. Les harmoniques générées forment leur propre modèle d'onde stationnaire qui peut avoir un maximum prononcé autour du défaut. Dans la pratique, les mesures de signaux de surface sont effectuées par vibrométrie laser ; notre modélisation représente donc une tentative d'imiter l'expérience de contrôle non destructif par vibrométrie laser dans des conditions géométriques simplifiées, mais en adhérant pleinement à son idéologie.

Les conditions simplifiées sont prises de manière à réduire le temps de calcul. L'hypothèse la plus importante est une géométrie en 2D qui empêche immédiatement toute comparaison quantitative avec l'expérience. D'autres simplifications sont discutées plus en détail ci-dessous. Tout en conservant la méthodologie générale proche des principes expérimentaux, nous générons un grand nombre d'images synthétiques non linéaires d'une fissure isolée immergée dans un fragment d'une plaque solide. Nous analysons en détail l'influence des paramètres géométriques et physiques du système dans les cas d'excitations à une ou deux fréquences. Parfois, nous voyons clairement la fissure dans ces images et parfois non ; nous avons essayé de fournir une interopération adéquate de ces situations qui découle du fait que le modèle d'onde stationnaire ainsi qu'un diagramme de rayonnement non linéaire d'une fissure peuvent avoir une structure complexe.

Enfin, nous nous concentrons sur le cas le plus proche des conditions expérimentales réelles en termes de géométrie de l'échantillon et de conditions aux limites sélectionnées. Une comparaison préliminaire entre la théorie et l'expérience est présentée.

D'une manière générale, les résultats de cette thèse pourraient intéresser les chercheurs impliqués dans les expériences de CND acoustique non linéaire ainsi que ceux qui recherchent des applications de modèles de contact semi-analytiques modernes basés sur les principes de Cattaneo-Mindlin.

Samenvatting

Dit proefschrift heeft betrekking op theoretische concepten, modellen en experimenten voor elastische golfvoortplanting en trillingen in vaste stoffen die interne contacten (scheuren, delaminaties, enz.) bevatten, gekenmerkt door wrijving. De studie focust zich op niet-destructief onderzoek en richt zich daarom op het geval waarin het materiaal slechts enkele scheuren bevat in een bekende configuratie. Dit in tegenstelling tot microscheuren in vaste stoffen waarin een statistisch ensemble van een groot aantal interne contacten aanwezig is.

Een essentieel deel van het werk is gerelateerd aan de ontwikkeling van een numerieke akoestisch model dat in staat is om elastische golven na te bootsen in een omgeving die wrijvingsscheuren/contacten bevat. Deze vlakke defecten vertegenwoordigen een soort binnengrenzen waarop de juiste randvoorwaarden moeten worden ingesteld. Afhankelijk van de modelleer hypothesen kunnen scheuroppervlakken als vlak of ruw worden beschouwd. Hier werken we in detail argumenten uit die aantonen dat ruwheid, hoewel het extra complexificatie introduceert, uiteindelijk resulteert in een compactere en elegantere beschrijving in vergelijking met vlakke interfaces. In het bijzonder kan contact van isotrope ruwe oppervlakken effectief worden voorgesteld als contact tussen twee axisymmetrische lichamen. Deze laatste situatie lijkt sterk op de Cattaneo-Mindlin (of Hertz-Mindlin) mechanica waarin twee bollen mechanisch worden onderworpen aan bepaalde normaal- en tangentiële krachten.

Voor het vaststellen van randvoorwaarden bij scheurvlakken is de Cattaneo-Mindlin oplossing onlangs herzien om rekening te houden met niet-sferische (maar asymmetrische contactvormen) en excitatie met niet-constante maar willekeurig in tijd variërende schuine actie. De geformuleerde belasting-verplaatsingsrelatie voor equivalente axisymmetrische lichamen is ook bij benadering geldig voor ruwe oppervlakken en vertegenwoordigt de gezochte randvoorwaarde.

Een andere component van het numerieke akoestische model dat we hier presenteren is een standaard eindige-elementenbeschrijving voor elastische golven in vaste materialen (vaste-mechanica-eenheid in commerciële FEM-pakketten). Er zijn technische inspanningen geleverd om een door de gebruiker gedefinieerd contactmodel als randvoorwaarde te integreren in de vaste-stof-mechanica module. Hierdoor is een compleet model verkregen dat golfgeïnduceerde contactwrijvingsinteracties omvat die beschreven zijn vanuit de eerste principes van contactmechanica.

Een essentiële vooruitgang in vergelijking met eerdere werken is de toepassing van het uitgewerkte model op een geval dat overeenkomt met een bekende techniek vanuit niet-lineair akoestisch niet-destructief onderzoek. De gekozen techniek is gebaseerd op excitatie van een proefstuk met een harmonische golf die, na voltooiing van een transiënt regime, resulteert in een zuiver harmonische respons als het proefstuk intact is, terwijl de respons van een beschadigd proefstuk een inharmoniciteit vertoont. De gegenereerde harmonieken vormen hun eigen stationaire golfpatroon dat een uitgesproken maximum kan hebben rond het defect. In de praktijk worden oppervlaktesignaalmetingen gedaan met behulp van laservibrometrie; onze modellering is daarom een poging om het NDT-experiment met laservibrometrie na te bootsen in geometrisch vereenvoudigde omstandigheden, maar volledig volgens hetzelfde concept.

De vereenvoudigde geometrie is gekozen om de computationele complexiteit te verminderen. De belangrijkste aanname is een 2D-geometrie die meteen een kwantitatieve vergelijking met het experiment onmogelijk maakt. Andere vereenvoudigingen worden hieronder in meer detail besproken. We houden de algemene methodologie echter dicht bij de experimentele principes en genereren een groot aantal synthetische niet-lineaire beelden van een geïsoleerde scheur, ingebed in een fragment van een massieve plaat. We analyseren in detail de invloed van geometrische en fysische parameters van het systeem in het geval van excitaties met één of twee frequenties. Afhankelijk van deze parameters kan het resultaat van de beeldvormingsprocedure variëren van volledig succes (de positie en omvang van de scheur wordt duidelijk geïdentificeerd) tot totale mislukking (er is geen scheur zichtbaar in een beeld dat bestaat uit een opeenvolging van maxima op verkeerde posities). Successen en mislukkingen zijn het gevolg van een complex patroon van de niet-lineaire stationaire golven die worden uitgezonden door de scheur.

Tot slot richten we ons op een concreet voorbeeld dat dicht bij de echte experimentele omstandigheden ligt wat betreft de geometrie van het monster en de geselecteerde randvoorwaarden. Er wordt een eerste kwalitatieve vergelijking tussen theorie en experiment gepresenteerd.

In het algemeen kunnen de resultaten van dit proefschrift interessant zijn voor onderzoekers die betrokken zijn bij niet-lineaire akoestisch gebaseerde niet-destructieve onderzoeksexperimenten en voor hen die zoeken naar toepassingen van moderne semi-analytische contactmodellen gebaseerd op Cattaneo-Mindlin principes.

Content

Introduction and objectives

Context

Only a tiny part of the materials produced, treated or used by mankind are free from any type of damage, defects, or internal structural features. Defects are often categorized into three types: 1D dislocations (e.g. irregularities, impurities, etc.), 2D inner contacts (e.g. cracks, delaminations, etc.) and 3D defects (e.g. pores, voids, etc.). All these defects particularly influence mechanical and physical properties of a material. However, inner contacts impact materials performance in the most crucial way. The reason lies in the inherent instability of the process of cracking, which can be illustrated using the following considerations. Suppose that an elastic continuum contains a circular crack of zero thickness, and that a uniform tensile stress σ is applied to each face of the crack. Then the critical stress σ_0 at which the crack starts growing equals

$$\sigma_0 = \sqrt{\frac{\pi E \Omega}{2R\left(1-\nu^2\right)}},$$

[Sne-51] where Ω [J/m^2] is the surface energy (i.e. the energy needed to form a unit area of free surface), and E and ν are respectively Young's modulus and Poisson's ratio of the material. The instability effect is explained by the inverse proportionality to the crack radius R. Indeed, if the applied stress reaches σ_0, the crack radius increases, and the new critical stress becomes even less than the applied one, so that the cracking process continues until the whole sample fails. For this reason, it is extremely important to develop realistic models that allow the mechanical behavior of solids with inner contacts to be accurately described.

The presence of internal contacts in a material is the reason for contact acoustic nonlinearity that appears at both normal and tangential (relative to the crack faces) loading of the crack. During normal straining the elastic reaction of an open and closed crack is different. The tangential loading engenders friction and associated hysteretic effects. In addition, friction described via the Coulomb friction law **[Des-15]** couples normal and tangential behavior. A successful theory for contact acoustic nonlinearity should appropriately deal with those issues.

Theoretical and numerical modeling approaches for elasticity in materials with inner contacts address at least two situations: distributed damage or localized damage. In the former case, the solid contains a large number of cracks whose exact positions are not known and not important. Typical examples of this case are geomaterials or construction materials consisting of consolidated grains with imperfect bounds between them, or fatigued metals. In this case,

contact nonlinearity shows up as nonlinear or, frequently, hysteretic stress-strain relationships that results from a cumulative influence of the crack ensemble or crack network. Materials belonging to the second case contain only a few cracks whose positions are important. Since the inner contacts represent unique or rare "events" in the material, a statistical analysis is not suitable in this situation. The response strongly depends on the geometry and locations of the cracks so that numerical models of finite element type (or similar based on a detailed meshing of the sample) are most appropriate. An inner contact constitutes an additional boundary at which proper boundary conditions should be defined. In the theoretical part of this thesis, issues related to a friction-induced load-displacement relationship at crack faces are considered in detail.

A standard Finite Element Method (FEM) description together with the user-defined boundary conditions at inner contacts provides a complete model for elastic wave propagation in a material with frictional defects. In general, the use of such a model is beneficial from several points. First of all, modeling grants full digital transparency and an access to all calculated wave field characteristics, which is not the case in real experiments, when only restrained amount of data is available. A much more promising advance could be related to the use of the validated model not for imitating real experiments, but for improving their precision. Indeed, model crack parameters can be varied around their experimentally established values to quantitatively match the experimental response. Then it could be expected that the fitted crack parameters are closer to reality than just visualization data.

In any case, the known link between the reason of nonlinearity (damage) and its measurable manifestations can greatly reduce the uncertainty in data interpretation. In practice, researchers tend to report “cleaner” images with no parasite peaks or distortions considering then as useless side effects. At the same time, if those imperfections are of physical nature and are reproducible both in modeling and experiments, they can become a valuable source of information. A successfully validated model can help deal with such issues on the regular basis.

The above arguments are valid only in the case where the model is proven by experiments. The validation problem is extremely complex since in reality there exist a multitude of factors, such as crack shape or inner roughness features, possible prestress, etc, which are hard to take into account. In the present study we make a first step towards this objective.

In general, it can be stated that the context of this study is related to frictional contact mechanics, numerical acoustics, and nonlinear nondestructive testing by ultrasound.

Objectives

Summarizing these desired requirements we formulate the following objectives of the present study:

Theoretical: elaborate a numerical model or, eventually, numerical tool for modeling wave propagation in materials containing defects

- taking into account real complex geometries of samples
- based on physically plausible contact models including roughness and friction

Experimental: use an existing nonlinear acoustical NDT technique (laser vibrometry)

- for generating nonlinear images of delamination in a composite plate
- to assess damage geometries that can and cannot be seen via the chosen experimental technique

Numerical:

- perform a series of simulations for sample geometries gradually changing from idealized to more and more realistic
- establish qualitative theory and experiment agreement
- identify essential features in the simulated data that can improve the detection of defects

Practical:

- contribute to the creation of computer-assisted nonlinear NDT having an imaging potential stronger than pure experimental methods

Dissertation structure

The thesis contains four Chapters. In Chapter I, we briefly describe existing nonlinear acoustic imaging methods and select one of them especially suitable for comparison with modeling. It is concluded that a method based on formation of nonlinear stationary[1] waves does not require fine focusing of acoustic energy and therefore an attempt to imitate it numerically is associated with coarser meshing and lower computational expenses. In a similar way, we review and classify known modeling approaches to wave propagation in

[1] Here stationary wave is a propagative wave with amplitude independent of time. It can exist in a sample with low reflective boundaries, in contrast to domains with usual boundary conditions of the first, second or third kind, in which standing waves are formed. For the details see Chapter III.

materials with frictional cracks and demonstrate that quite a general physics-based method is necessary that would describe crack-wave interaction for a variety of geometries.

In Chapter II, we utilize the previously developed MMD-FEM code from the IEMN (France) and the Wave Propagation Research Group (KU Leuven, Belgium) to simulate acoustic waves in materials with frictional contacts. We formulate the Method of Memory Diagrams (MMD) that originates from Cattaneo-Mindlin mechanics and provides a boundary condition linking contact loads and displacements at inner interfaces (cracks). It is essential that cracks are considered to have deformable micro-geometry (roughness) instead of having smooth surfaces. This feature results in a purely local description for the boundary condition at a single point without a necessity to satisfy additional conditions in a neighborhood, as it occurs with more traditional account for friction. We also show how to incorporate the MMD into a standard software package (COMSOL) based on the Finite Element Method (FEM).

In Chapter III we apply the elaborated MMD-FEM code for description of wave propagation in idealized cases requiring relatively low computational effort. A fragment of a plate with low reflective boundary conditions at the left and right edges is considered in which a relatively large crack (or parallel to surface delamination) is positioned close to the surface, whereas the sample is excited by a transducer located not far from the crack. The plate fragment has comparable vertical and horizontal dimensions. We generate a large number of synthetic nonlinear images based on generated higher harmonics and on frequency mixing.

Finally, in Chapter IV we attempt to compare modeling and experiments in a qualitative manner. Firstly, we briefly describe an existing nonlinear acoustic experiment with the use of laser vibrometry for measuring surface wave displacements (particle velocities). Then, in a subsequent series of numerical simulations, we gradually change the modeling geometry trying to better imitate the real one. In more realistic cases, the plate is thinner, the distance between the crack and the transducer is higher, etc. Finally, we perform modeling with geometric parameters indeed close to the experiment, but in a two-dimensional case instead of 3D, and demonstrate that synthetic nonlinear images are qualitatively similar to real ones.

Frequently used abbreviations, and variables

Abbreviations

NDT	nondestructive testing
MMD	method of memory diagrams
FEM	finite element method

MMD-FEM	method of memory diagrams integrated into a finite element environment
LDR	local defect resonance
CFRP	carbon fiber reinforced polymer
SLDV	scanning laser Doppler vibrometer or vibrometry
1D, 2D, 3D	one, two, and three dimensions or dimensional
rms	root mean square

Variables

Here we include only variables that are involved in the original derivations. There are also some single formulas in the manuscript cited once and not related to the original model directly. All original notations are unique, whereas in single formulas used once the same notation can have a different meaning. For instance, in the original model, there is a unique parameter C that determines stiffness of the normal load-displacement curve for a crack and depends on composite roughness of crack faces. The same notation C independently appears in Eqs. 6 and 8 of Chapter I where it has two different meanings. These notations hold only locally. The list of unique notations valid for the entire manuscript is given below together with units of measurements.

ρ	density of sample's material, [kg/m^3]
E	Young's modulus of sample's material, [Pa]
ν	Poisson's ratio of sample's material, dimensionless
f	excitation frequency, [Hz]
A	excitation amplitude, [m]
T_{exc}	excitation duration, [s]
a	normal contact displacement, [m]
b	tangential contact displacement, [m]
μ	coefficient of friction of sample's material, dimensionless
u_x	wave x-displacement, [m]
u_y	wave y-displacement, [m]
N_t	number of time discretization points, dimensionless
N_x	number of mesh elements per smallest structure size, dimensionless
σ_{xx}	xx stress component in the convergence test, [Pa]
σ_{xy}	xy stress component in the convergence test, [Pa]

N	normal load, [N] for axisymmetric bodies and [Pa] for rough surface fragments
T	tangential load, [N] for axisymmetric bodies and [Pa] for rough surface fragments
C	stiffness of the normal load-displacement curve depending on inner roughness, [$Pa^{1/2}$ m^{-1}]
$2w$	excitation zone (transducer) length, [m]
x_0	excitation zone center x-coordinate, [m]
η_b	bulk viscosity of sample's material
η_v	shear viscosity of sample's material
K	bulk modulus of sample's material, [Pa]
G	shear modulus of sample's material, [Pa]
ε_{cra}	mean first strain invariant near crack, dimensionless
ε_{exi}	mean first strain invariant near transducer, dimensionless
D_x	deviation of first and last fragment of the stationary tail of u_x time records
D_y	deviation of first and last fragment of the stationary tail of u_y time records
$u_{x,y}^{first}$	u_x and u_y wave displacements for the first fragment of the stationary tail, [m]
$u_{x,y}^{last}$	u_x and u_y wave displacements for the last fragment of the stationary tail, [m]
$A_{x,y}^{n}$	n-th harmonic amplitude of u_x and u_y of the measured signal, [m]
$I_{x,y}$	nonlinear criterion (x and y-direction), dimensionless
$I_{x,y}^{NL}$	nonlinear criterion based on nonlinear frequency mixing (x and y-direction), dimensionless
$I_{x,y}^{LDR}$	nonlinear criterion based on nonlinear resonance (x and y-direction), dimensionless
$C_{x,y}$	contrast (x and y-direction), dimensionless
C_{cr}	crack center x-coordinate, [m]
L_{cr}	crack length, [m]
f_I	first frequency for the case of frequency mixing, [Hz]
f_{II}	second frequency for the case of frequency mixing, [Hz]

A_I first excitation amplitude for the case of frequency mixing, [m]

A_{II} second excitation amplitude for the case of frequency mixing, [m]

f_B base frequency for the case of frequency mixing, [Hz]

$A^I_{x,y}$ x and y amplitudes of the measured signal harmonics at first frequency f_I, [m]

$A^{II}_{x,y}$ x and y amplitudes of the measured signal harmonics at second frequency f_{II}, [m]

N_p number of quasi-periods considered in the stationary tail of signal, dimensionless

f_m frequency number m in Fourier spectrum, [Hz]

τ shear stress, [Pa]

σ normal stress, [Pa]

R radius of spheres in the Cattaneo-Mindlin problem, [m]

$$E^* = \frac{E}{2\left(1-\nu^2\right)}$$

$$\theta = \frac{2-\nu}{2\left(1-\nu\right)}$$

c contact zone radius, [m]

s stick zone radius, [m]

$w(\rho)$ tangential displacement field, [m]

$\tau(\rho)$ shear stress field, [Pa]

$u(c,\rho)$ normal displacement field, [m]

$\sigma(c,\rho)$ normal stress field, [Pa]

$D(\rho)$ memory function, dimensionless

Q reduced normal force, [N] for axisymmetric bodies and [Pa] for rough surface fragments

q reduced normal displacement, [m]

b_0 tangential displacement due total sliding, [m]

$\tilde{b}$ tangential displacement due to bodies' shearing, [m]

$\vec{l}$ unit vector in the direction of slip

$z(\rho)$	gap distribution characterizing axisymmetric contact shapes, [m]
A_n	nominal contact area, [m^2]
A_g	geometric contact area, [m^2]
h'	rms of the random surface slope, dimensionless
k	tangent to the random gap distribution $\varphi(z)$, [m^{-2}]

Chapter I. Contact acoustic nonlinearity and nondestructive testing

This Chapter briefly summarizes the available literature on contact acoustic nonlinearity in the context of nondestructive testing. The presented review supports the idea that despite of existence of a number of particular models (frequently phenomenological or simplified e.g. 1D), an adequate model usable for the NDT purposes should account for a realistic contact with friction mechanically activated with an oblique action variable in time, in a way similar to the effect of an acoustic wave.

1. Geometric, material and contact nonlinearities

Section 1 offers a succinct analysis of mechanical nonlinearity, encompassing geometric, material, and contact aspects. Geometric nonlinearity pertains to changes in the distance between two points under external loads. Material nonlinearity arises from discord in interatomic potentials, while contact nonlinearity manifests in materials with internal contacts, like cracks, delaminations, and imperfect intergranular boundaries.

1.1. Geometric nonlinearity

Geometric nonlinearity occurs when trying to connect changes in distance between two points in a strained material with the displacement vector **[Lan-93]**. This connection is expressed by Eq. (1):

$$dl'^2 = dl^2 + 2\varepsilon_{ik} dx_i dx_k \,, \tag{1}$$

where dl and dl' are distances between close points in unstrained and strained bodies, respectively, $x_i\,(i=1,2,3)$ are Cartesian coordinates, and ε_{ik} is the strain tensor calculated as

$$\varepsilon_{ik} = \frac{1}{2}\left(\frac{\partial u_i}{\partial x_k} + \frac{\partial u_k}{\partial x_i} + \frac{\partial u_j}{\partial x_i}\frac{\partial u_j}{\partial x_k} \right), \tag{2}$$

through the displacement vector u_i. In the above formulas, the implicit summation is used.

In mechanics and acoustics, strains are typically small, meaning that alterations in the sample size are much less significant than the size itself. This means that all derivatives of the kind $\partial u_i / \partial x_k$ are much smaller than 1. Hence, the product of the derivatives in Eq. (2) can be neglected and

$$\varepsilon_{ik} = \frac{1}{2}\left(\frac{\partial u_i}{\partial x_k} + \frac{\partial u_k}{\partial x_i} \right). \tag{3}$$

The term we're ignoring deals with geometric nonlinearity. Considering it leads to more complex equations in solid mechanics, as explained by **[Gad-84]**. However, accounting for geometric nonlinearity is only necessary for certain systems, like bending thin bars or plates and cable-stayed structures, which we won't be covering in this thesis.

1.2. Material nonlinearity

The source of material nonlinearity is linked to the inherent unharmonicity in the potential energy of interactions among atoms comprising the lattice. In an ideally linear material, the interatomic potential would exhibit a parabolic (harmonic) profile based on the distance between the atoms. A more practical representation is the Lennard-Jones potential **[Len-24]**, which characterizes the interaction between a pair of neutral atoms or molecules:

$$U_{LJ}(r) = U_0 \left[\left(\frac{r_m}{r} \right)^{12} - 2\left(\frac{r_m}{r} \right)^{6} \right], \tag{4}$$

depicted in Fig. 1. Here, U_0 represents the depth of the potential well, and r_m is the distance at which the potential reaches its minimum. It is straightforward to demonstrate, via Taylor expansion of $U_{LJ}(r)$ around r_m that this potential exhibits a weak inharnonicity, becoming more significant as r deviates considerably from the rest radius r_m:

$$U_{LJ}\left(r\right) \approx U_0 \left[-1 + 36\left(\frac{r - r_m}{r} \right)^2 - 252\left(\frac{r - r_m}{r} \right)^3 + 1113\left(\frac{r - r_m}{r} \right)^4 \right]. \tag{5}$$

Here the value $((r - r_m)/r)^2$ is related to strain ε in the simple 1D case, while the potential $U_{LJ}(r)$ contributes directly to the strain energy U of a unit volume:

$$U\left(\varepsilon\right) \sim U_0 \left[-1 + 36\varepsilon^2 - 252\varepsilon^3 + 1113\varepsilon^4 \right]. \tag{6}$$

Now it evident that the stress $\sigma = dU/d\varepsilon$ becomes a nonlinear function of strain ε because of inclusion of the term with powers higher than 2 in Eq. (6).

A more general form of the nonlinear stress-strain relationship corresponding to the material nonlinearity is easy to obtain **[Lan-93]** in the following way. The expression for the elastic energy W should not depend on the choice of the reference frame, therefore it must contain tensor invariants only. Symmetric 2-nd rank tensors have only two quadratic (ε_{ik}^2 and ε_{ll}^2) and

three cubic ($\varepsilon_{ll}^3, \varepsilon_{ll}\varepsilon_{ik}^2, \varepsilon_{ik}\varepsilon_{il}\varepsilon_{kl}$) invariants in which the sum over indexes is meant. Hence in the isotropic case

$$W = G\varepsilon_{ik}^2 + \left(\frac{K}{2} - \frac{G}{3}\right)\varepsilon_{ll}^2 + \frac{A}{3}\varepsilon_{ik}\varepsilon_{il}\varepsilon_{kl} + B\varepsilon_{ll}\varepsilon_{ik}^2 + \frac{C}{3}\varepsilon_{ll}^3, \tag{7}$$

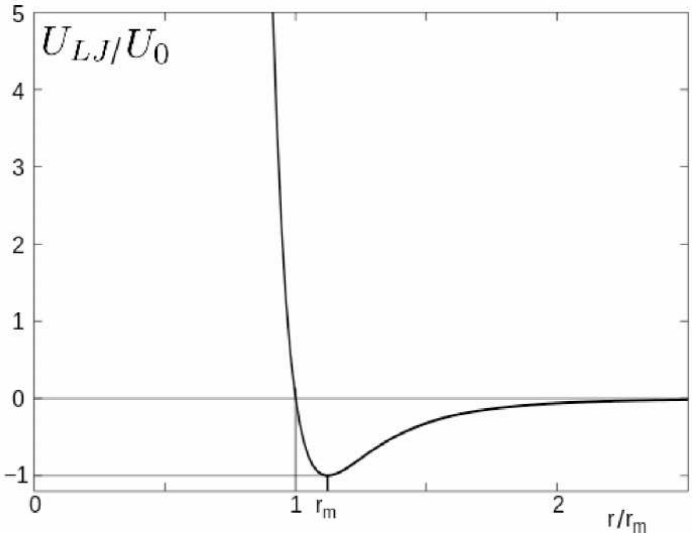

Fig. 1. The Lennard-Jones 6-12 potential approximates the intermolecular interactions of two atoms. Figure referred to **[Tri-17]**.

where *K* and *G* are the bulk and shear moduli, respectively. This fact can be confirmed by differentiation of the first two components of *W* over its arguments ε_{ik}, which produces Hooke's law for isotropic materials **[Lan-93]**:

$$\sigma_{ik} = K\varepsilon_{ll}\delta_{ik} + 2G\left(\varepsilon_{ik} - \frac{1}{3}\delta_{ik}\varepsilon_{ll}\right), \tag{8}$$

where σ_{ik} is the stress tensor and δ_{ik} is the Kronecker delta.

In Equation (7), three nonlinear constants, namely A, B, and C, have been introduced. Therefore, the complete constitutive model for material nonlinearity is constructed using only five constants, defining the stress-strain relationship. While the depiction of anisotropic materials demands additional material constants, the stress-strain relation can still be expressed as a closed-form expression. As the subsequent section will demonstrate, the case of contact nonlinearity is generally more intricate.

1.3. Contact nonlinearity

Contact nonlinearity constitutes the third category of mechanical nonlinearities examined in this context. Inner contacts within materials and structures can represent defects, such as cracks or delaminations, or other defect-like features like loose joints. Their impact on the

response to acoustic excitation is two-fold. Firstly, their response to normal loading exhibits bimodality, indicating significantly different stiffness in open (lost contact) and closed (contact occurs) states. Additionally, apart from the nonlinearity associated with bimodality, the normal load-displacement curve in the closed state is inherently nonlinear. This behavior arises because contact surfaces possess some relief, and with increasing compression, deeper material layers undergo strain. In fact, only two half-spaces filled with linear elastic continua, without edge effects, exhibit a purely linear loading curve.

Another aspect of contact interaction is friction. Friction introduces a multifaceted tangential response, characterized not only by nonlinearity but also by hysteresis. This means that the response is not determined instantaneously by the excitation but depends on the excitation history. Essentially, friction leads to both sticking and sliding in different contact zones. In the stick state, the system "memorizes" a local tangential displacement (which remains unchanged as per the definition of stickiness). The presence of memory in a system contributes to its hysteric behavior.

In the next sections we consider existing models for contact nonlinearity in more detail.

2. Existing models for contact nonlinearity

There are several models exist to describe the nonlinear elastic behavior of materials, with a specific focus on theories that generate nonlinear stress-strain relationships-critical for constructing numerical models simulating nonlinear wave propagation. The objective is to develop a numerical tool for nonlinear non-destructive testing (NDT). Notably, these models also predict characteristics such as wave dispersion, attenuation, parameter variations over time, and changes in linear elastic properties with damage. Beyond the conventional Landau theory **[Lan-93]**, "nonclassical" models fall into two categories: phenomenological, postulating desired behavior in stress-strain relations, and physical, considering the actual internal contacts' physical behavior. Most of these models cater to one-dimensional (1D) scenarios, particularly in highly idealized wave propagation geometries.

2.1. Phenomenological stress-strain models

The models examined in the following sections have primarily been introduced by acousticians dealing with materials containing numerous internal contacts. This leads to a stress-strain relationship characterized by hysteresis, rather than a straightforward connection between load and displacement established at a single interface. These models are predominantly phenomenological, often simplistic, as they tend to assume the stress-strain behavior with *ad hoc* nonlinear properties rather than offering a physical explanation.

2.1.1. Clapping or bimodal model

The basic phenomenological model focuses on a single contact, like a crack, perpendicular to the longitudinal wave direction. When the incident wave's stress exceeds the initial interface static stress, the crack opens, altering the material's overall stiffness. A simple method to model this involves assigning different stiffness values for positive and negative strains:

$$\sigma = C\left(1 - H(\varepsilon)\frac{\Delta C}{C}\right)\varepsilon, \tag{9}$$

where $H(\varepsilon)$ denotes the Heaviside step function (refer to **[Sol-02]**, for the clapping or bimodal model, or similar relationships by **[Naz-89]**, and **[Ost-91]**).

2.1.2. Sliding friction model

Although the earlier model focuses on normal wave incidence, the sliding friction model pertains to the interaction between tangential wave and interface. Consider an unbounded interface between two friction-coupled surfaces, experiences an oscillating tangential traction (shear wave scattering) of sufficient strength to induce sliding. Assume that gross sliding of the interfaces occurs when the shear wave stress ε surpasses a specific value ε_1. Subsequently, the tangential stiffness, which has a value of C in the stick phase, reduces to zero in the sliding phase, so that

$$\frac{d\sigma}{d\varepsilon} = \frac{C}{2}\left(1 - \operatorname{sgn}(\dot{\varepsilon})\operatorname{sgn}\left[\varepsilon + \operatorname{sgn}(\dot{\varepsilon})\varepsilon_1\right]\right) \tag{10}$$

(see **[Bal-02]**). It's crucial to emphasize that, in contrast to the clapping model where both odd and even harmonics are produced, the sliding friction model exhibits symmetry concerning positive and negative ε, resulting in the generation of only odd harmonics.

These fundamental mechanisms of contact nonlinearity are frequently found in a combined or mixed form. At a basic level, they provide a reasonable explanation for observed effects. Furthermore, if the sample's geometry favors one of these modes, it can be discerned through the presence or absence of even harmonics.

2.1.3. Preisach model

The Preisach model is a mathematical formalism suitable for the description of a wide class of hysteretic dependencies in 1D (see **[Pre-35]**, **[Kra-89]**). Suppose we have a collection of bistable elements such that each of them can be open (contribution 1) or closed (contribution 0). For each of them, there are two critical values of the argument x: x_o and x_c ($x_o > x_c$). By definition, the element (x_o, x_c) is open if $x > x_o$ and closed if $x < x_c$. (see Fig. 2). A hysteretic function y is obtained then as a sum of all contributions of all elements (i.e. contributions of

the open elements since the closed ones do not contribute) weighted by a 2D weighting function $\rho(x_o,x_c)$ called the Preisach density.

In this formalism, the Preisach density represents the portrait of the system. By varying the density, the responses of a wide range of hysteretic systems can be imitated. The method allows one to obtain the response $y(t)$ of a hysteretic system for any signal $x(t)$ that makes it particularly suitable for complex acoustical excitations.

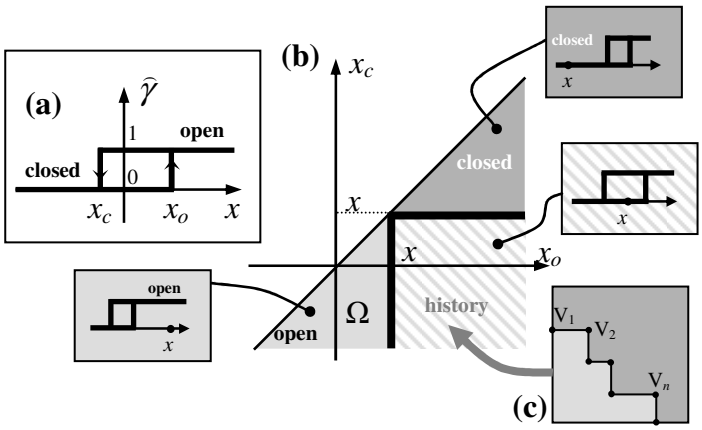

Fig. 2. **(a)** *Hysteretic element characterized by critical values x_c and x_o.* **(b)** *The Preisach space (x_o,x_c) containing three areas: triangles with open and with closed elements, and rectangle where the state of elements is determined by the history of the system.* **(c)** *Typical configuration of the history-dependent part of the Preisach space (refer to* **[Ale-04]***).*

There are two identifying criterions for the Preisach system (see **[May-85]**); using these criterions it is possible to check if a particular hysteretic model represents the Preisach system or not.

In addition, there exist procedures (see **[Guy-97]**, **[Ale-08]**) for reconstructing the Preisach density from a sole particular hysteretic curve. The methods work well for high quasi-static loads where up-going and down-going branches of a hysteresis loop are clearly distinguished. However, many researchers used the Preisach formalism for acoustical simulations as well assuming a constant density or accepting some model density forms. The advantage of the approach is in its flexibility and possibility to imitate a wide class of hysteretic dependencies. The disadvantage is related to its phenomenological character; the theory becomes physical only when the Preisach density and other model characteristics are linked to physical and geometrical parameters of the material and damage. Assuming various forms for the Preisach density, it is possible to deduce (see **[Van-12]**) from the Preisach formalism a number of particular hysteretic models, such as the hysteretic quadratic nonlinearity, Nazarov, Davidenkov, and Granato-Lücke models (see below).

2.1.4. Hysteretic quadratic nonlinearity

Derived from the Preisach formalism, this model is formulated by considering a harmonic excitation with the amplitude $\Delta\varepsilon$, leading to the resultant expression for stiffness:

$$\frac{d\sigma}{d\varepsilon} = C\left(1 + 2\beta\varepsilon - \alpha\left[\Delta\varepsilon + \operatorname{sgn}\left(\dot{\varepsilon}\right)\varepsilon\right]\right) \tag{11}$$

where α and β are material constants. Due to its simplicity, several researchers have employed this model to examine the influence of hysteresis on wave shapes (see **[Ale-04]**), simulate resonance experiments, and explore theoretical amplitude dependencies for nonlinear resonant frequency shifts and higher harmonics in resonance (see **[Van-00]**), among other applications.

2.1.5. Nazarov model

The model, as outlined in **[Naz-03]**, is designed for harmonic excitation with an amplitude $\Delta\varepsilon$. It involves three parameters and provides separate descriptions for the up-going and down-going branches:

$$\begin{cases} \sigma^{+}\left(\varepsilon\right) = C\left(\varepsilon - \alpha\left(\Delta\varepsilon\right)\varepsilon + \left(\dfrac{\beta_1 + \beta_2}{4}\right)\left(\Delta\varepsilon\right)^2 - \dfrac{\beta_1}{2}\varepsilon^2\right) \\ \sigma^{-}\left(\varepsilon\right) = C\left(\varepsilon - \alpha\left(\Delta\varepsilon\right)\varepsilon - \left(\dfrac{\beta_1 + \beta_2}{4}\right)\left(\Delta\varepsilon\right)^2 - \dfrac{\beta_2}{2}\varepsilon^2\right) \end{cases} \tag{12}$$

This model represents a variation of the method employing hysteretic quadratic nonlinearity. It can be derived from the Preisach formalism by setting:

$$\rho\left(\varepsilon_{o,}\varepsilon_c\right) = C\frac{\beta_1 + \beta_2}{2} \tag{13}$$

where ε_o and ε_c are strain-related arguments introduced instead of formal arguments x_o and x_c.

2.1.6. Davidenkov model

The adjusted Davidenkov model, detailed in **[Dav-38]**, postulates the following expressions for the stress-strain curves:

$$\begin{cases} \sigma^{+}\left(\varepsilon\right) = C\left(\varepsilon + \dfrac{\alpha}{m}\left(2^{m-1}\left(\Delta\varepsilon\right)^m - \left(\Delta\varepsilon + \varepsilon\right)^m\right)\right) \\ \sigma^{-}\left(\varepsilon\right) = C\left(\varepsilon - \dfrac{\alpha}{m}\left(2^{m-1}\left(\Delta\varepsilon\right)^m - \left(\Delta\varepsilon - \varepsilon\right)^m\right)\right) \end{cases}. \tag{14}$$

It can be obtained from the Preisach formalism by configuring

$$\rho\left(\varepsilon_o, \varepsilon_c\right) = C\alpha\left(m-1\right)\left(\varepsilon_o - \varepsilon_c\right)^{m-2}. \tag{15}$$

2.1.7. Granato-Lücke model

The Granato-Lücke model, as outlined in **[Gra-56]** and **[Naz-09]**, is rooted in the physics of dislocations, which encompasses hysteretic behavior. The stress-strain curves within the (modified) Granato-Lücke model encompass four branches and can be formulated as follows:

$$\sigma(\varepsilon,\dot{\varepsilon}) = C\begin{cases} (\varepsilon - \frac{\gamma_1}{m}\varepsilon^m) & if \quad \varepsilon \geq 0, \dot{\varepsilon} \geq 0 \\ (\varepsilon + \frac{\gamma_2}{m}\varepsilon^m - \frac{\gamma_1+\gamma_2}{m}(\Delta\varepsilon)^{m-1}\varepsilon) & if \quad \varepsilon \geq 0, \dot{\varepsilon} \leq 0 \\ (\varepsilon + \frac{\gamma_3}{m}\varepsilon^m) & if \quad \varepsilon \leq 0, \dot{\varepsilon} \leq 0 \\ (\varepsilon - \frac{\gamma_4}{m}\varepsilon^m + \frac{\gamma_3+\gamma_4}{m}(-\Delta\varepsilon)^{m-1}\varepsilon) & if \quad \varepsilon \leq 0, \dot{\varepsilon} \geq 0 \end{cases} \tag{16}$$

Here the Preisach space is not constant (quadratic hysteretic, Nazarov) and does not depend only on the perpendicular coordinate $\varepsilon_\perp = (\varepsilon_o - \varepsilon_c)/\sqrt{2}$ (Davidenkov), but equals

$$\rho(\varepsilon_o,\varepsilon_c) = \begin{cases} C\frac{m-1}{m}(\gamma_1+\gamma_2)\varepsilon_o^{m-2} & if \quad \varepsilon_o > \varepsilon_c > 0 \\ C\frac{m-1}{m}(\gamma_3+\gamma_4)|\varepsilon_c|^{m-2} & if \quad \varepsilon_c < \varepsilon_o < 0 \\ 0 \quad otherwise \end{cases} \tag{17}$$

Since the density equals 0 in a whole quadrant $\varepsilon_c<0$, $\varepsilon_o>0$, some internal loops within the large hysteresis loop can be actually non-hysteretic (reversible i.e. no difference between up-going and down-going branches). The original Granato-Lücke model does not have this property since it is not intended for non-harmonic signals at all.

In contrast to the generic Preisach formalism, these models offer the advantage of fewer free parameters. Nevertheless, they remain purely phenomenological with an *ad hoc* character. Comprehensive graphical representations of the hysteretic quadratic, Nazarov, Davidenkov, and Granato-Lücke models are provided in **[Van-12]**.

2.1.8. Vector and tensor Preisach models

In the vector Preisach model, it is suggested (see **[May-88]**) that any direction of the output vector generates its own scalar Preisach space that depends on two switching values (x_o, x_c). The elementary hysteretic units are switched by the projection of the input vector on the direction of the output vector. As such, the Preisach density additionally depends on the polar angle in 2D case, $\rho=\rho(x_o,x_c,\varphi)$, and on the spherical angles, $\rho=\rho(x_o,x_c,\theta,\varphi)$, in the 3D case. This also means that the distribution of open and closed elements can be different for each angle.

The tensorial model (see **[Hel-01]**) uses the Kelvin notations and representation of the stress and strain tensors as 6-component vectors. These vectors are linked with a 6x6 matrix that can be diagonalized thus presenting 6 eigenvectors. It is suggested that these 6 eigenvectors are separately multiplied by the stress vector which results in the appearance of 6 scalar quantities. Then, 6 independent Preisach spaces are introduced with the above 6 scalar inputs; the corresponding outputs are considered as weighting coefficients for the 6 eigenvectors in a linear combination that represents the global output of the model.

The tensor Preisach model actually implied some additional simplifications compared to the vector model. They come from the imposed consideration of 6 eigenvectors in the Kelvin notations that brings into the model only 6 independent Preisach spaces, while in the vector model the number of Preisach spaces is continual. In any case, the number of free parameters is huge which makes the identification problem (retrieving material's parameters from data) hardly solvable.

2.1.9. Preisach-Arrhenius model

This model, detailed in **[Tor-02]** and **[Gus-05]**, represents one of the various potential extensions of the Preisach formalism. It introduces energy barriers separating the open and closed states of the hysteretic elements, proposed to be very weak (comparable to kT). This adjustment leads to several dynamic effects, including dispersion and spontaneous transitions between the two metastable states. It proves useful when a scalar representation of the stress-strain relationship suffices, and accounting for dynamic effects and relaxation becomes essential.

2.1.10. Conclusion

In conclusion it can be noted that the models of the phenomenological class are suitable only for imitating contact nonlinearity (in a precise or qualitative way), but neither for explaining it nor linking it to the materials' parameters. They can be very flexible, but for the price of high number of free parameters and associated difficulties in solving the identification problem. At the same time, the simplified versions can reproduce the nonlinear effects in a qualitative manner only.

2.2. Physical stress-strain models

Physical models adopt an approach that fundamentally diverges from pure phenomenological considerations. In this context, the assumption is made that one or more physical mechanisms are responsible for the observed nonlinear effects. By acknowledging a specific geometry,

even in a highly simplified form, for the defects, an appropriate model is selected for the fundamental physical mechanism (such as friction, adhesion, collective transformations of dislocations, etc.) that hypothetically underlies the nonlinear behavior. Below, we provide examples of several models within this class.

2.2.1. Lawn and Marshall model

In this model (refer to **[Law-98]** for the original version or **[Ale-07a]** for the modified model taking into account additional effects), an elastic continuum contains a large number of diversely oriented plane cracks. For each of them, the Coulomb friction law is postulated that assumes either stick state or total sliding (i.e. with no stick zones) of the crack surfaces. The choice of the state depends on the normal and shear stresses transmitted to the crack faces from distant boundaries of the sample, where external loading conditions are posed. Then, all displacements of the cracks faces (only tangential in the original model **[Law-98]** and both tangential and normal in the modified one **[Ale-07a]**) are summed up with the relevant orientational weighting coefficients to produce the total strain tensor. It is seen that a large number of cracks having the postulated behavior give rise to hysteretic responses of the Preisach type with internal loops for partial loading-unloading-reloading, etc. In other words, the model explains the macroscopic stress-strain hysteresis as a collective movement of individual cracks. Moreover, experimental results for complex quasi-static loading can be fitted by matching a very limited number of model parameters. This makes us believe that the suggested mechanism of internal friction is primarily responsible for the hysteretic constitutive behavior of micro-cracked solids. The model has not been tested for weak acoustical excitation, since at this level it most likely provokes only partial slip in micro-contacts, which is neglected by the adopted friction model. In addition, small characteristic displacements of the cracks' faces can bring into play adhesion effects.

2.2.2. Micro-potential model

The **[Ale-05]** model explores the hysteresis in stress-strain of materials by considering two key factors: adhesion forces requiring a force to separate surfaces in contact and a persistent gap between crack faces even without external strain. Notably excluding friction, this model introduces a double-well potential for internal cracks, existing in either "adhesive" states (faces trapped with a non-zero pull-off force) or "open" states (faces not in contact). Applying the Preisach formalism, each hysteretic element corresponds to a single crack, allowing for variability based on geometric factors. The model predicts theoretical stress-strain

relationships with hysteresis, qualitatively aligning with observed behavior in experiments on micro-cracked solids under mild acoustic excitation.

2.2.3. Adhesion hysteresis model

In this adhesion-based model (see **[Sha-94]**, **[Ale-07b]**), the stress-strain hysteresis is deduced from hysteresis in adhesion. Indeed, introduction of the surface energy and related pull-off force leads to the formation and rupture of adhesive necks connecting two asperities belonging to the opposite crack faces. These necks are formed when two asperities that initially were in contact separate. The presence of a neck means that the asperities interact with some attraction force. When identical asperities, initially distant, are approaching each other, a neck will not form until atomic contact is reached, so that at the same distance between the asperities they do not interact. So the presence of the interaction force depends on the movement direction (approaching or separating) that actually corresponds to hysteresis at the micro-level. Again, it is possible to transfer this model to the Preisach description; a hysteretic element is represented in this case by a pair of contacting asperities. In this model, the decomposition of continuous roughness into a set of individual asperities presents an additional problem.

Again, the model offers the opportunity to qualitatively describe nonlinear acoustic experiments in media with simple geometries.

2.2.4. Soft-ratchet model

The model presented in **[Vak-05]** aims to replicate acoustical experiments on both short and long timescales, specifically addressing the phenomena known as slow dynamics effects as discussed in **[Ost-01]**. The slow dynamics effect encompasses various timescales, characterized by a sudden reduction in elastic moduli following intense straining from a powerful acoustic wave or impact. Subsequently, the modulus experiences a gradual (logarithmic) recovery, approaching but not reaching its original value. In the model, this effect is attributed to the asymmetry in the creation and breaking of adhesive bonds at the micro-level. The assumption is that multiple paths exist for breaking a bond, as an individual atom can belong to different asperities after breaking. However, there is only one way to reunite two initially separated asperities. This implies that the process of breaking the bond is faster than the healing process, leading to a more likely drop in modulus during intense straining.

2.2.5. Pack of Hertz-Mindlin spheres

In the model detailed in **[Nih-00]**, devised for isotropic materials with internal cracks like sandstones, the intricate geometry of the actual material is substituted with a collection of spheres interacting based on the Hertz-Mindlin laws (refer to **[Min-53]**; note that the term "Hertz-Mindlin" is conventional, although, historically, it is more accurate to designate this solution as Cattaneo-Mindlin **[Cat-38]**). Known force displacement relationships for elastic spheres in contact with friction were used for calculating the response of a face-centered cubic sphere pack subjected to uniaxial strain loading ε_{zz}. The spheres were considered as unconsolidated, so that, in order to model a solid material, the pack was confined from the sides, $\varepsilon_{xx}=\varepsilon_{yy}=0$. This greatly simplified system provides a hysteretic stress-strain response σ_{zz} vs ε_{zz}, similar to the experimental hysteretic curves for rocks. The model successfully predicts several experimentally observed phenomena, including the displacement of the first hysteresis loop concerning subsequent loops under periodic excitation and the strain-independent behavior of dynamic moduli. Despite its potential in describing micro-cracked materials, the model encounters challenges when considering the material's consolidation.

2.3. Physical load-displacement models

In the previous section, we have presented a brief review of existing models for a micro-cracked material, whereas in the context of NDT, it is appropriate to discuss available approaches to mechanics of materials with a single crack or a number of cracks. As it was mentioned, for individual cracks boundary conditions related to contact loads and displacements should be set.

2.3.1. Models for normal contact interaction of rough surfaces

Contact mechanics started with the problem of normal contact of two elastic spheres solved by H. Hertz in 1882. Much later, in 1960s, this solution was applied to contact of rough surfaces. The idea is based on the assumption that a continuously rough surface can be represented as a collection of individual asperities whose summits are approximately spherical. In the simplest case considered by Greenwood and Williamson in 1966 **[Gre-66]**, the spheres are identical but their heights are different and present a statistical ensemble. Analytical results were obtained for exponential and for Gaussian distributions of asperities' heights that close resemble measurement data. Moreover, it was shown that the real contact area representing only a tiny part of the nominal one is exactly or approximately proportional to the contact load. This fact, established in 1930s (see **[Bow-39]** and references in **[Gre-66]**), can be used as a test for any contact model for rough surfaces.

As an improvement, Whitehouse and Archard **[Whi-70]** showed that a better approximation for the real surface roughness can be obtained by considering a collection of different spheres. The two key points in the Whitehouse and Archard contact mechanics model consist in (i) the introduction of a set of points spaced by a sampling interval comparable to the correlation radius of the random function representing roughness, and (ii) the treatment of a mutual distribution of heights at neighboring points. As such, the value of this model is that the procedure of roughness decomposition into a set of spherical asperities uses original statistics of the continuous roughness and its correlation properties. However, in this model, the continuity of the real rough surfaces is still not fully represented.

Recently, other interesting approaches in contact mechanics have been developed, such as the introduction of fractality in the consideration of surface roughness (**[Maj-91]**, **[Yan-98]**). Nonetheless, the problem of an adequate description of two rough surfaces in contact remains. Moreover, the substitution of a real fractal surface by a mathematical representation with certain postulated properties and similar behavior has led to discrepancies with experimental data. A fundamental approach in this field **[Per-02]**, not using Hertz contact at all, targets the relationship between force and contact area. Unfortunately, this particular knowledge is insufficient for us, since our study compels to start from the force versus displacement relationship.

2.3.2. Plane cracks governed by the Coulomb friction law

The Amontons-Coulomb friction law (see **[Zhu-40]** and, for the historical review, **[Des-15]**) is a common approximation for frictional contact interaction originating from inelastic deformations of asperities in contact. It states that a material point posed on a substrate and experiencing a tangential loading can stick to the substrate or slip on it. In the former case, no relative movement occurs, and the tangential displacement that could appear during previous evolution, remains fixed. The friction force T equilibrates the external loading not exceeding a threshold value μN, with N, the normal reaction force, and μ, the coefficient of friction. When the external tangential load reaches the threshold μN, the friction force freezes at that level, and the material point starts sliding. The tangential displacement is unlocked and becomes *a priori* unknown, or, better to say, it is determined not by the contact system, but by external conditions.

The same considerations hold for contact of two surfaces, except that forces and displacements become local stresses and local displacement fields, respectively.

It can be immediately concluded that the Coulomb friction law does not provide the sought-for boundary conditions in a unique way. More precisely, it produces the Dirichlet boundary

condition (for displacements i.e. of the first type) in the situation of stick, while in the slip case we have the Neumann boundary condition (for stresses i.e. of the second type). This means that, in a numerical implementation, it is necessary to check if the Coulomb threshold is achieved at every discretization point/element in the crack interface. In practice, at a certain moment, a condition $|T| > \mu N$ can re reached in some discretization element which is prohibited by the Coulomb friction law. In this case, the condition $|T| = \mu N$ should be enforced by redistributing all stresses and displacements in a neighboring area. This is doable **[Bla-14]**; however, the corresponding computational expenses can be quite high. In any case, the computational effort for a cracked sample is dramatically higher in comparison to an intact one. The obvious reason for that is in the implicit character of computations.

2.3.3. Example of a purely numerical contact description: Kalker software

In the previous section, principles of contact modeling with friction were sketched. In fact, nowadays, numerical contact mechanics is a vast discipline comprising a large number of methods **[Yas-13]**. The contact area itself as well as areas of stick and slip are *a priori* unknown and are calculated in the solution process.

One of the oldest examples is presented by so-called Kalker software based on solutions found in 1980s **[Kal-88]**, **[Vol-23]**. The software package contains two modules targeting as wheel-rail contact and systems of Hertzian type called basic contact by the authors. The latter is illustrated in Fig. 3 below. The numerical solver calculates stress and displacement fields at contact interfaces also providing the access to elastic field in the interiors of the bodies.

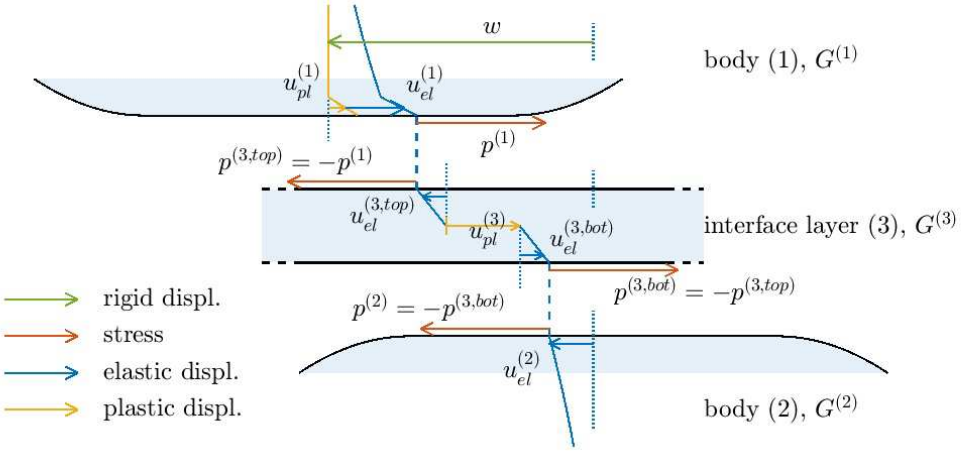

Fig. 3. Contact geometry including a third body. Notations illustrate the degree of detail taken into account by Kalker software.

It is important to note that the friction coefficient in detailed numerical models can depend on slip velocity as well as on temperature. Moreover, complex phenomena such as friction coefficient memory and relaxation are taken into account.

Full detailed numerical solutions can be used for describing the behavior of a system excited acoustically, as a particular case, but are clearly not intended for that. The associated computational expenses are extremely high.

2.4. Conclusion

The above review demonstrates the necessity of an efficient contact model, providing boundary conditions corresponding to an inner frictional contact (crack) in a solid material. The existing approaches are either not applicable for that purpose, either require significant computation effort. In Chapter II, we expect that the Method of Memory Diagrams (MMD) **[Ale-15]**, formulated by the accomplished author, provides a well-balanced approach that combines essential physical principles with computational efficiency.

3. Recently developed nonlinear acoustic imaging methods

Since 1990s-2000s, there exist a growing interest to nonlinear acoustic methods for detecting the presence of damage in materials and structures. One of them (see more complete review **[Ost-01]**) uses the fact that frequency of an acoustic resonance becomes amplitude-dependent in nonlinear materials. Since contact nonlinearity, if existing is typically dominant over other nonlinearity types, amplitude-dependent resonances are good indicators of damage.

The practical use of NDT requires, however, not only to detect the presence of damage but also to determine a damage location. Ideally, a robust image of damage should be obtained. In fact, the nonlinear imaging methods can be roughly categorized into two groups.

The first group comprises techniques that use a continuous wave excitation with a characteristic wavelength comparable to the defect size. After the transient regime decay, a wave pattern is formed with stationary (i.e. independent of time) amplitude. The time dependence of the wave field contains a nonlinear component that can be used for calculating of a nonlinear criterion or image that is supposed to be concentrated in space near the defect. In that regard, the nonlinear wave pattern itself can indicate the position and extent of the defect.

Methods belonging to the second group require sharp focusing and the wavelength considerably smaller than the defect, since it is the wavelength that determines the imaging resolution in this case. Formation of stationary waves is not required.

Computational expenses essentially depend on the mesh size which, in turn, is determined by the smallest element of geometry. From that point, it is preferable to numerically implement a method of the first group to keep the computational effort at a reasonable level. Indeed, sharp focusing would require having the mesh size smaller than the wavelength λ , the smallest spatial scale in that case. Therefore, the total number of mesh elements is proportional to $1/\lambda^2$ in 2D. Since time stepping is linked to the mesh element size (see Section 2.2 of Chapter II for details), the total computational effort becomes proportional to $1/\lambda^3$ and is very high. This is the reason to prefer an experimental method from the first class, which are less demanding in terms of smallness of λ, even if they require a longer total calculation time necessary for adequate representing the stationary waves formation process.

In this section we present several examples of methods belonging to both classes to justify our choice of the damage imaging localization technique most suitable for our first attempt to imitate a real imaging experiment starting from physical principles.

3.1. Nonlinear imaging methods based of stationary wave formation

3.1.1. Nonlinear resonant scanning laser vibrometry

The method uses a continuous vibrational/wave excitation of a structure that activates hidden damage and produces higher harmonics. The sample's surface is scanned with a laser beam for simultaneous measurements of surface displacements/velocities via a precise interferometric technique (Fig. 4). These fields contain higher harmonics that reach maximum amplitude in the vicinity of damage **[Pfl-04]**. It is also possible to use very high harmonics (up to 20^{th}, **[Bal-02]**), as long as measurement conditions allow one to calculate them in a reliable manner. In addition, the nonlinear criterion (image) can be based on subharmonics **[Sol-04]** or proper nonlinear resonances of the damaged sample.

The method should work for a large band of excitation frequencies; however, for obtaining a higher image contrast at moderate excitation intensity, the frequency can be specially optimized. Cracks or delaminations can create new resonances called Local Defect Resonances (LDRs); pumping at the LDR frequencies selectively activates these defects and produces at their locations considerable peaks of acoustic energy thus enhancing imaging contract **[Sol-19]**, **[Sol-20]**, **[Ehr-17]**. The use of the LDR explains the word "resonant" in the name of this technique.

Laser interferometry is widely used in other NDT methods based on surface acoustic field measurements. However, this specific method used continuous wave excitation and

standing/stationary wave formation without need of sharp focusing thus making it especially suitable for MMD-FEM modeling, see details in **[Ale-15]**.

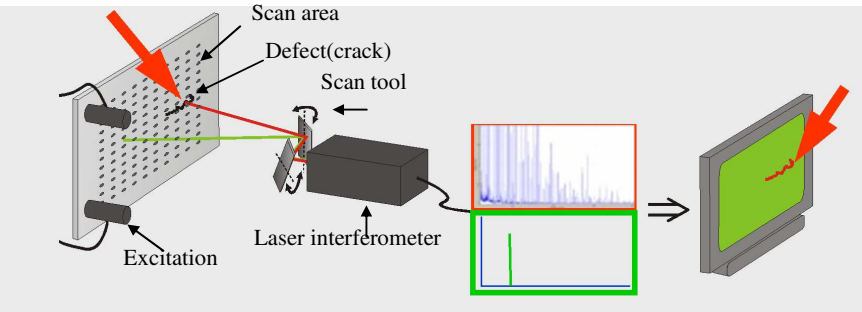

Fig. 4. Nonlinear resonant scanning laser vibrometry system scheme. The laser beam was redirected by a pair of rotating mirrors. Figure reproduced from **[Tri-17]**.

3.1.2. Scanning laser vibrometry with nonlinear frequency mixing

This method represents a modification of the previous technique, with the only difference that the sample is excited with two frequencies instead on one, and the nonlinear effect underlying measurements is based on frequency mixing rather than on harmonics generation. The lower frequency can correspond to vibration **[Gol-20]**, **[Loi-22]**. Vibrations in this nonlinear vibro-acoustic modulation technique (Fig. 5) can initiate crack opening and closing thus considerably modifying the propagation conditions for the high-frequency probe wave. The presence of sidebands in the probing frequency signal indicates the nonlinear behavior of the material resulting from the existence of defects. Conversely, an intact system with no defects exhibits a linear response without generating sidebands.

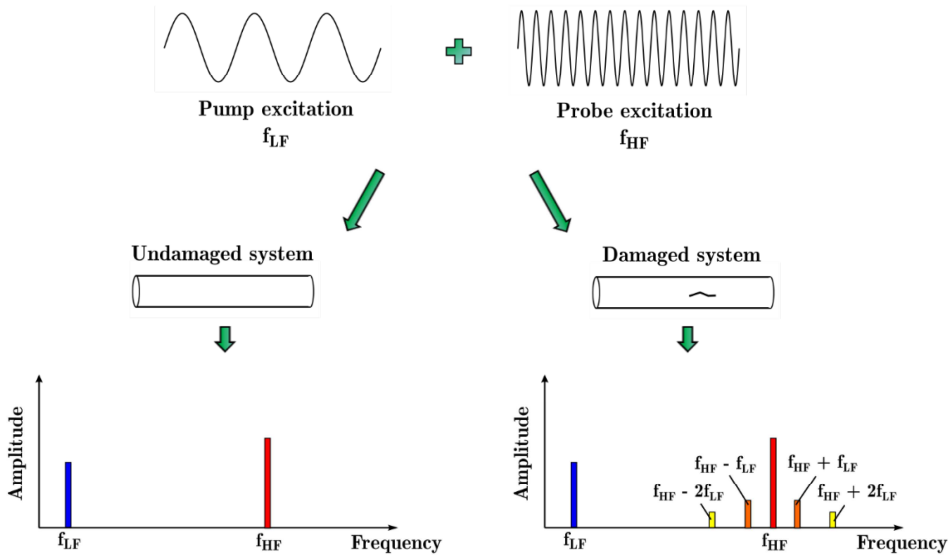

Fig. 5. Schematic representation of the nonlinear vibro-acoustic modulation technique. Figure taken from **[Loi-22]**.

In the nonlinear frequency-mixing photoacoustic imaging technique, a sample containing a crack is illuminated with two laser beams whose intensities are modulated at high and low frequencies (Fig. 6). Mixed-frequency signals are produced by the crack and are measured via laser vibrometry (actually, the third laser beam). An important advantage here is in a fully contactless detection. From the point of measuring procedure, this method can be seen as belonging to the class of laser vibrometry. The nonlinear response calculated on the basis of the generated mixed frequencies can have a maximum in the vicinity of the crack.

The creators of this novel technique **[Chi-10]**, **[Mez-20]** provide a comparison of experimental and theoretical curves to produce an estimate for geometric parameters of damage. Attempts made in this thesis are along the same line; however, our modeling tool is specially designed to have full geometric flexibility i.e. is oriented to a vast number of cases where no theoretical solution for wave propagation is possible.

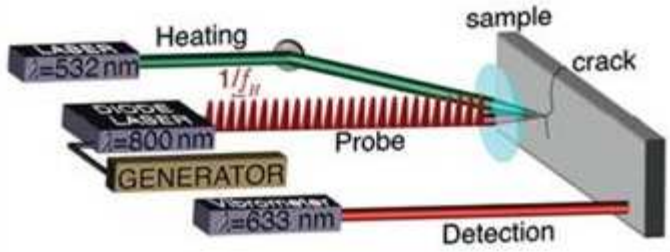

Fig. 6. Experimental setup for nonlinear frequency-mixing photoacoustic imaging to probe the crack state, sourced from **[Mez-20]**.

3.1.3. Resonant thermosonics

The method can be seen as a continuation of the previous ones that combines the ultrasonic excitation of a sample with a thermal measurement of the sample surface using a high sensitivity and a high-resolution infrared camera covering a large field of viewing area. Ultrasound-induced mechanical vibrations activate friction at the interfaces of the defect and finally generate local heating **[Sol-13]**, **[Cia-18]**. The released frictional heat diffuses from the defect to the surface of the sample in a few milliseconds, and, as a result, the local surface temperature rises very soon after the ultrasound has activated the defect (Fig. 7). In this case, the measured temperature field is much less sensitive to a particular shape of the acoustic signal, and the measured scalar temperature field contains less information for damage identification.

Again, the use of pumping frequencies corresponding to local defect resonances drastically increases the imaging efficiency and contrast, since the acoustic energy is concentrated around the defects and activates them in a selective manner.

Qualitative modeling for damage detection via thermosonics is reported in **[Tru-22]** with the use of the principles discussed in this thesis.

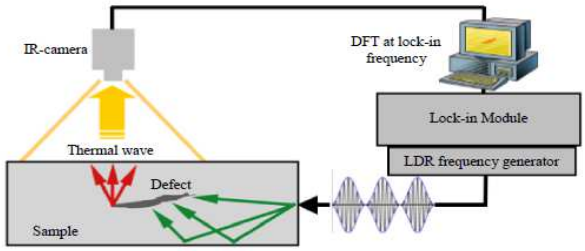

Fig. 7. Schematic diagram of thermosonics, reproduced from **[Tri-17]**.

3.2. Nonlinear imaging methods with the use of higher frequencies

In this section, we briefly discuss nonlinear imaging methods which are based not on standing wave formation but on other principles. In most of cases, the latter methods use frequencies essentially higher than in the former ones, in particular, when they require focusing on a defect. In this situation, the image resolution is comparable to the wavelength, so high frequency signals are preferable.

3.2.1. Nonlinear ultrasonic guided wave tomography

This non-destructive imaging method is capable of inspecting large areas with a fixed number of permanently attached transducers playing the role of both transmitters and receivers (Fig. 8). Multiple paths are analyzed via a special procedure that uses the difference between responses on strong and weak excitations with the proper amplitude factor to get a nonlinear damage signature **[She-12]**, **[Mar-19]**, **[Can-21], [Lee-21]**. The concept of "paths" involves high frequencies comparable to those of ray acoustics. The principle has been implemented in a number of modifications, such as a combination of Lamb waves in a plate and a so-called back-propagation algorithm **[Ter-21]** that scan the plate for defects.

3.2.2. Nonlinear ultrasonic phased array

The array generates a series of pulses with different and controllable delays which makes it possible to create a peak of acoustic energy in a given position in the sample (Fig. 9). In other words, the array works as an acoustic lens with an adjustable focal spot. Measuring a nonlinear response allows one to detect damage existing at this point; varying the focus coordinates produces an image **[Oha-19]**, **[Oha-20]**, **[Bai-20]**, **[Fie-20], [Hon-20]**. Sharp focusing requires the use of high enough frequencies but provides high-contrast robust images of damage.

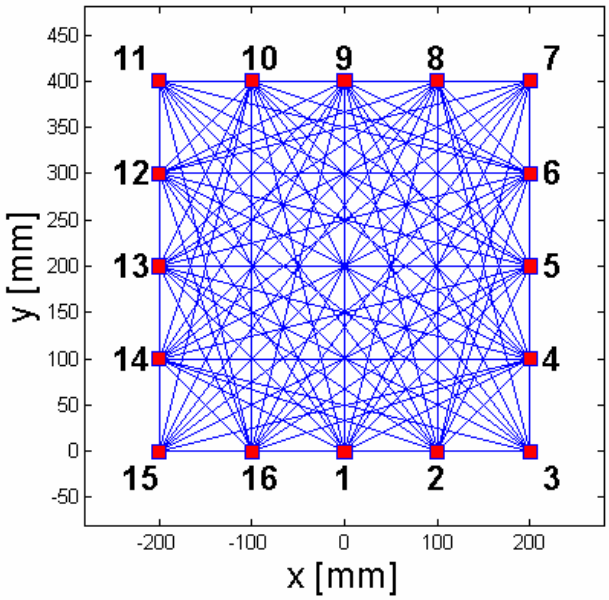

Fig. 8. Schematic of rays in the ultrasonic guided-wave based tests, figure from **[Lee-21]**.

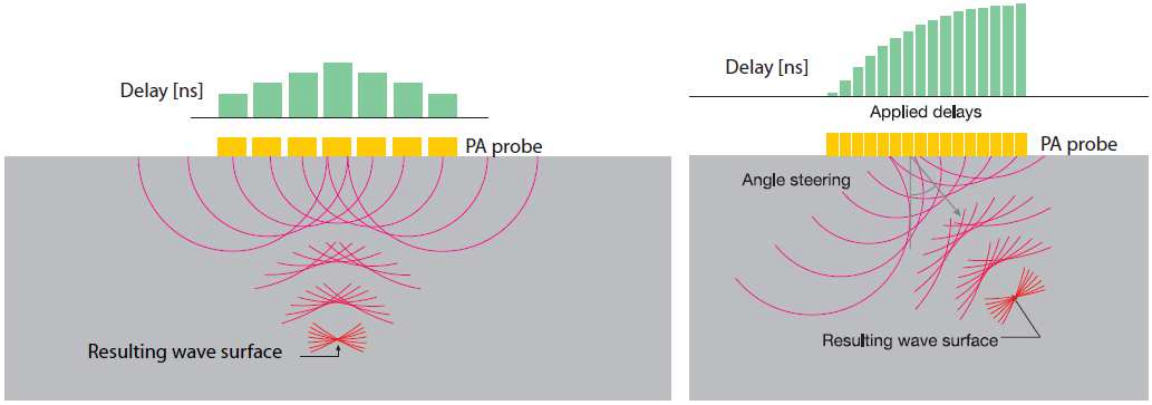

Fig. 9. Example of angled beam produced by flat probe using variable delay, figure copied from **[Hon-20]**.

3.2.3. Nonlinear time reversal acoustics

Due to the reciprocity principle, inverting all wave vectors in a wavefront results in focusing of the wave back at the source. Doing so with a nonlinear wavefield produces focusing on the nonlinear source i.e. on the defect. There exists a family of methods based on that principle **[Fin-00]**.

An example is given by Wright et al **[Wri-13],** who introduced nonlinear time reversal acoustics, an advanced method for localizing defects within structures by harnessing the principle of reciprocity and exploiting the non-linear energy emitted by the defect. This technique involves a two-step process (Fig 10).

Firstly, the signal received by the transducer(s) is time-reversed, effectively reversing the propagation path of the waves. In the time-reversed state, the receiver transducers now function as transmitters, emitting the time-reversed signal as a stimulus.

Secondly, this time-reversed stimulus is directed back towards the structure, where the non-linear energy component automatically converges and returns to the defect. By carefully analyzing the received signals, the defect can be accurately located within the structure.

To further enhance the effectiveness of the technique, the original stimulus is filtered from the time-reversed signal, resulting in an improved signal-to-noise ratio during the defect detection process. This filtering process helps to isolate the non-linear energy associated with the defect, enhancing the detection sensitivity and reducing interference from other signals.

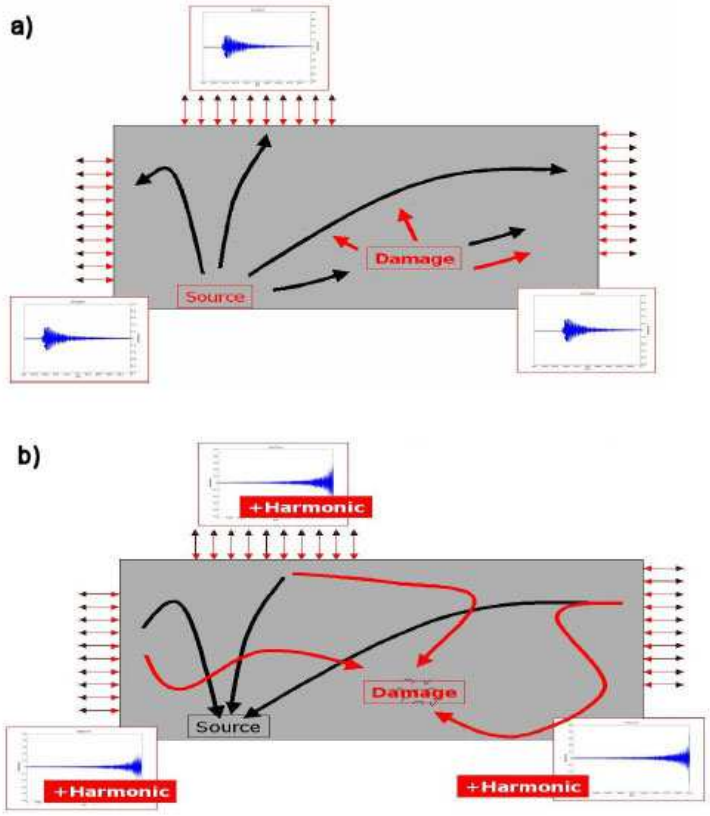

Fig. 10. **(a)** *When a structure contains a non-linear defect, the damage site produces harmonics.* **(b)** *The transmission of time-reversed signals leads to the presence of two energy concentrations - one at the original source site and the other (harmonics) at the defect, figure copied from* **[Wri-13]**.

3.2.4. Nonlinear coda wave interferometry

In numerous instances, the transmission of ultrasound through weakly attenuating materials gives rise to the emergence of coda waves, as detailed by **[Aki-75]**. These waves originate from the interference of acoustic waves, recurrently probing the same spatial region due to

multiple scattering induced by material inhomogeneities or reflections from the sample's boundaries. An acoustical receiver capturing a coda wave records a signal exhibiting quasi-chaotic characteristics, yet possessing a deterministic nature. This signal is highly responsive to subtle variations in the material's geometry or properties. Essentially, throughout multiple reverberations or scattering events, information about these changes accumulates and eventually becomes quantifiable. The material effectively functions as a natural interferometer, leading to the utilization of the method known as coda wave interferometry, characterized by its sensitivity to alterations in material properties.

By combining the above advantages with nonlinear ultrasonic techniques, a method called nonlinear coda wave interferometry has been recently proposed in **[Sni-02]**. In this case, a low-frequency pump wave is excited in the sample, while the corresponding low-frequency component in the coda signal is filtered out. If coda signals produced with and without pump wave are still different, the deviation can only be attributed to nonlinear frequency mixing due to contact acoustical nonlinearity that, in turn, reveals the presence of damage **[Zha-17]**. A combination of the technique with the time reversal principle (see Section 3.2.3) produces a method having an imaging potential **[Sma-20]**, **[Che-22].**

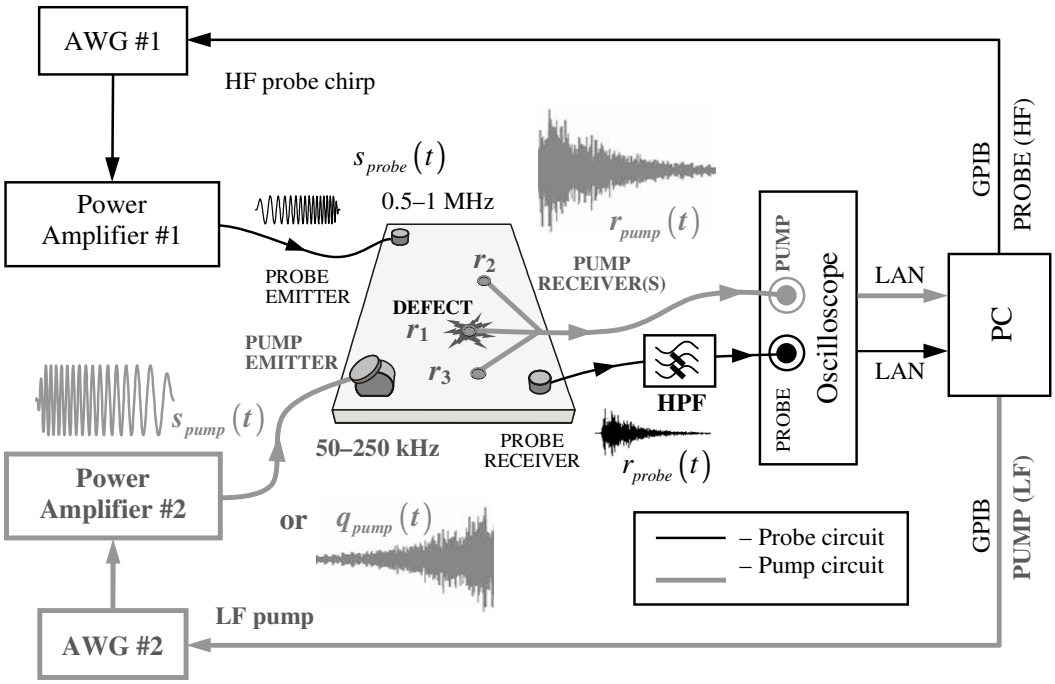

Fig. 11. Schematic of overall experimental setup nonlinear coda wave interferometry, figure copied from **[Sma-20]**.

As described in **[Sma-20]**, the scheme is illustrated in Fig. 11 where $r_{probe}(t)$ is a high-frequency coda signal which is measured and analyzed together with low-frequency reverberation signal $r_{pump}(t)$ that represents a reaction of the propagation medium on the excitation $s_{pump}(t)$ produced by the pump emitter. The low-frequency coda $r_{pump}(t)$ is required for the calculation of signal $q_{pump}(t)$ inverted in time. Then $q_{pump}(t)$ is excited by the same pump emitter to produce so-called retro-focusing of acoustic energy at the pump receiver on which $r_{pump}(t)$ was measured. The second pump wave emission is accompanied by the generation of a high-frequency signal $s_{probe}(t)$ by the probe emitter and recording of the high-frequency coda $r_{probe}(t)$ by the probe receiver. The above measurements are repeated in the presence and in the absence of the pump and for each pump receiver r_1-r_3. The difference between the reference and the perturbed codas indicates the presence of damage at the location of the pump receiver.

It is appropriate to note that coda wave is a high-frequency signal that assumes strong computational requirements once the method is attempted to numerically model for.

3.2.5. Fundamental wave amplitude difference imaging

The fundamental amplitude difference technique refers to a measurement principle that focuses on the amplitude dependence of the distortion experienced by an incident ultrasonic wave due to non-linear scatterers, as opposed to the more traditional linear scatterers. Linear scatterers typically include features like holes, grains, or slits that backscatter the incident wave. On the other hand, nonlinear scatterers encompass micro-damages such as flaws, microcracks, partially closed cracks, or dislocations, which exhibit non-linear elastic behavior resulting from interactions like clapping, slipping, or friction at the micro or nano contact level.

When an incident ultrasonic wave encounters nonlinear scatterers, a portion of the wave becomes distorted, leading to changes in its frequency content by introducing sub-harmonics and/or superharmonics. This distortion reduces the amplitude of the fundamental frequency. Importantly, this phenomenon is amplitude dependent, meaning that the response of the non-linear scatterers does not follow a proportional relationship with the amplitude of the incident ultrasonic wave **[Hau-17]**, **[Hau-19]**, Fig. 12.

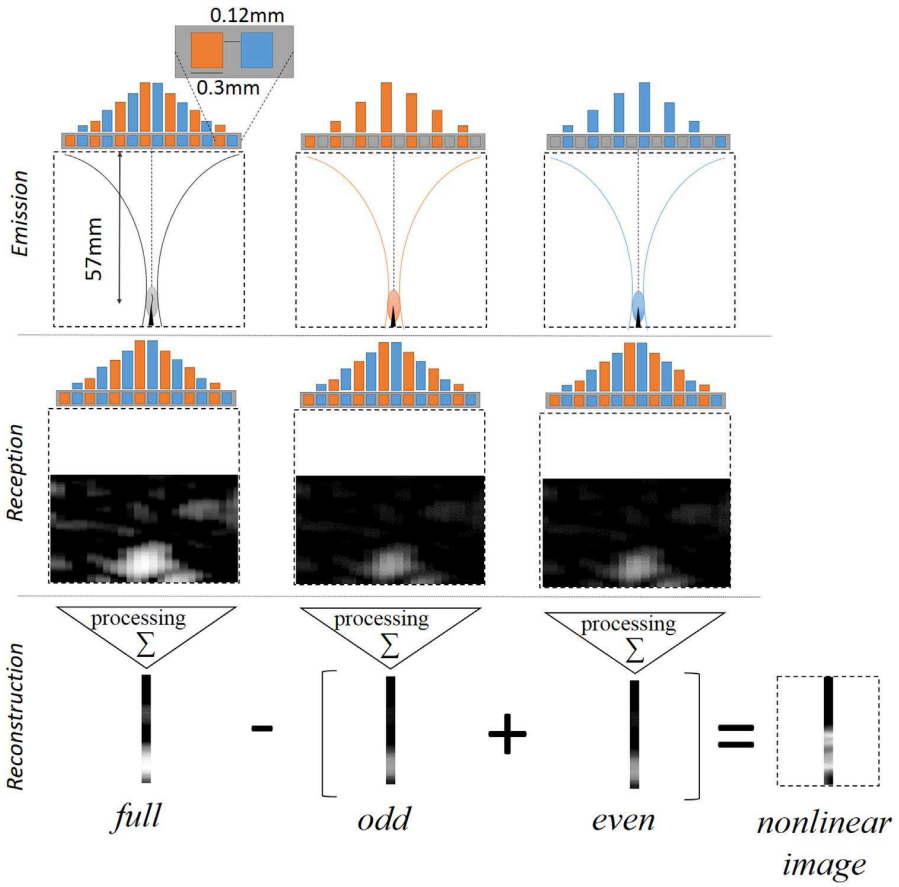

Fig. 12. Schematic of the amplitude modulation technique: sequential acquisitions with alternating element activation, filtered, shifted, and combined signals, copied from **[Hau-17]**.

3.3. Conclusion

The above brief review exemplifies several nondestructive testing and imaging methods that use the concept of contact acoustic nonlinearity. Typically they require precision measurements since the effect of acoustic nonlinearity is quite weak in real cases and can be masked by other effects. At the same time, even tiny acoustic nonlinearity detected in a purely linear system can be attributed only to presence in inner contacts and can be a manifestation of incipient damage hardly detectable by other NTD techniques.

Most of experimental methods presented here require the use of a high-frequency excitation since it predominantly impacts the final resolution depending on the wavelength. As a first step in modeling, we are going to imitate the method having a weaker requirement to the wavelength smallness. Doing that, we intend to consider an excitation wavelength comparable to the crack size hoping that the stationary wave pattern of the generated harmonics will indicate the position and the extent of damage. This idea actually underlies the nonlinear scanning laser vibrometry technique. Here we use the name is this technique in accordance to the established tradition, fully accepting the fact that the idea of using interferometric methods for measuring surface velocity is widely applied in many other NDT imaging procedures.

Chapter II: MMD-FEM modeling

In this chapter, we establish the cornerstone of our research by delving into the classical Cattaneo-Mindlin solution, also recognized as the Hertz-Mindlin solution. This exploration sets the stage for our work, which builds upon an existing framework—the Method of Memory Diagrams (MMD) and its extension, the MMD-FEM code. The finite element code for simulating acoustic waves in materials with frictional contacts was developed as a collaborative effort by researchers associated with the Joint International Laboratory LICS/LEMAC at the Institute of Electronics, Microelectronics and Nanotechnologies, UMR CNRS 8520, Villeneuve d'Ascq, France, and the Wave Propagation and Signal Processing Research Group at KU Leuven Kulak, Kortrijk, Belgium. The theoretical groundwork is outlined in **[Ale-15]**, **[Ale-16]**, **[Ale-18]** and the numerical implementation is detailed in **[Del-18]**. This code seamlessly integrates MMD-type boundary conditions at inner contacts with the finite-element formulation of solid mechanics equations within a given volume. Our research relies on this well-established model, and for a comprehensive understanding, readers are encouraged to refer to the previously mentioned foundational publications.

We express our gratitude for their collaborative efforts and valuable contributions to this research.

1. Frictional contact model based on the Method of Memory Diagrams (MMD)

Researchers at the Joint International Laboratory LICS/LEMAC, Institute of Electronics, Microelectronics, and Nanotechnologies, have extensively studied and developed a frictional contact model. This work is detailed in **[Ale-15]**, **[Ale-16]**, and **[Ale-18]**, focusing on the principles of the MMD, as explained in **[Ale-15]**. In this Section, all components of the contact model based on deformability of surface roughness and on the MMD **[Ale-15]** are described. The approach includes the normal contact solution which is independent of tangential contact interaction, while the tangential one depends on the normal loading. As a result, we build up a link between the normal and tangential contact displacements (a, b) and the normal and tangential contact loads (N, T) for an arbitrary in time excitation signal in terms of displacements. The contact loads are defined as forces applied to the bulks of the both bodies. The displacements are also defined elative to bulk parts of the bodies in such a way that the full normal displacement equals $2a$, and the tangential one equals $2b$. The

derivation is done in 2D i.e. when tangential loading always stays in one plane; a 3D generalization that provides a link between vectors $\left(a,\vec{b}\right)$ and $\left(N,\vec{T}\right)$ is also discussed.

1.1. Normal indentation of rough surfaces

In a number of traditional models of Greenwood-Williamson type **[Gre-66]**, contact between rough surfaces is described using a concept of a single asperity, i.e. an element of roughness approximating one of its summits. The asperity can be approximately seen as a sphere which immediately suggests the use of the Hertz solution linking the normal contact force and displacement. However, roughness is not something that has a certain number of summits. It represents a continuous profile or surface with actually undetermined number of individual asperities, since on top of one of them several others can be located. The approximation of continuous roughness with a fixed number of spheres, even if they are of different radii, is an ambiguous procedure. In that sense, the situation is similar to fractals that have no particular scale; any small feature hosts smaller features and so on.

At the same time, despite that we cannot count asperities, we can count contact spots appearing once contact between two surfaces is established. Below we suggest a model that does not use the concept of asperity but considers contact spots only.

The model is formulated for a physically small fragment of contact of nominal area A_n which, on one hand, is much less than the acoustic wavelength and the crack size, and, on the other hand, is much larger than microscopic scale related to roughness and contains a lot of roughness elements or features. At the scale of A_n, the surfaces are globally plane. At a given compression state, all contact spots form a real (atomic) contact area A, which is much smaller than the nominal one. At the same time, there can be introduced a geometric (truncated) contact area A_g obtained in a virtual situation when rough surfaces can freely penetrate into each other or, equivalently, when all roughness elements of each surface located higher than a certain height are virtually cut off. Two of these contact areas are also illustrated in Fig. 1. As it can be seen, A_g is also a tiny part of the nominal contact area A_n that corresponds to ideally plane surfaces. The real contact area A is a similar thing except that the roughness features do not penetrate into each others but recede under compression.

For isotropic roughness those features do not depend on a direction along the surface, the areas A and A_g can be linked via a simple model relationship. Indeed, consider a pair of rough surfaces in a certain compression state. Although each of the surfaces cannot be approximated as a collection of asperities in a unique way, a given compression makes such an approximation possible. It comes from contact spots, each of them represented as a circle, and

having an overall normal displacement a. In a virtual situation of free interpenetration, an individual circle has radius c_g, while in reality its value is different and equals c.

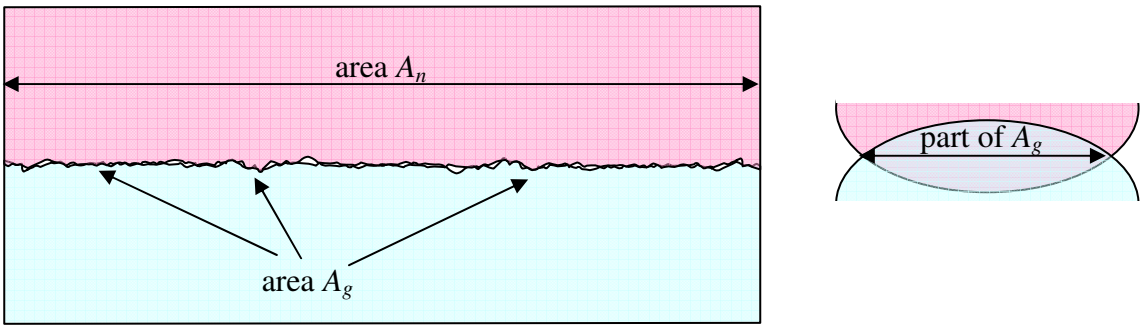

Fig. 1. Illustration of the nominal contact area A_n and the geometric contact area A_g formed by all interpenetrations in a virtual situation when surfaces can freely penetrate into each other. In reality surfaces recede under compression forming the real contact area A.

The free interpenetration case is illustrated in Fig. 2 in which values of c_g, a, R, and h are shown. It is easy to conclude that

$$h^2 = R^2 - c_g^2 = \left(R - a\right)^2. \tag{1}$$

Neglecting the small value a^2 we immediately get $c_g^2 = 2Ra$. At the same time, it follows from the Hertz solution (Eq. 8 given below) that for the physical contact when material recedes under load its squared radius $c^2 = Ra$.

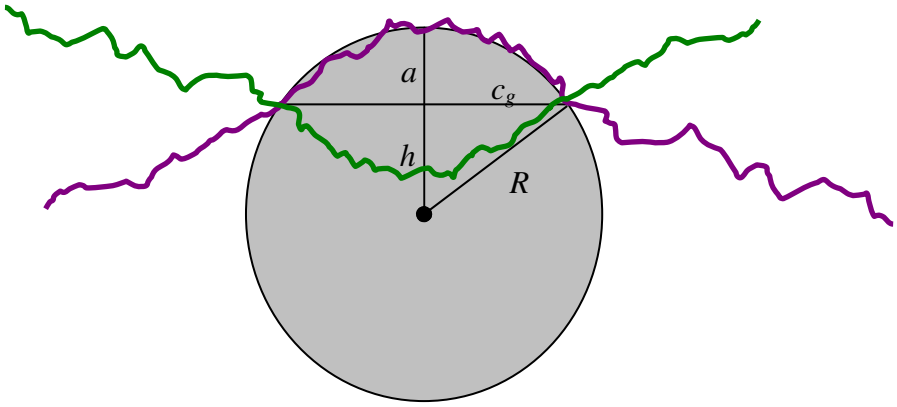

Fig. 2. Illustration for two rough surfaces that can freely penetrate into each other. They form a geometric contact spot approximated with a circle of radius c_g and is characterized by an overall displacement a.

These simple considerations provide the relation

$$\frac{A}{A_g} = \upsilon = \frac{1}{2} \tag{2}$$

linking the real contact area and the geometric one. Despite the Hertz theory provides the coefficient ½, its value denoted υ can be slightly different in reality.

It is important to note that the radius R of the approximating sphere is uniquely determined from the above relationships. This means that the concept of asperity makes sense once the compression state is defined.

Further, the proportionality $N \sim A$ was proposed by Bowden and Tabor in 1939 **[Bow-39]**; a more recent discussion on the proportionality can be found in **[Car-08]**. Both empirical and theoretical arguments suggest that

$$N = \frac{Eh'}{2\kappa\left(1-\nu^2\right)} A\,, \tag{3}$$

with h' equal to the root mean square of the random surface slope (dimensionless), and $\kappa \approx 2$ (see **[Hyu-07]** and references therein for experiments, **[Per-02]** for theory, **[Pag-10]** for the discussion on the coefficient κ, **[Pag-14]** for theoretical and numerical examples).

Finally, we introduce the random gap ξ between the surfaces (2ξ is the full gap, ξ is related to one body) and denote as $\varphi(z)$ its distribution. Then it is easy to express the ratio A_g/A_n from purely geometric consideration as

$$\frac{A_g}{A_n} = \int_0^a \varphi(z)\,dz\,. \tag{4}$$

Combining Eqs. (2)-(4) we obtain an analytical expression linking N and a,

$$N(a) = A_n \frac{\upsilon h' E}{2\kappa\left(1-\nu^2\right)} \int_0^a \varphi(z)\,dz, \quad a \geq 0\,. \tag{5}$$

In the case of negative normal displacement a, we set N equal to zero, which actually corresponds to the absence of adhesion.

Eq. (5) means that the normal reaction of a crack section is determined by the gap (aperture) distribution which, in turn, depends on the nature of a crack. Since typical acoustic excitations can always be considered as small perturbations, the normal reaction in the acoustical strain range mainly depends on the tangent to the curve $\varphi(z)$ at z=0 (i.e. the first-order Taylor series approximation). As such, three cases can be distinguished: a vertical tangent, a horizontal one, or a tangent with inclination angle between 0 and $\pi/2$. A vertical tangent implies that even for a small compressive displacement a, a non-zero contact area is immediately formed. In practice, this refers to highly conforming surfaces at the atomic level. Secondly, a horizontal tangent refers to an essentially open crack in which points in atomic contact practically do not

appear. Finally, an intermediate tangent inclination coefficient k ($0<k<\infty$) results in the approximation $\varphi(z) \approx kz$ which yields the following relationship:

$$N(a) = A_n \frac{\upsilon h' E k}{4\kappa\left(1-\nu^2\right)} a^2, \quad a \geq 0 \tag{6}$$

The same second-order dependency ($N(a) \sim a^2$) has been introduced by Biwa et al **[Biw-04]** based on existing experimental data for aluminum-aluminum contact and was already used by Yuan et al **[Yua-15]** for modeling the nonlinear interaction of a compressive wave with a soft contact interface between two solid blocks of aluminum. This suggests that the quadratic dependency is a possible approximation for two globally plane surfaces with uncorrelated roughness brought into contact. As an extension we assume that Eq. (6) is also approximately valid for fatigue cracks since the internal stresses released during cracking and the associated microscopic displacements result in a similar loss of conformity at the atomic scale. Micro-scale composite roughness that mainly contributes to the acoustic response can thus be considered as uncorrelated.

The quadratic approximation is not the only possible form for modeling the normal load-displacement relationship. In **[Poh-12]**, **[Poh-13]** it is shown that rough surfaces with various fractal dimensions correspond to different powers in approximation of the kind of Eq. (6). Nevertheless, based on experiments **[Biw-04]**, we here accept Eq. (6) as a model equation for the normal reaction curve keeping in mind that, for the proposed theory, the specific form of $N(a)$ is not essential.

Certainly, a tangential excitation may considerably displace the contacting asperities in the lateral direction and therefore alter the normal reaction curve $N(a)$. However, this effect can be neglected if we assume that the random gap between the crack surfaces is a stationary process of which the characteristics h' and $\varphi(z)$ do not depend on the tangential shift. Therefore, $N(a)$ is supposed to be a portrait of the system which is not affected by any other interactions, and incorporates all geometric information about the rough surfaces in contact.

1.2. Cattaneo-Mindlin problem

Similarly to other semi-analytical methods in contact mechanics, the MMD can be regarded as a direct generalization of the classical Cattaneo-Mindlin **[Cat-38]**, **[Min-53]** solution developed for elastic spheres in contact loaded by a subsequent application of constant normal and tangential forces. As it was shown, the contact zone consists of stick and slip areas that represent a central circle and outer annulus, respectively. In the stick zone, no relative tangential displacement between close points belonging to the opposite surfaces is possible. In

the slip zone, the shear stress τ equals the normal stress σ times the friction coefficient μ, in accordance to the Coulomb friction law. At the same time, in that zone, the relative tangential displacement is a nonzero vector that must be directed as the local shear stress vector. The latter condition can be called the orientation aspect or property of the Coulomb friction law.

The most compact derivation **[Jäg-95]** is based on a superposition of the Boussinesq solutions for rigid punches straining an elastic half-space in both normal and tangential directions. The smallest punch in the superposition coincides with the stick circle that guarantees the no-slip condition in the stick zone, and the largest one has obviously the size of the contact zone itself. By a proper choice of "strengths" of the punches in the normal and tangential directions it is possible to satisfy the Coulomb condition $\tau=\mu\sigma$. However, the orientational property is satisfied only approximately. The matter is that for punches applied in the *x*-direction parallel to the half-space surface, the local vectors $\vec{\tau}$ are all directed along the same *x*-axis, while the tangential displacement vector has a non-zero in-plane *y*-component (Eq. (28c) in **[Jäg-95]**. Another simplification is related to the neglect of the second term in the second line of Eq. (28b) in the cited paper. In addition, the Catteneo-Mindlin approximation disregards dissimilarity phenomena **[Mun-94]** which, if present, can produce local tangential displacement for purely normal compression, since the Poisson effect can be of the different magnitude for non-equal spheres of different materials. However, despite some assumptions in the analysis, the Cattaneo-Mindlin solution remains a good approximation to frictional contact interaction of axisymmetric bodies largely used since 1950s. For equal spheres of radius R with the elastic constants E and ν shown in Fig. 3 (contact forces N and T, displacements a and b understood hereafter as one-half of total displacements, contact zone radius c and stick zone radius s) the solution has the following form:

$$N = \frac{4E^*}{3R}c^3, \tag{7}$$

$$a = \frac{1}{R}c^2, \tag{8}$$

$$T = \frac{4\mu E^*}{3R}\left(c^3 - s^3\right), \tag{9}$$

$$b = \frac{\mu\theta}{R}\left(c^2 - s^2\right). \tag{10}$$

with E^* and θ defined as

$$E^* = \frac{E}{2\left(1-\nu^2\right)}, \tag{11}$$

$$\theta = \frac{2-\nu}{2(1-\nu)}. \tag{12}$$

In this solution, all geometric features of the contact system are taken into account through the dependences $N = N(c)$ and $a = a(c)$ in Eqs. (7) and (8) that represent the classical Hertz solution. The result can be rewritten using these functions as

$$\begin{cases} b = \theta\mu\left(a(c) - a(c=s)\right) \\ T = \mu\left(N(c) - N(c=s)\right) \end{cases} \tag{13}$$

where in the last terms of each equation the argument of functions $N(\cdot)$ and $a(\cdot)$ is the radius of the stick zone s. The result Eq. (13) is frequently referred to as the reduced elastic friction principle **[Jäg-05]**. The principal Eq. (13), in contrast to Eqs. (7)-(10), is valid for any axisymmetric contact geometry, not necessarily spherical.

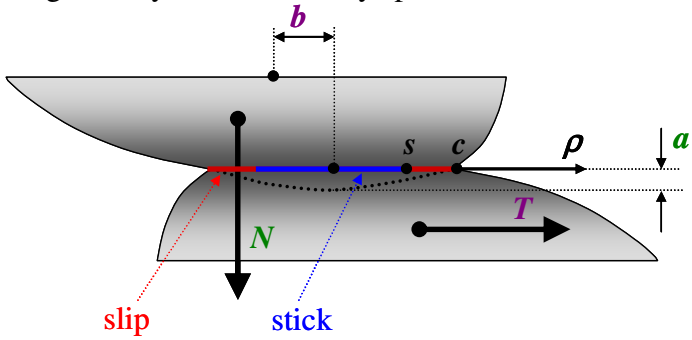

Fig. 3. Geometry of the Cattaneo-Mindlin problem and important parameters, figure taken from **[Ale-20]**.

The same principle applies to local stresses and displacement fields. It has been shown **[Jäg-98]**, **[Pop-15]** that

$$\begin{cases} w(\rho) = \theta\mu\left[u(c,\rho) - u(s,\rho)\right] \\ \tau(\rho) = \mu\left[\sigma(c,\rho) - \sigma(s,\rho)\right] \end{cases} \tag{14}$$

where $w(\rho)$ and $\tau(\rho)$ is the local tangential displacement field and shear stress, respectively, and $u(c,\rho)$ and $\sigma(c,\rho)$ are corresponding tangential characteristics obtained when the contact size equals c. In accordance to the accepted notations, $u(s,\rho)$ and $\sigma(s,\rho)$ are the normal displacement field and the normal stress distribution existing in a virtual case where the contact size equals s, a smaller than c value that corresponds to the actual stick zone radius.

It is straightforward to see that $\tau = \mu\sigma$ in the slip zone $s < \rho < c$, since the normal stress is nonzero only if its first argument is higher than the second one. At the same time, it is

possible to check **[Jäg-95]** that in the stick zone $\rho < s$ the tangential displacement field $w(\rho)$ is constant i.e. surface deformation on the stick zone is that of a rigid body. The above two properties are in accordance to the Coulomb friction law formulated locally i.e. at an arbitrary contact point.

In Fig. 4, stress and local displacement distributions are illustrated for two spheres in contact. It is appropriate to cite here the corresponding exact solutions **[Pop-15]**:

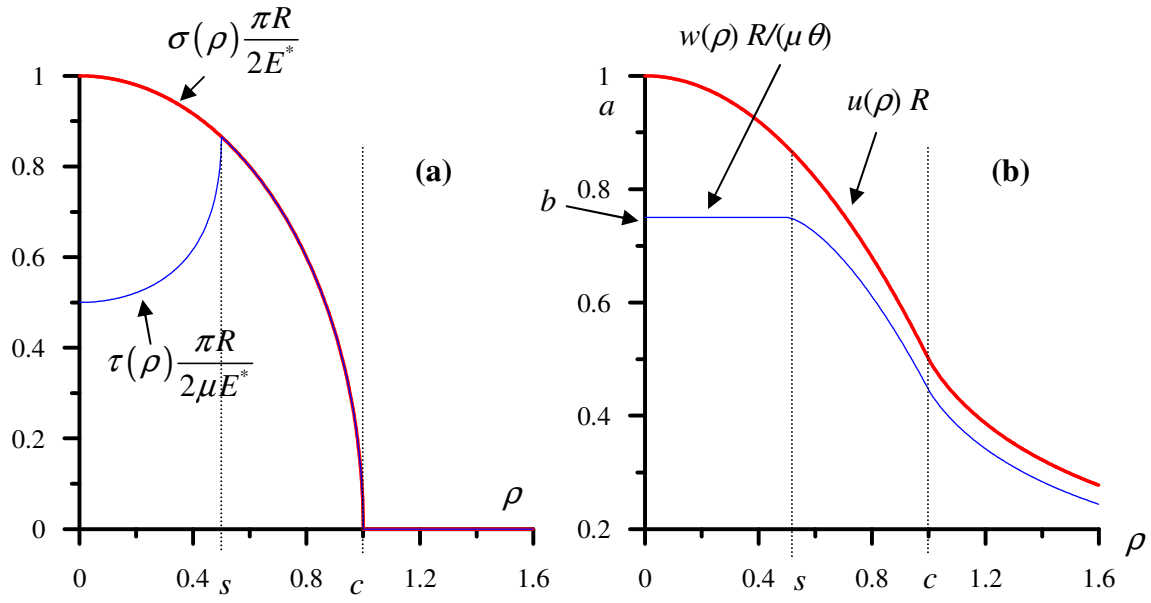

Fig. 4. Distributions of contact stresses $\sigma(\rho)$ and $\tau(\rho)$ **(a)** *and of local contact displacement fields $u(\rho)$ and $w(\rho)$* **(b)** *for spherical profiles calculated in accordance to Eqs.* (15)-(18). *It is straightforward to verify the fulfillment of the Coulomb friction conditions: stresses coincide in the slip zone $s<\rho<c$ with factor μ, while the tangential displacement field $w(\rho)$ is constant and equal b in the stick zone $\rho<s$. Here the radial coordinates are normalized on the contact radius c.*

$$\sigma(\rho) = \frac{2E^*}{\pi R}\sqrt{c^2 - \rho^2} \tag{15}$$

$$\tau(\rho) = \frac{2\mu E^*}{\pi R}\begin{cases} \sqrt{c^2-\rho^2} - \sqrt{s^2-\rho^2}, & \rho < s \\ \sqrt{c^2-\rho^2}, & s < \rho < c \\ 0, & x > c \end{cases} \tag{16}$$

$$u(\rho)=\begin{cases}\dfrac{2c^2-\rho^2}{2R}, & \rho<c\\ \dfrac{1}{\pi R}\left(\arcsin\left(\dfrac{c}{\rho}\right)\left(2c^2-\rho^2\right)+c\sqrt{\rho^2-c^2}\right), & c<\rho\end{cases} \tag{17}$$

$$w(\rho)=\frac{\mu\theta}{R}\begin{cases}c^2-s^2, & \rho<s\\ \dfrac{1}{2\pi}\left(\arcsin\left(\dfrac{s}{\rho}\right)\left(2\rho^2-4s^2\right)-2s\sqrt{\rho^2-s^2}+2\pi c^2-\pi\rho^2\right), & s<\rho<c\\ \dfrac{1}{\pi}\left(\arcsin\left(\dfrac{c}{\rho}\right)\left(2c^2-\rho^2\right)-\arcsin\left(\dfrac{s}{\rho}\right)\left(2s^2-\rho^2\right)+c\sqrt{\rho^2-c^2}-s\sqrt{\rho^2-s^2}\right), & c<\rho\end{cases} \tag{18}$$

1.3. Method of memory diagrams for partial slip

The above solution is valid in the case where a constant normal force/displacement is applied to the contact system followed by an application of constant tangential force/displacement. Since the solution is quasi-static, the actual time dependence of any signal is not important, and the instantly arising tangential action can be seen as monotonously increasing. This situation can be called “simple loading” and is illustrated in Fig. 5 (a). In addition, slip here can only be partial i.e. the stick zone, even of a tiny radius, must remain at the contact center.

To mimic an acoustic excitation, both normal and tangential forces (or displacements, depending on what is considered as argument) should evolve simultaneously in a non-monotonous way. Changes in the normal force or displacement are easy to take into account since the normal solution Eq. (6) is fully reversible once we neglect adhesion and plasticity. However, the tangential solution **[Min-53]** is hysteretic. It has a simple form Eqs. (13)-(14) only for positive direction of the tangential force that results in slip of positive (by convention) sign. If the tangential force starts decreasing, the slip occurs in the opposite direction. To account for that, a superposition of solutions **[Min-53]** should be considered that provides the condition $\tau=\pm\mu\sigma$ in the slip zone, with a proper sign.

A more recent generalization of this principle is provided by the Method of Memory Diagrams, the MMD **[Ale-15]**, **[Ale-18]**. The method develops the idea described in the previous section by applying it to more general loading histories which consist in arbitrarily changing oblique compression in 2D or in 3D (the former means that the normal and tangential forces stay in one plane). The calculation is organized with the use of an auxiliary

internal dimensionless function $D(\rho)$ called memory diagram that encodes all memory information in the frictional system. In 2D, the solution reads

$$\begin{cases} b = \theta\mu \int_0^c D(\rho) \left.\frac{da}{dc}\right|_{c=\rho} d\rho \\ T = \mu \int_0^c D(\rho) \left.\frac{dN}{dc}\right|_{c=\rho} d\rho \end{cases}. \tag{19}$$

In the previously considered "simple loading case" (Fig. 5(a)) i.e. when the tangential action is added after application of constant normal compression, the memory diagram has a simple rectangular shape that corresponds to the classical result Eq. (13) after calculation of the integral in Eq. (19).

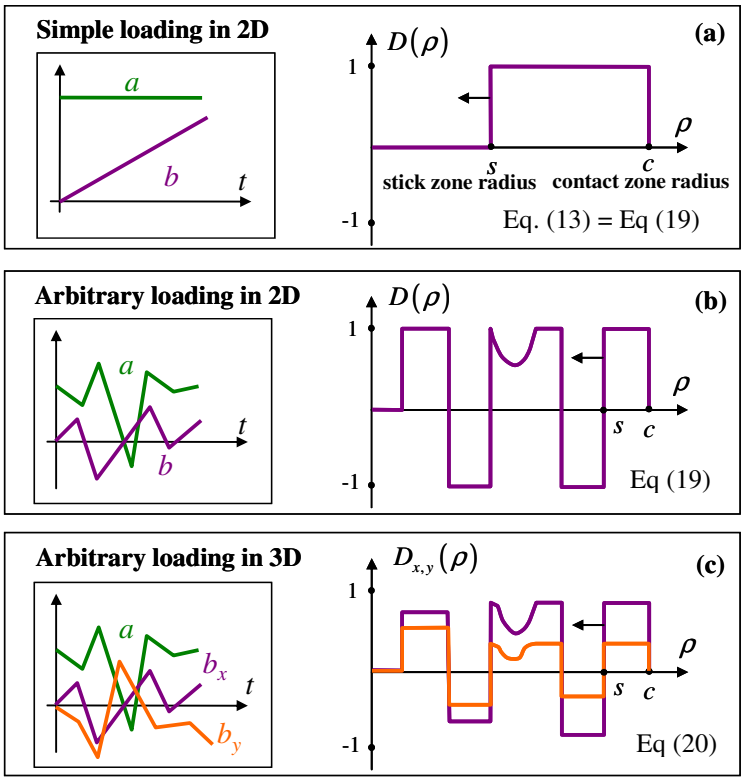

Fig. 5. Illustration for the MMD: loading histories at the left and memory diagrams at the right, for the simple loading **(a)**, *arbitrary loading in 2D* **(b)** *and in 3D* **(c)**. *Here* $s<\rho<c$ *is the slip annulus, see also Figs. 3 and 4. Rectangular fragments in* **(b)** *and* **(c)** *correspond to residuals of previous partial slip events of the kind* **(a)**. *Curvilinear sections are explained in detail in* **[Ale-15]**.

An arbitrary loading history in 2D corresponds to a more complex shape of the memory diagram that can consist of positive and negative horizontal elements as well as from curvilinear sections (Fig. 5(b)). The algorithm **[Ale-15]** keeps track on the evolution of the

loading parameters and updates the diagram shape accordingly, in order to keep the balance equation Eq. (19). This formula does not require any additional assumptions in comparison to the reduced elastic friction principle Eq. (13). Limitations related to this principle are discussed by **[Jäg-05]** and also mentioned in the paper **[Ale-15]** where the MMD in described in more detail.

If now the loading parameters are allowed to arbitrarily vary in 3D, the system can be described via a vector counterpart of Eq. (19), which reads

$$\begin{cases} \vec{b} = \theta\mu \int_0^c \vec{D}(\rho) \left.\dfrac{da}{dc}\right|_{c=\rho} d\rho \\ \vec{T} = \mu \int_0^c \vec{D}(\rho) \left.\dfrac{dN}{dc}\right|_{c=\rho} d\rho \end{cases}. \tag{20}$$

A detailed analysis **[Ale-16]** show that the 3D solution should be considered as an approximation.

Eqs. (19) or (20) together with algorithm governing the memory diagram evolution provide the possibility to calculate the hysteretic tangential load-displacement relationship through the known normal load-displacement relationship given by $N = N(c)$ and $a = a(c)$. It is easy to get rid of the radial coordinate ρ by a proper substitution of variable. For the force-driven system solutions Eq. (13) can be written as

$$\begin{cases} b = \theta\mu\left(a(N) - a(Q)\right) \\ T = \mu\left(N - Q\right) \end{cases} \tag{21}$$

where $a(N)$ is the normal displacement-load curve (inverted Eq. 6) and $Q = N(c = s)$ in Eq. (13). Similarly, for the displacement-driven system

$$\begin{cases} b = \theta\mu\left(a - q\right) \\ T = \mu\left(N(a) - N(q)\right) \end{cases} \tag{22}$$

where $N(a)$ is the normal load-displacement curve and $q = a(c = s)$ in Eq. (13). Correspondingly, the MMD solutions read

$$\begin{cases} b = \theta\mu \int_0^N D(\eta) \left.\dfrac{da}{dN}\right|_{N=\eta} d\eta \\ T = \mu \int_0^N D(\eta)\, d\eta \end{cases} \tag{23}$$

and

$$\begin{cases} b = \theta\mu\int\limits_0^a D(\alpha)\,d\alpha \\ T = \mu\int\limits_0^a D(\alpha)\left.\dfrac{dN}{da}\right|_{a=\alpha} d\alpha \end{cases}, \tag{24}$$

for the force-driven and displacement-driven systems, respectively, with inner integration variables $\eta = N(c=\rho)$ and $\alpha = a(c=\rho)$ in defined via functions $N(c)$ and $a(c)$.

The use of Eqs. (23)-(24) simplifies the treatment since those equations do not contain any geometry-related variables explicitly. The contact geometry only contributes into the normal load-displacement curve $N(a)$ or its inverted counterpart. The description Eq. (19) is fully symmetric with respect to forces and displacements. Each pair (a, b) or (N, T) can be considered as an argument thus making the other pair function.

1.4. Account for total sliding and contact loss

As it was mentioned, the method works when the forces are considered as arguments and displacements are unknown or vice versa. At the same time, it is important to emphasize that the MMD introduced above is only valid for partial slip i.e. when some stick zone remains around ρ=0. If $|T|$ reaches μN or $|b|$ reaches $\theta\mu a$, the stick zone disappears. The force-driven system excited by a tangential force exceeding μN will experience accelerated movement, which violates the current quasi-static character of description and generally complicates the problem. Fortunately, in the case where the system is driven by displacements, there exists a simple way to construct a quasi-static force-displacement relationship valid in all situations, which may be encountered: partial slip, total sliding, and contact loss.

To do so, we introduce two displacement components of the total displacement

$$b = b_0 + \tilde{b}\,. \tag{25}$$

as illustrated in Fig. 6.; $\tilde{b}$ reflects deformation of one of the contacting bodies due to shearing, while b_0 is a tangential shift between the contact centers that develops due to total sliding. Since we anyway consider small displacements in comparison to all geometric features, the effects of the slight drop of the upper body because of the tangential mismatch or contact plane rotation are neglected.

For the 2D case, the algorithm that provides the unknown tangential force is shown in Fig. 7. When the contact is lost, there is no contact interaction, and the bodies are unstrained, i.e. $N = T = 0$. When total sliding takes place, $T = \pm\mu N$ with the sign depending on the sliding

direction. Finally, for partial slip the MMD algorithm has to be applied, which is symbolically expressed as $T = MMD\left(\tilde{b}\right)$. In each case, one of the components, b_0 or $\tilde{b}$, is known directly, and the other one is immediately found since their sum equals the known argument. Numerically, the algorithm is applied to small increments Δb and Δa, and updates previous values with small changes calculated at the current step which become previous values at the next step, etc.

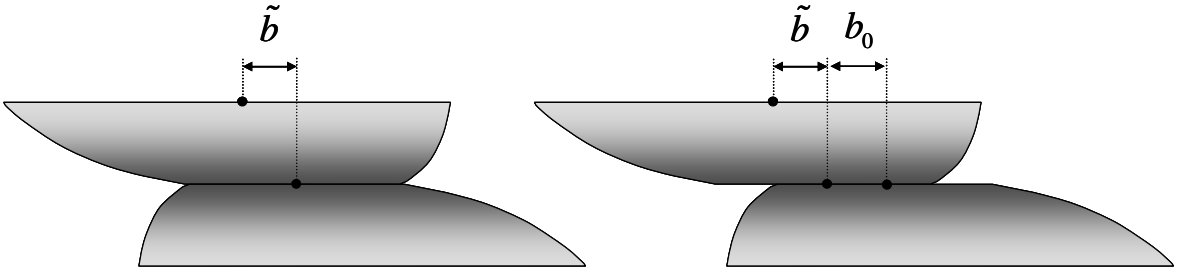

Fig. 6. Partial tangential displacements due to shearing of the bodies and due to the shift between contact centers, figure taken from **[Ale-20]**.

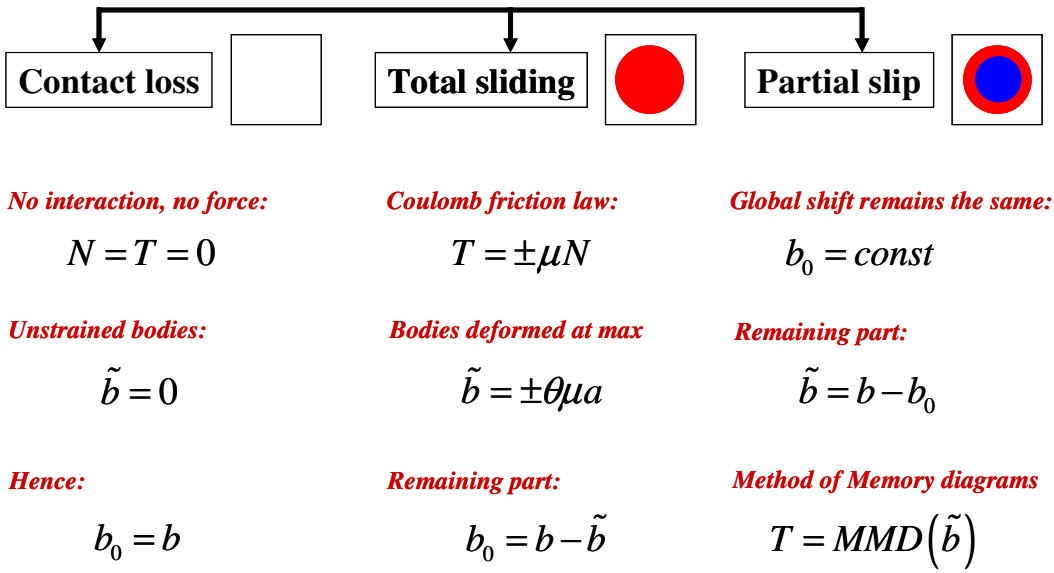

Fig. 7. Three contact states (contact loss, total sliding, and partial slip) and the corresponding solutions for T obtained via repartition $b = b_0 + \tilde{b}$ for loading in 2D (normal and tangential displacements always stay in one plane). More explanations in **[Ale-20]**.

In the 3D loading case, tangential displacement b, its components b_0 and $\tilde{b}$, and force T in Fig. 7 become vectors. In addition, the formulas for the total sliding case have to be further modified since sliding occurs not in the positive or negative direction as in 2D, but in a

direction given by the unit vector $\vec{l} \uparrow\uparrow \Delta\vec{b}_0$ where $\Delta\vec{b}_0$ is an infinitesimal slip vector, and symbol $\uparrow\uparrow$ denotes collinearity. These vectors are also collinear with the tangential force, $\vec{l} \uparrow\uparrow \vec{T}$, since slip is caused by $\vec{T}$ (orientational aspect of the Coulomb friction law). From the previous considerations we also know that $\left|\vec{\tilde{b}}\right| = \theta\mu a$ (assume s=0 in Figs. 3-5(a) or in Eq. (13)). Then the repartition Eq. (25) takes the form

$$\vec{b} = \vec{b}_{0p} + \Delta\vec{b}_0 + \vec{l}\,\theta\mu a \tag{26}$$

in which $\vec{b}_{0p}$ is the known component $\vec{b}_0$ at the previous step, and the two last vectors are collinear. Finally, $\vec{l}$ is obtained as a unit vector collinear to

$$\vec{l} \uparrow\uparrow \vec{b} - \vec{b}_{0p}, \tag{27}$$

and then $\vec{T} = \vec{l}\,\mu N$. The infinitesimal slip vector $\Delta\vec{b}_0$ becomes equal $\Delta\vec{b}_0 = \vec{b} - \vec{b}_{0p} - \vec{l}\,\theta\mu a$ which means that all components of the repartition Eq. (26) at the current step are determined.

For brevity, the term MMD comprises the extension to the contact loss and total sliding cases (Fig. 7), not only the partial slip situation in Eqs. (19), (23), and (24). The formulation shown in Figs. 5 and 7 illustrates the efficiency of the method. Indeed, instead of considering detailed evolving distributions of local stresses and displacements, it is enough to introduce and update one inner memory function (two functions in 3D). Moreover, the function frequently contains constant segments thus allowing to memorize only the beginning and the end of each segment and not all intermediate points. The MMD algorithm is based on an adaptive grid whose points are created and deleted following the loading protocol instead of being predefined at fixed positions. As a result, the method is especially suitable to complex loading protocols such as random or acoustical excitation. At the same time, the contact geometry should remain relatively simple in order to be imitated by axisymmetric shapes.

In conclusion, it is instructive to provide an example of the tangential load-displacement curve calculated for an exemplar displacement history. In Fig. 8 we show it together with the normal one **(a)** which does not depend on loading history and is approximated here by the simple quadratic dependence Eq. (6). In contrast, the tangential curve **(b)** is hysteretic and is of complex shape depending on loading history shown at the left.

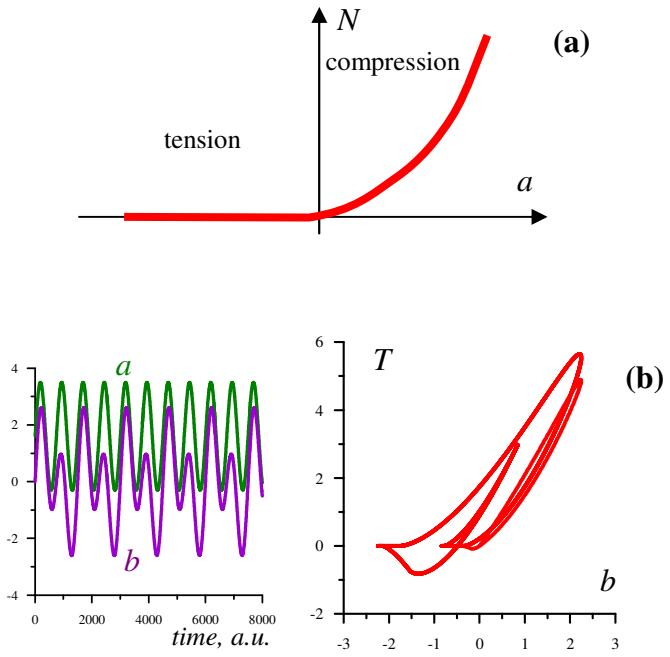

Fig. 8. Normal load-displacement curve considered **(a)** *is independent on loading history while the tangential one depends on it* **(b)**. *All forces and displacements are measured here in arbitrary units.*

1.5. Isotropically rough surfaces and axisymetric bodies

Deriving the semi-analytical link between the tangential force and displacement we actually addressed axisymmetric bodies in the Cattaneo-Mindlin approximation. However, there exist arguments showing that the method should be approximately valid for rough surfaces as well.

Indeed, suppose that contact of rough surfaces is represented as a collection of contacts between spherical asperities of different radii and height. The considered contact system will have a certain normal response $N(a)$ determined as a superposition of Hertz solutions Eqs. (7)-(8). It is possible to find another (effective) axisymmetric contact pair having the same normal response. This possibility is guaranteed by the known normal contact solution **[Gal-61]**, **[Jäg-95]** valid for an arbitrary contact profile characterized by the gap $z(\rho)$ between bodies in contact:

$$N = \frac{2E}{1-\nu^2}\left(ca - \int_0^c \frac{\rho z(\rho)}{\sqrt{c^2-\rho^2}} d\rho \right), \tag{28}$$

$$a = \int_0^c \frac{cz'(\rho)}{\sqrt{c^2-\rho^2}} d\rho, \tag{29}$$

Eqs. (28)-(29) provide an indirect link between a and N for a given $z(\rho)$ and potentially can be inverted to have the gap profile $z(\rho)$ for a known (say, quadratic) dependence $N(a)$. Then, the procedure of the tangential response calculation can be applied to that effective axisymmetric contact pair. In accordance to the reduced elastic friction principle Eqs. (13), two contact systems having the same normal response will also have identical tangential responses. The derivation **[Ale-15]** should be valid in this case as well.

For axisymmetric bodies in contact the valued N and T represent forces. For fragments of rough surfaces with nominal area A_n, it is more convenient to introduce average contact stresses N/A_n and T/A_n. In what follows, we renormalize forces N and T on A_n and call then loads in order to avoid a confusion with stress distributions $\sigma(\rho)$ and $\tau(\rho)$ for equivalent axisymmetric bodies. To comply with that, we rewrite Eq. (6) as

$$N(a)=\begin{cases}\dfrac{\upsilon h' Ek}{4\kappa\left(1-\nu^2\right)}a^2 \equiv C^2a^2, & a\geq 0\\ 0, & a<0\end{cases} \tag{30}$$

dropping A_n here. The corresponding tangential load T will also have the dimension of pressure.

Here parameter C introduced by Biwa **[Biw-04]** characterizes primarily the composite roughness of the crack faces. Remember that h' is the root mean square of the random surface slope and k is the tangent to the random gap distribution, while the other parameters are approximate constants, $\kappa \approx 2,\ \upsilon \approx 1/2$. For two globally smooth aluminum blocks of unspecified roughness measurements presented in **[Biw-04]** produced an estimation $C = 6\cdot 10^6\ Pa^{1/2}m^{-1}$. It is expected that a gap between crack surfaces is broader than between two globally smooth blocks, which means that k can be considerably lower. Anyway, contact of rough surfaces should be less stiff than one of smooth blocks, therefore the reported value of C should be considered as the highest estimation. In our modeling we use lower values.

2. Finite element description for acoustic waves in materials with frictional contacts

Researchers from the Wave Propagation and Signal Processing Research Group at KU Leuven Kulak, Kortrijk, Belgium, worked together to create a finite element code for simulating acoustic waves in materials with frictional contacts. You can find more details about how it works in reference **[Del-18]**. The load-displacement relationship obtained in the previous section represents a semi-analytical description i.e. given by a number of analytical

solutions with parameters determined by the algorithm. Previously **[Del-18]** it was coded as a user-defined boundary condition in a standard finite element package (COMSOL). In this thesis, the existing code has been modified to compute the solutions in a large number of new cases presented in the next Chapters. An important addition is a study of convergence of the numerical procedure accompanied by some optimization efforts. The latter results in a special selection of discretization parameters (time step and mesh element size) that produces a given precision for lesser computation time.

2.1. Combining MMD and FEM

The extended version of the MMD taking into account three possible contact states provides boundary conditions in the form of contact loads N and T calculated for any displacement history $\left(a(t),b(t)\right)$. COMSOL accepts user-defined boundary conditions, not necessarily expressed in closed form equations, but equally well as an external algorithm written in MATLAB and connected to COMSOL using the LiveLink feature for MATLAB **[Liv-18]**. This allows a relatively complex MMD-based algorithm to be directly incorporated in COMSOL and hence, ensures a simple and explicit procedure of data exchange between the crack model and the solid mechanics unit in COMSOL, organized as follows:

(a) In the Structural Mechanics Module of COMSOL, normal and tangential stresses, defined by appropriate boundary conditions, are used for calculating normal and tangential displacements defined at each contact surface at a particular time step of the procedure. The relative normal and shear displacements calculated at the discretization points on the contact interface (called integration points or Gauss points) are stored as outputs of the COMSOL module and considered as an input for the MATLAB code.

(b) The calculated relative displacement values at all Gauss points on the contact interface are used as an input in the displacement-driven crack model (MATLAB code), in order to determine the corresponding stress values at these positions, which in turn are transferred to COMSOL to update the boundary conditions at the contact interface.

(c) Steps (a) and (b) are repeated for the next time step, until the desired calculation time is reached.

Using this approach, the final model thus contains two components: the constitutive model for cracks with rough surfaces implemented in MATLAB and the wave propagation model implemented in the Structural Mechanics Module of COMSOL. It is important to stress again that accounting for roughness does not mean that internal roughness meshing is used. The roughness is only present on the microscopic level of the crack model, whereas at the

mesoscopic level crack faces are considered and modeled as globally flat. The scheme of data exchange is presented in Fig. 9.

The simulations considered here are in 2D because of high computational demands associated to an attempt to reproduce a real experimental method. In a simpler case, first results in 3D geometries have been obtained **[Ale-19]** with the use of the 3D MMD version formulated in **[Ale-16]**.

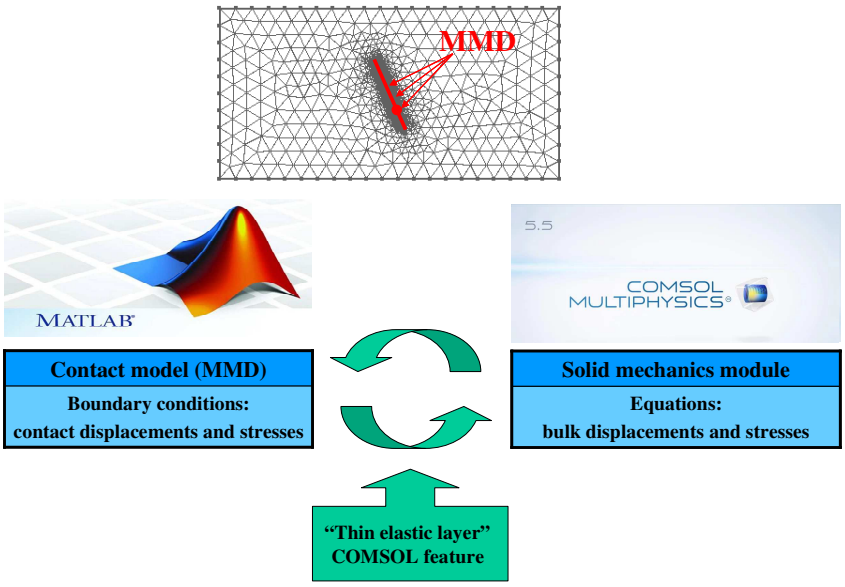

Fig. 9. Illustration of MMD-FEM code structure.

2.2. Convergence studies and optimization

Initiating our research, we build upon the previously developed MMD-FEM code for simulating acoustic waves in materials with frictional contacts. Our sincere thanks go to our researchers at the I.E.M.N. laboratory in France and the Wave Propagation and Signal Processing Research Group in Belgium. Their collaborative efforts and invaluable contributions have been instrumental in laying the essential foundation for this research. Before employing the existing code, we initiate our thesis work by executing two fundamental technical steps, thereby establishing a robust foundation for our research. Firstly, since the model generates unique results in the sense that they cannot be compared with any other model in any particular case, error estimation can be made only via convergence analysis. Secondly, the convergence analysis grants an opportunity to adjust space and time discretization in an optimal way. In other words, we have to avoid a situation when too fine time discretization is used together with very coarse spatial meshing and vice versa. Moreover, there is one more technical detail that should be checked. Ideally, values of N and T coincide with the respective stresses at all points where the boundary condition is posed. In

practice, they can be slightly different as the stresses are defined by an internal COMSOL solver. The corresponding error also characterizes the computational precision of the entire procedure.

The study has been conducted in the following case. The model geometry consists of a rectangular aluminum domain of 150 mm width and 30 mm height, as illustrated in Fig. 10. The aluminum sample has density ρ = 2700 kg/m^3, Young's modulus E = 70 GPa, and Poisson's ratio ν = 0.33. A vertical crack with a depth of 15 mm is positioned at distance of 25 mm from excitation side. At the side boundary of the sample, a shear excitation with a frequency f = 80 kHz in a segment of 10 mm at height of 10 mm from bottom surface is defined by specifying a vertical (i.e. in y-direction) displacement boundary condition in the form

$$u_y = A\sin\left(2\pi ft\right), \quad t < T_{exc}, \tag{31}$$

where A the excitation amplitude (10 nm, corresponds to typical acoustics strains of 10^{-6}) and T_{exc} is the excitation duration of 125 μs (that equals about 5 times of time of flight with respect to the length).

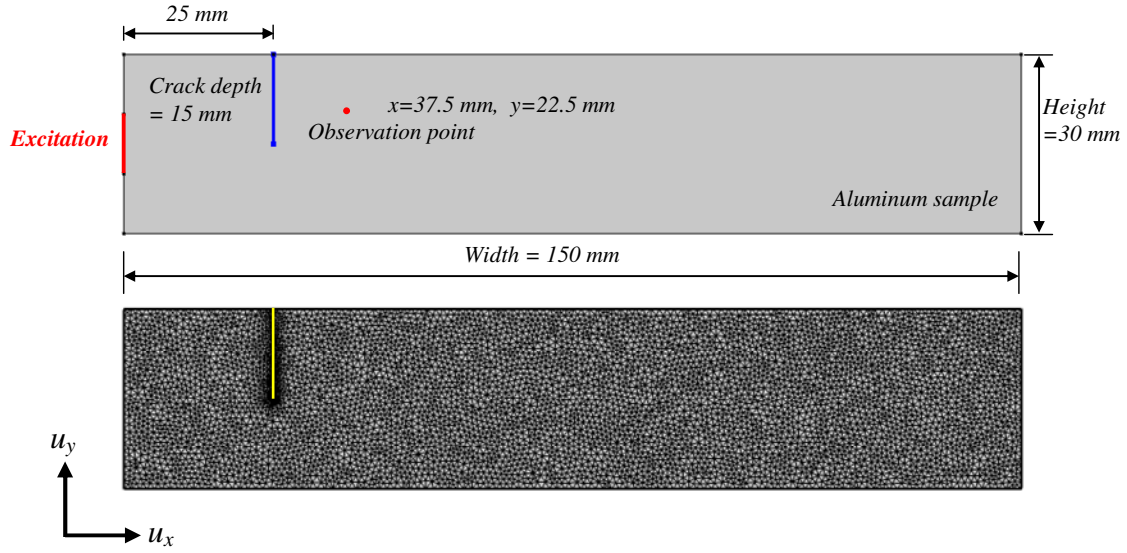

Fig. 10. Illustration of the geometry implemented in COMSOL, together with the generated mesh. The geometry consists of a rectangular aluminum domain with a crack of finite extent positioned vertically at a distance of 25 mm from excitation side of the aluminum domain. The geometry was meshed with triangular mesh elements. Smaller mesh elements were generated in the region of the crack to keep the boundary condition errors at a low level (Fig. 11).

Time and space discretizations are characterized by two point numbers, N_t and N_x. The former one is a number of time steps per excitation period 1/f, while the latter one is the number of mesh elements per smallest spatial element of geometry. In the considered case it is the crack

size; a typical longitudinal wavelength of 80 mm is much longer. To keep boundary condition errors at a low value, mesh around the crack should be refined with some factor. The mesh refinement optimization is done separately and is not discussed here. The illustration in Fig. 11 shows the boundary condition error for N_t=200 and N_x=12. In future, this error will be kept on an approximately the same level considered satisfactory as acoustic nonlinearity itself is usually quite small.

Further, we performed a number of simulations with several values N_t=50, 100, 200, 400 and N_x=12, 19, 27, 35, 43. The convergence level was estimated by calculating normalized rms deviations between the responses at the observation point (see Fig. 10) for a current case and the best case N_t=400, N_x=43. The "responses" in our modeling were the x-component of displacement (u_x) and stresses σ_{xx} and σ_{xy}. The results are given below in Fig. 12.

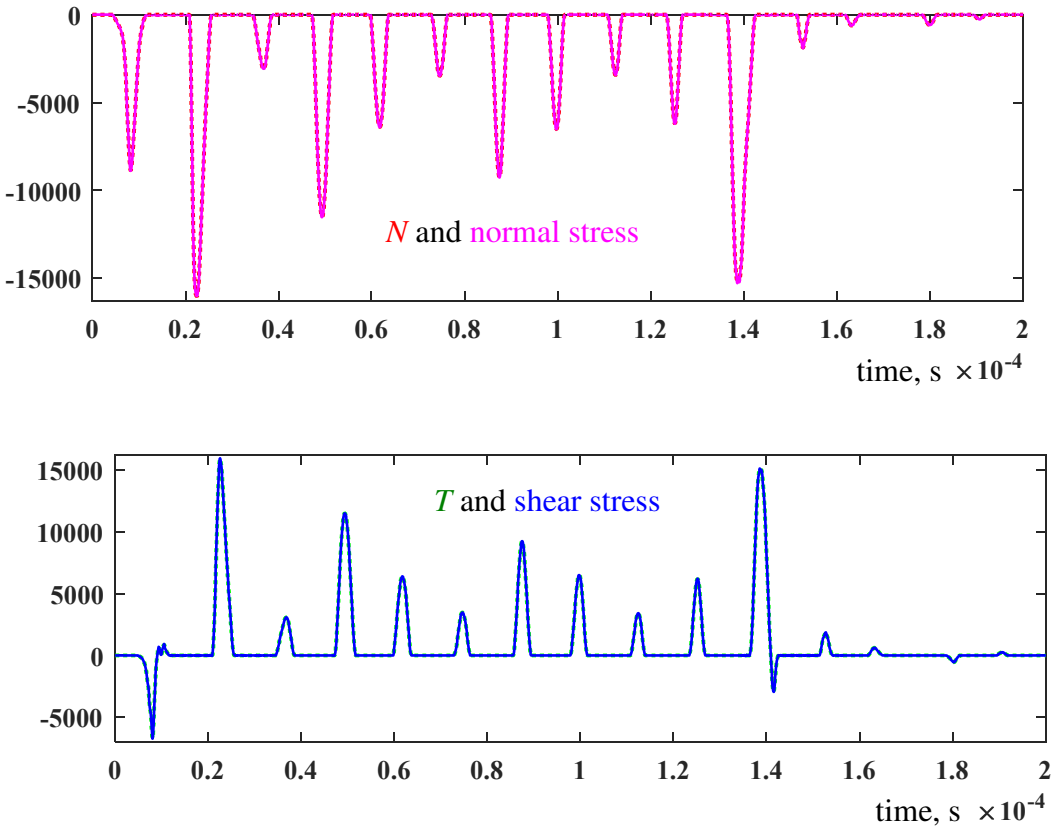

Fig. 11. The boundary condition error: contact loads N and T calculated by the MMD and the respective stress values determined by the FEM solver.

These results show highest N_t, which is reasonable to take for each N_x, and the corresponding precision in terms of displacements and stresses. For instance, the last picture shows that for N_x=27 it is enough to select N_t=100 to get error of 0.5%, and further increase in N_t is useless.

If the desired precision is 0.3%, it is necessary to choose a higher N_x=35 and increase N_t up to 200.

The error in terms of stresses is usually higher than for the displacement. However, it is the normal displacement at the sample's surface, which is measured in laser vibrometry experiment. In this case, for typical nonlinear responses exceeding 1% the precision obtained in our preliminary study is satisfactory. The results shown in Fig. 12 help optimize the code in terms of the space and time discretization. In each case, they indicate maximum N_t such that further time step decrease is useless.

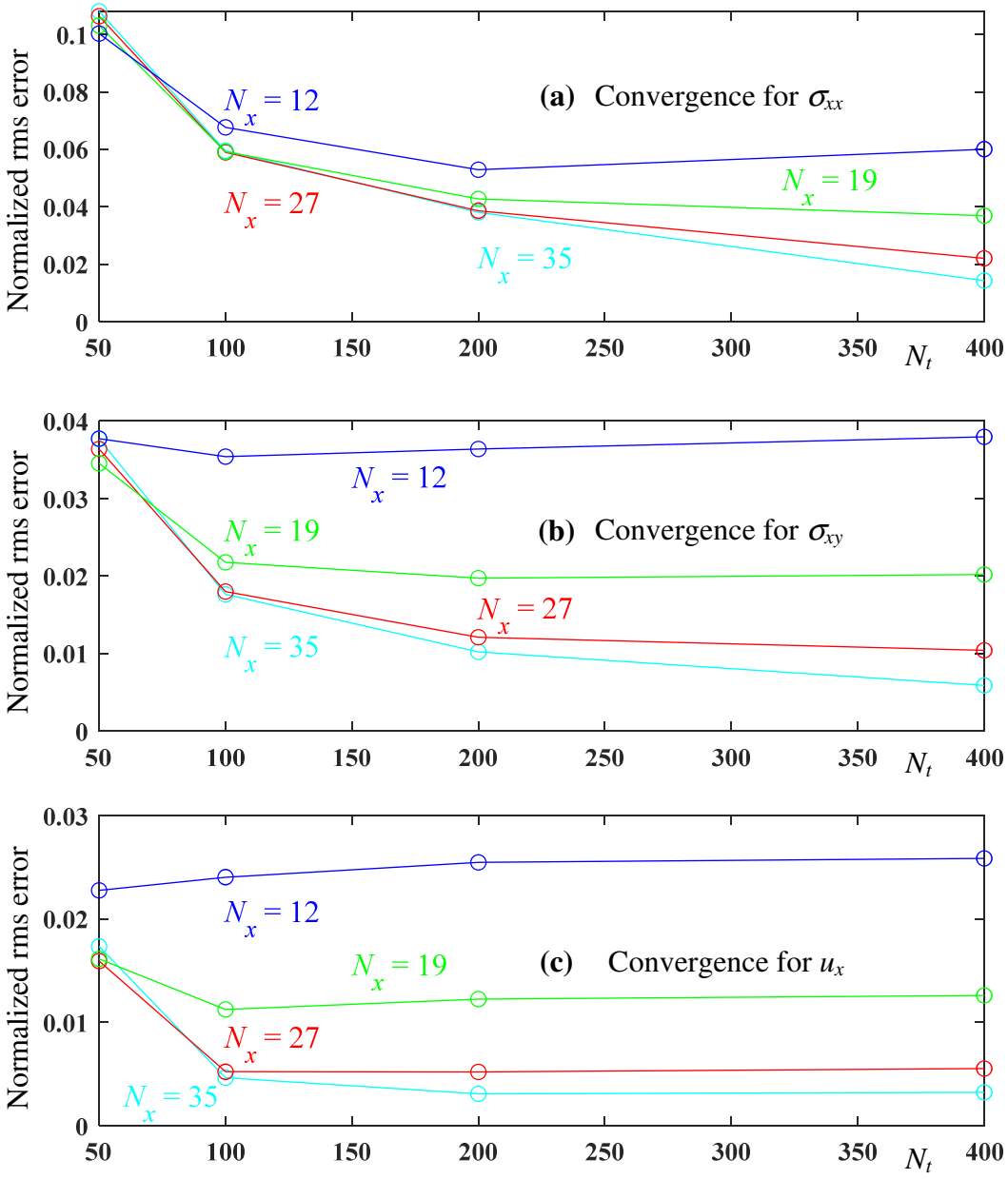

Fig. 12. Values of relative errors for σ_{xx} **(a)**, *σ_{xy}* **(b)**, *and u_x* **(c)** *at the observation point. Curves as functions of N_t are given for several N_x values. The error is calculated by comparison of each current case (N_t, N_x) with the best result for N_t=400 and N_x=43.*

3. Conclusion

In Chapter II we described the MMD-FEM modeling tool in detail. Firstly, it used a semi-analytical solution of the Cattaneo-Mindlin type for contact of isotropically rough surfaces extended to take into account partial slip, total sliding, and contact loss. The Cattaneo-Mindlin approach generalized in the frameworks of the MMD provided calculation of contact loads directly from contact displacements and their histories at each point at the crack interface, with no need to adjust values at neighboring point for the fulfillment of the Coulomb friction law.

Secondly, the MMD-based boundary conditions were integrated into a standard FEM environment (COMSOL) that provided the model for wave propagation in solid materials containing frictional cracks.

We also presented some convergence analysis in one particular case that gave an idea on the degree of time and space discterizations required to achieve a certain final precision in terms of measurable characteristics. With the developed tool in hands, everything is ready for modeling for more or less realistic situations corresponding to the acoustic experiment with surface measurement of nonlinear stationary wave displacements (or velocities).

Chapter III: Modeling for nonlinear acoustic imaging of an isolated crack

In this Chapter, we describe an extensive series of nonlinear computations of an isolated crack in a fragment of a plate considered in an easiest case from the point of numerical modeling. In the 2D geometry, we select boundary conditions disabling non-essential motion types e.g. bending modes. Besides, we assume a relatively large crack and a low aspect ratio for the sample thus not creating tiny geometric features requiring especially dense meshing. A collection of a large number of cases with different geometric and excitation parameters gives one an idea on detectable and non-detectable cracks as well as on the working range of parameters.

1. Geometry and parameters

Setting up 2D geometry and boundary conditions for the nonlinear acoustic problem is stipulated by the following considerations:

- The Geometry should represent a fragment of a realistic structure, e.g. a fragment of a plate with edges having negligible reflections;
- The Material attenuation should be high enough to build up stationary waves during reasonable time;
- The top face should be free to imitate scanning by laser vibrometer;
- Some boundaries should be fixed to avoid movement of a sample as a whole (in laboratory experiments, samples are usually suspended, which is not considered here).

A simple case meeting those requirements is illustrated in Fig. 1. The 15x3 cm^2 sample has free, fixed and low-reflecting boundaries. The crack has a specific length (we consider cracks of various lengths, including 3 cm, 2 cm, 1 cm and 0.5 cm) and is located at a depth of 0.5 cm; mesh refinement around it is necessary for robust code functioning (see Fig. 11 of Chapter II). Further details about mesh refinement in problems related to cracks can be found in **[Ras-98]**, **[Kho-13]**. Fixing the lower boundary for simplicity may limit the excitation of bending modes, which could have implications for the acoustic propagation within the system.

It is important to mention that the numerical problem formulated in that way is related to two difficulties. One of those is unknown composite roughness statistics for the inner contact that makes the coefficient *C* unknown (see Eq. 21-22 in article published by Biwa et al. **[Biw-04]**).

In their literature, a value $C = 6 \cdot 10^{10}\ Pa^{1/2} m^{-1}$ has been reported for two aluminum blocks of unspecified roughness. In reality, inner crack faces have much higher but partly conforming roughness. With no *a priori* information on it we use value $C = 10^{10}\ Pa^{1/2} m^{-1}$ having the same order of the value as a first guess corresponding to higher roughness. Further on, the influence of this important parameter on nonlinear acoustic images will be evaluated.

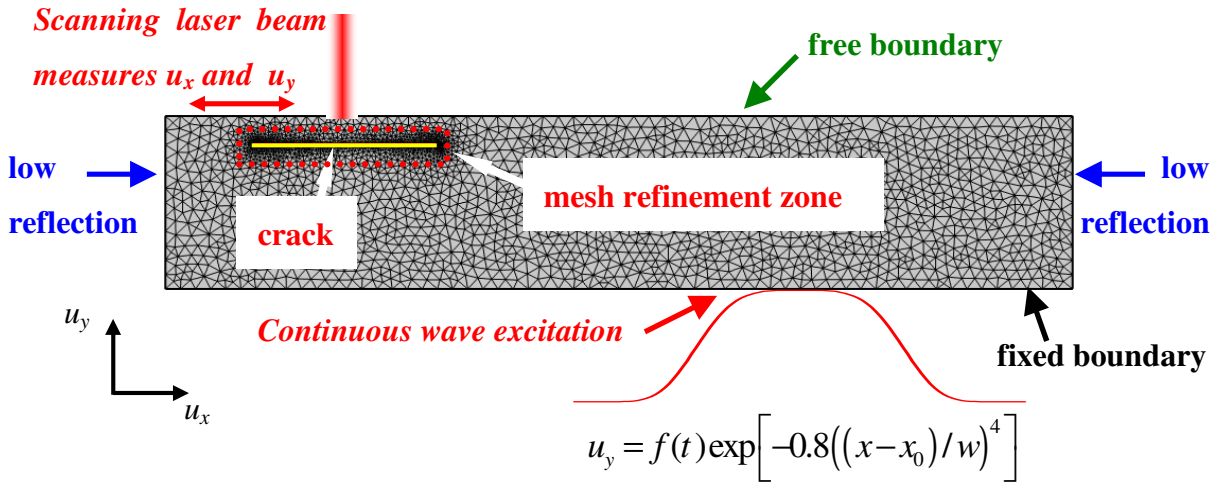

Fig. 1. Meshed sample of 15x3 cm^2 dimensions containing a crack. Free, fixed and low-reflecting boundaries are indicated together with a zone of continuous excitation that has the length 2w and is centered at x_0. The sample is excited by a vertical displacement u_y those time dependence is defined by function f(t), figure source from **[Ale-23]**.

The second difficulty has a more technical character and is associated to the necessity to have highly stable stationary waves, which should be perfectly harmonic in the absence of damage. Indeed, a remaining transient component introduces parasite frequency components (continuous spectrum), which are not related to nonlinear generation by damage, thus corrupting nonlinearity images. In real experiments this effect does not arise as even for low attenuation materials a waiting time of as few seconds is sufficient to make sure that no trace of the transient regime remains. In numerical modeling, such a delay is hardly possible as few real seconds correspond to days of computing on an average PC. Therefore, in our modeling, while having elastic parameters of the material equal to that of aluminum to be consistent with available data **[Tal-79]**, we use highly exaggerated damping (bulk and shear viscosities $\eta_b = 167\ Pa \cdot s$ and $\eta_v = 60\ Pa \cdot s$, respectively). These values satisfy the common relationship $\eta_b / \eta_v = K / G$, with K and G, bulk and shear moduli. Thus, in our first MMD-FEM simulations for stationary waves, the material is assumed to have elastic properties of a metal but damping typical to composite materials with epoxy-based matrix. The influence of attenuation on the transient process decay is estimated in greater detail in Section 2.1. Note

that low-reflecting boundaries play a significant role for evacuating the acoustic energy in the sample, thus effectively shortening the transient period duration.

The term stationary waves are used here since the sample has low-reflecting boundaries and represents a fragment of a plate, otherwise standing waves with non-moving amplitude pattern would be formed. Low-reflecting boundaries are designed to reduce the reflection of waves at the boundary of the computational domain, thereby mimicking the behavior of waves in an unbounded medium. This is achieved by modifying the boundary conditions to allow waves to pass through with minimal reflection. On the other hand, perfectly matched layers are an alternative approach where an absorbent layer is introduced around the computational domain to absorb outgoing waves, effectively preventing reflections from the boundary. Perfectly matched layers are known for their ability to handle wave's incident at any angle and frequency, making them highly effective but computationally more demanding.

It is well recognized that perfectly matched layers generally offers broader applicability than low reflecting boundaries and is often viewed as the superior alternative **[Liv-18]**. However, in our model, we chose low reflecting boundaries due to their simpler design, reduced computational demands, and enhanced performance in comparison to perfectly matched layers **[Muh-21]**.

In what follows, we are focus on two different nonlinear techniques that use single and dual frequency excitation. In the former case, higher harmonics will be generated through the contact acoustic nonlinearity effect. The latter technique used frequency mixing i.e. the appearance of the combination frequencies in the spectrum. Moreover, for the high excitation amplitude selected, process of higher orders will take place when the combination frequencies interact with the fundamental ones. It is important to mention that, in addition to nonlinear interactions, proper nonlinear resonances in the sample are frequently exited which are absent in the absence of damage. Further we analyze these effects in more detail and show a series of simulated nonlinear images based on the selected criterions.

2. Single frequency excitation

The first sequence of results is obtained in a traditional case of a harmonic excitation with $f(t) = A\sin 2\pi ft$ where the amplitude A is chosen equal to $6.6\cdot 10^{-8}$ m that provides strong but realistic value of acoustic strain $\varepsilon_{cra} \sim 10^{-6}$ in vicinity of the crack. The considered value of the strain ε_{cra} actually denotes the rms of the first strain tensor invariant averaged at a number of points near the crack. To ensure the decay of the transient process, the total

observation time was 300 excitation periods 1/*f*. The following damage images are generated on the basis of the harmonics generated by contact nonlinearity.

2.1. Stationary regime identification

Our analysis only concerns the stationary regime that takes place after the transient process is over. In the stationary regime, the wave signal at every point of the intact sample contains the same frequencies as the excitation signal. In the damages sample, new frequencies coming from nonlinear interactions or from nonlinear resonances will appear providing a source for building up images. Therefore, it is essential to correctly identify the stationary regime i.e. properly select the signal's tail in which a residual of the transient process is negligible.

The choice of the tail's duration is determined by two contradictory factors. On one hand, it should be short enough to make sure that the transient process decayed. On the other hand, it should be long enough to represent a richer harmonic content. The latter factor is especially important when nonlinear resonances appear at frequencies which are not multiples of the fundamental ones thus breaking periodicity of the spectrum. This effect should not interfere with the stationary character of the concluding tail, therefore it makes sense to determine the stationary regime for the intact sample when those resonances are absent.

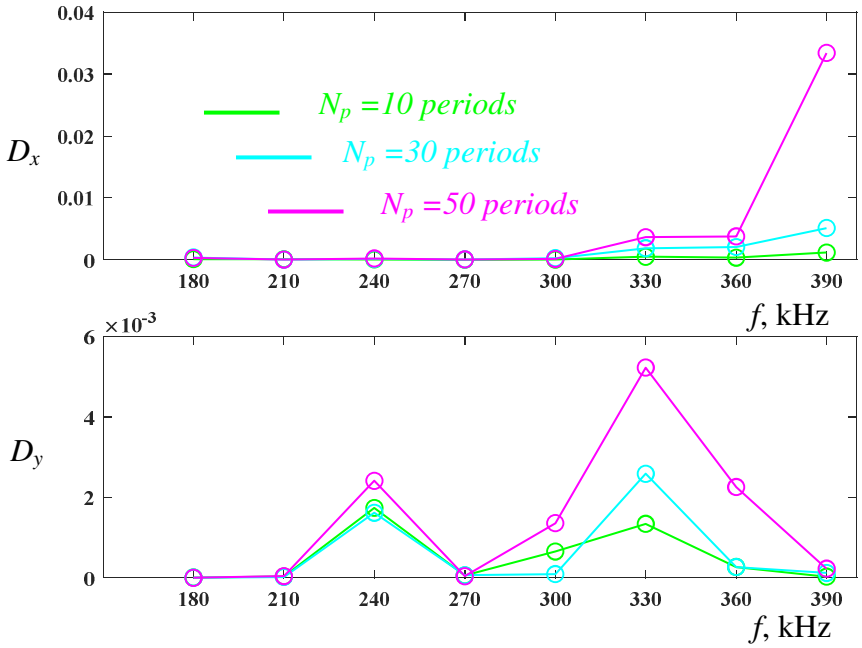

Fig. 2. Comparing deviations $D_{x,y}$ between the first and last fragment of the stationary tail calculated for different tail durations measured in the numbers N_p of quasi-periods, for excitation frequencies f ranging from 180 kHz to 390 kHz in an intact sample.

For signal's tail containing the number N_p of quasi-periods in the considered tail, we define a deviation between the first $u_{x,y}^{first}(x,t)$ and last $u_{x,y}^{last}(x,t)$ quasi-periods of the tail as

$$D_{x,y} = \frac{\sum_{i=1}^{N_t} \left(u_{x,y}^{first}(C_{cr}, t_i) - u_{x,y}^{last}(C_{cr}, t_i) \right)^2}{\sum_{i=1}^{N_t} \left(u_{x,y}^{last}(C_{cr}, t_i) \right)^2}, \quad (1)$$

where N_t is the number of time points per quasi-period, and the wave displacements are calculated at the top surface of the sample at the point corresponding to the crack center, C_{cr}.

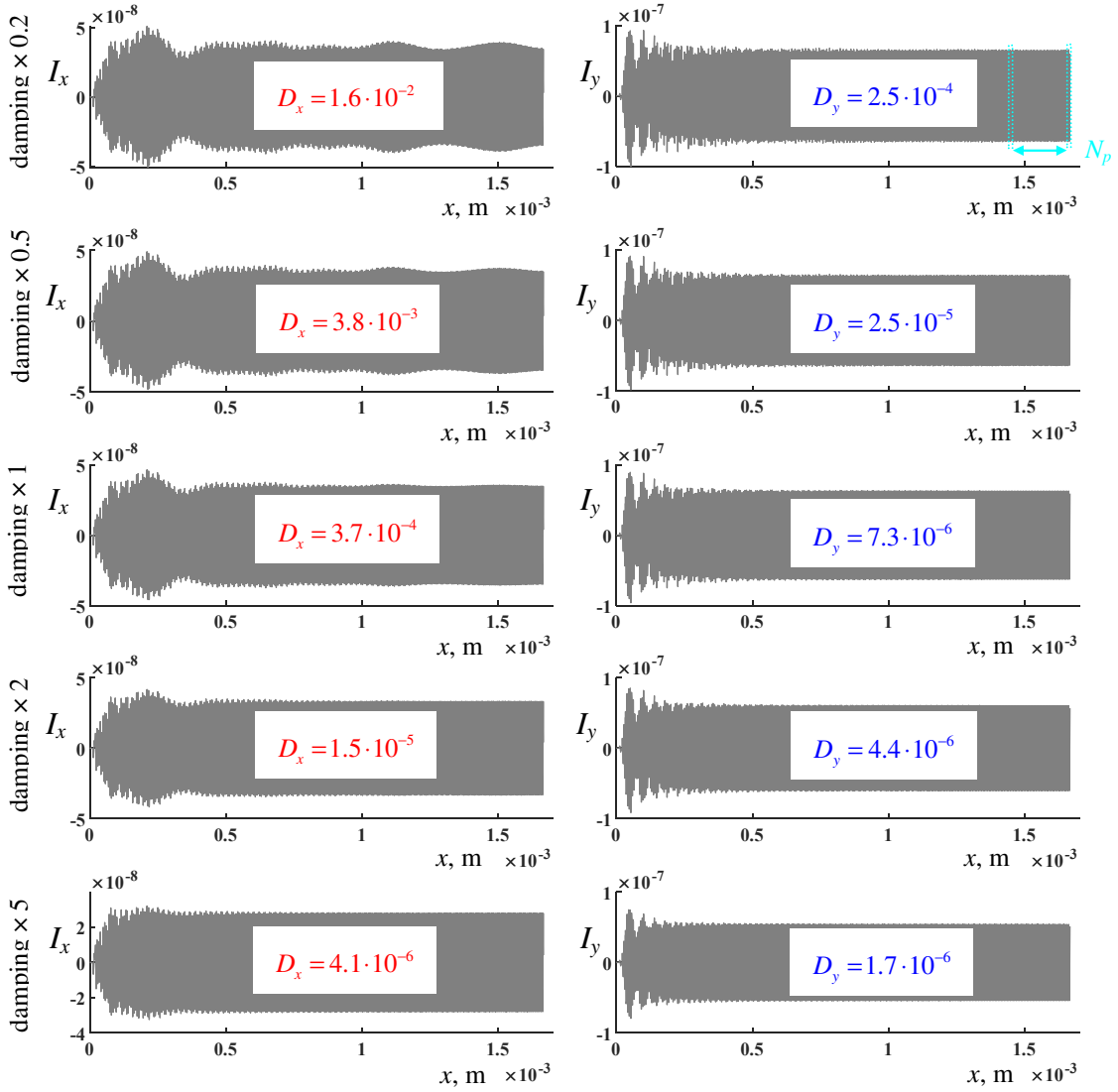

Fig. 3. Effect of damping on stationary wave formation in an intact sample at f=180 kHz. The original damping coefficients $\eta_b = 167\ Pa \cdot s$, $\eta_v = 60\ Pa \cdot s$ *are multiplied by a factor of 0.2, 0.5, 1, 2, and 5. The deviations are calculated for specified tail duration* $N_p = 30$ *according to Eq. (1) and gradually decrease as long as this factor grows. The first and last fragments are illustrated in the upper right plot.*

In Fig. 2, the deviations $D_{x,y}$ are plotted for different numbers N_p of quasi-periods in the tail, as a function of excitation frequency *f*. As one can see, taking N_p=30 is enough to guarantee a

reasonably low deviation $D_{x,y}$ and, at the same time, have a sufficient number of points to represent spectral features.

Note that the illustration Fig. 2 is made for the exaggerated bulk and shear viscosities values that equal $\eta_b = 167\, Pa \cdot s$ and $\eta_v = 60\, Pa \cdot s$, respectively. It would be of interest to see the effect of material attenuation on the stationarity of the tail in terms of deviations $D_{x,y}$ and to specify a reasonable range of damping coefficients suitable for the practical use of the MMD-FEM model implemented here. Due to limited computational resources, it is preferable to use relatively high damping that shortens the stationary wave formation time.

In the presented example of an intact sample excited at *f*=180 kHz, the original damping coefficients $\eta_b = 167\, Pa \cdot s$, $\eta_v = 60\, Pa \cdot s$ are multiplied by factors of 0.2, 0.5, 1, 2, and 5. Fig. 3 shows the degree of stationarity that can be obtained for different attenuation levels. It is important to make sure that the deviations $D_{x,y}$ are less than the nonlinear criterions used as images, otherwise the image robustness can not be guaranteed. In the next section we shall see how these criterions are defined.

2.2. Signal processing

The synthetic data for obtaining damage images represent the time-dependent horizontal u_x and vertical u_y wave displacement components calculated at a number of *x*-points (here 1000) located at the top surface of the sample (similarly to Fig. 3 but for a damaged sample). At each scanned *x*-point we apply the Fourier transform to the stationary solution i.e. the identified concluding signal's tail containing N_p quasi-periods each having the duration 1/*f*. Then the excitation frequency *f* will have number N_p in the Fourier spectrum.

As described in **[Ale-23]**, we introduce the nonlinear criterion (called here image) as

$$I_{x,y} = \sum_n \left(\frac{A^n_{x,y}}{A^1_{x,y}} \right)^2 , \tag{2}$$

where $A^n_{x,y}$ is the *n*-th harmonic amplitude shown in Fig. 4(a) and Fig. 5(a). In Eq. (2) the harmonics are numbered relatively the fundamental one with frequency *f*, but their actual numbers in the spectrum are $n\, N_p$ since it actually constants N_p fragments.

I_x and I_y images are shown in Fig. 4(b) and in Fig. 5(b), respectively. The full u_x and u_y records at the crack center C_{cr} are plotted in sets (c) in both figures, while the first and last fragments of the stationary tail are shown in sets (d).

The definition Eq. (2) has the same metrics as Eq. (1) and also coincides with the criterion used in known laser vibrometry experiments (chapter 4 of **[Jha-20]**) that provide typical values of order of 10^{-3} for moderate damage level. The only important feature is that the first harmonic in the denominator of Eq. (2) is actually a complex stationary wave with nodes of almost zero amplitude. In this situation, images $I_{x,y}$ have maxima at the positions of zeroes of $A^1_{x,y}$ regardless of damage-related higher harmonics in the numerator. At the same time, normalization in Eq. (2) is essential as zones with lower acoustic intensity in the sample should not be penalized. To deal with the issue, we applied running averaging to $A^1_{x,y}$ as a function of *x*-coordinate on the top surface, with the result shown in Fig. 4(e) and in Fig. 5(e). After application of this simple procedure, it is indeed possible to use the criterion Eq. (2) as an image of damage.

An essential feature of the obtained spectra is the presence of a significant zero harmonic $A^0_{x,y}$. The effect is more pronounced for A^0_y that can be explained by the strong asymmetry in the normal response curve Eq. (30) of Chapter II for positive and negative contact displacements *a*. In other words, the system "prefers" the open state with $a<0$ since in this case there is no contact interaction and the associated strain energy stored in asperities is zero. Roughly speaking, the sample globally thickens near crack under the action of the acoustic excitation that results in appearance of A^0_y. Further, the zero harmonic in u_y engenders the zero harmonic in u_x through Poisson's effect and coupling via boundary conditions.

As we have mentioned, image robustness require the fulfillment of the strong inequality

$$D_{x,y} \ll I_{x,y}. \tag{3}$$

In addition, image "quality" or robustness can be characterized by its contrast defined (refer to **[Ale-23]**) as the nonlinear criterion averaged for *x*-values inside the crack divided by an average outside of it:

$$C_{x,y} = \frac{\left\langle I_{x,y} \right\rangle\Big|_{x\in(C_{cr}-L_{cr}/2,C_{cr}+L_{cr}/2)}}{\left\langle I_{x,y} \right\rangle\Big|_{x\notin(C_{cr}-L_{cr}/2,C_{cr}+L_{cr}/2)}}. \tag{4}$$

Here C_{cr} is the crack center coordinate and L_{cr} is the crack length.

Figures 4 and 5 illustrate signal processing leading from $u_{x,y}$ records to images. At the same time, one important feature appears in Fig. 5, namely a proper nonlinear resonance of the sample marked with green circle. In the next section, these resonances are shown in more detail.

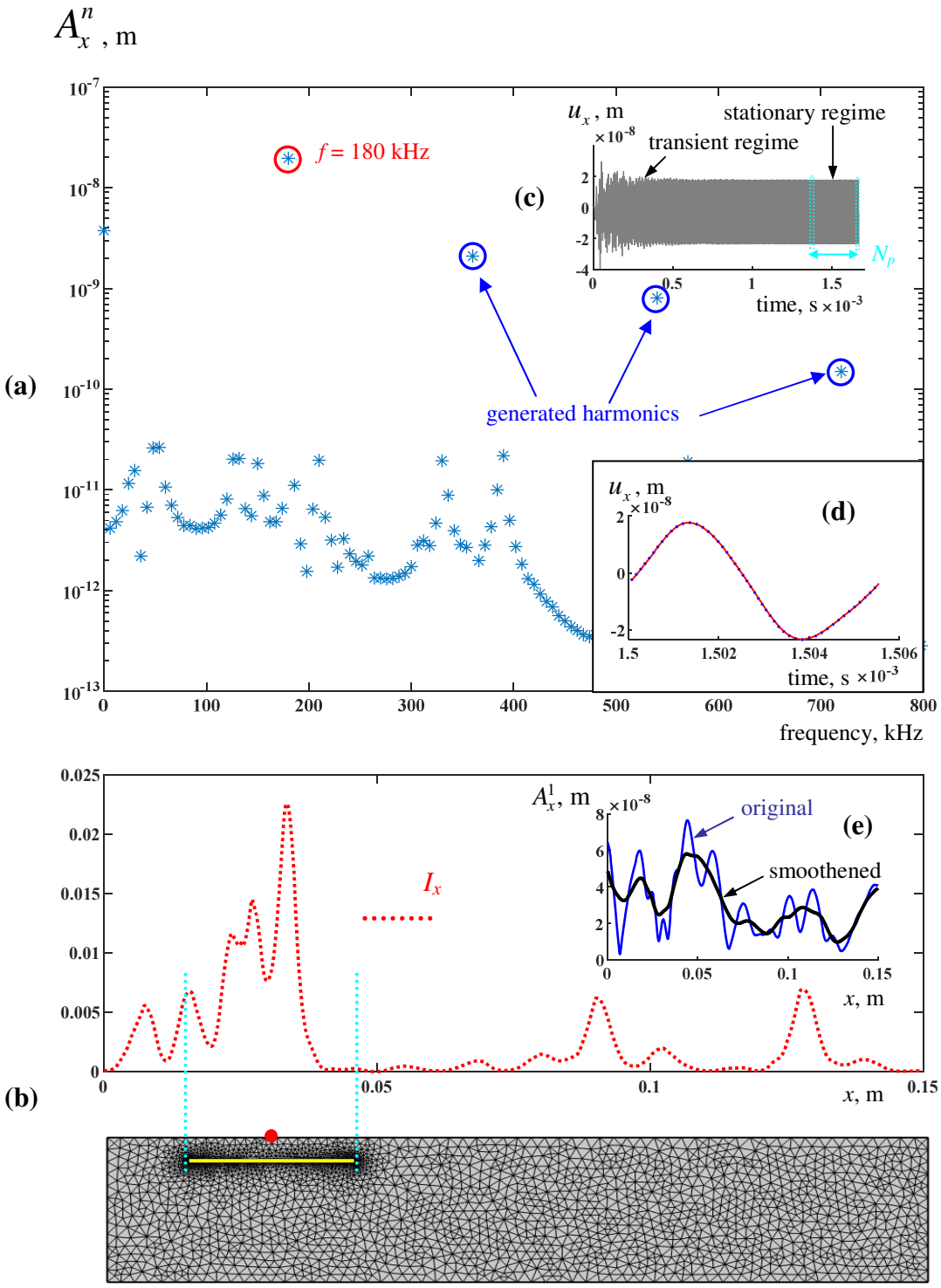

Fig. 4. For the crack of 3 cm length buried at depth of 5 mm : **(a)** *spectrum* A_x^n *of displacement* u_y *on the top surface at the crack center (*x=C_{cr}*, red dot in* **(b)***), with the excited frequency* f *marked with a red circle, and generated harmonics via nonlinear process marked with blue circles;* **(b)** *image* I_x *calculated accordingly to Eq. (2) and the meshed sample with the crack indicated;* **(c)** *full record of* u_x *as a function of time at the crack center,* **(d)** *first and quasi-periods of the stationary tail;* **(e)** *fundamental harmonic in the above spectrum on the entire top surface (original and smoothened via running average).*

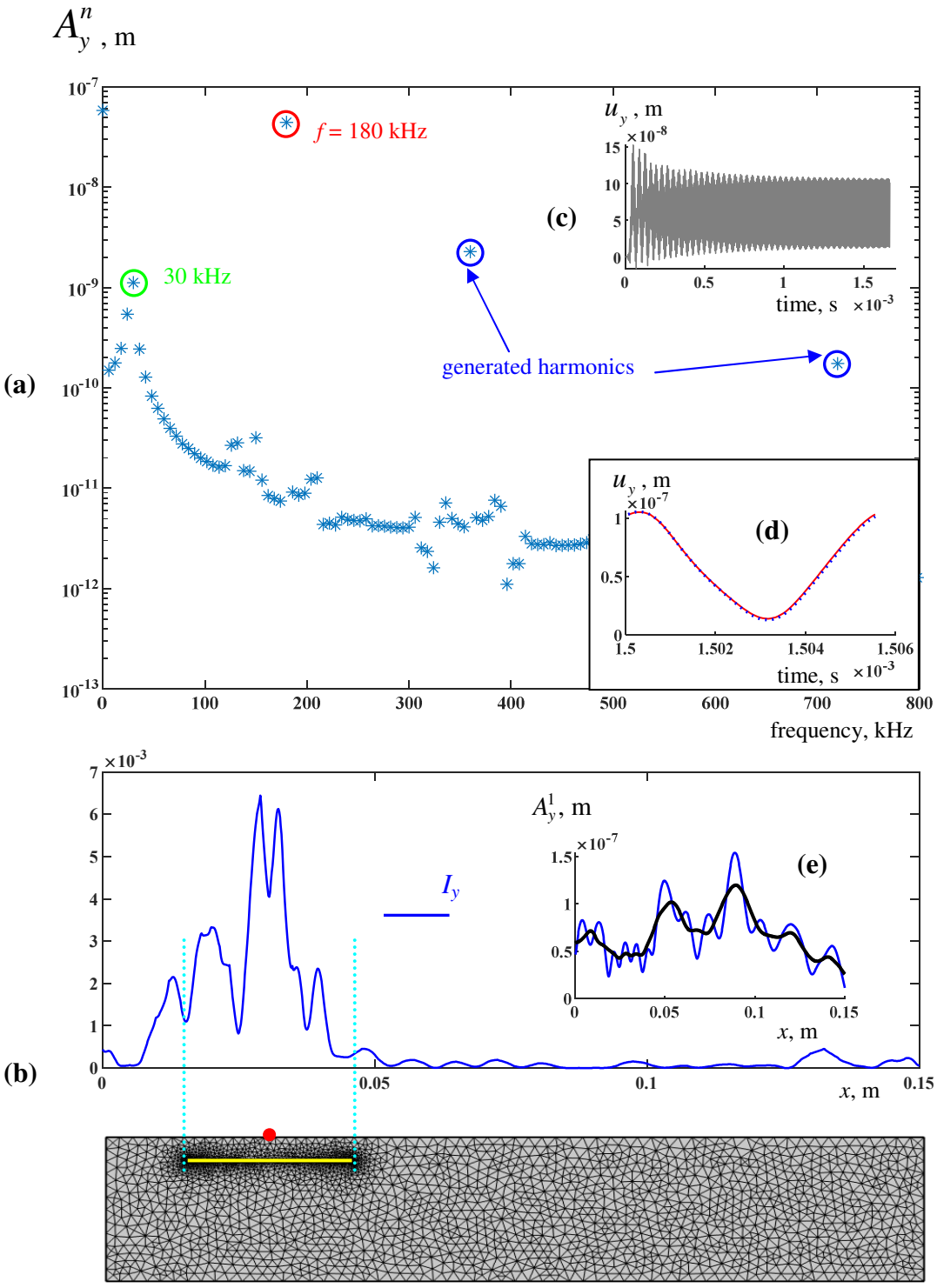

Fig. 5. Same as Fig. 4 but for u_y. Here a proper nonlinear resonance at 30 kHz appears in the spectrum (green circle).

2.3. Proper nonlinear resonances of the sample

In addition to higher harmonics, spectra on the displacement wave components for the damaged sample have another feature that consists in appearance of resonance frequencies showing up as maxima of the spectrum (see Figs. 6-8 (a) and (c)). It is essential that they do not exist in the intact sample and can occur only when damage is present. Therefore their appearance should be related to the crack. Crack is a nonlinear object since it engenders contact interactions strongly nonlinear in nature. In that sense, we call them proper nonlinear resonances of damaged sample. The phenomenon closely resembles that reported in **[Sol-04]**, where the proper resonant frequencies of the sample were identified as the cause behind the generation of subharmonics. Their origin is also close to the one of Local Defect Resonances (LDR) described in more detail in **[Sol-20]** and in other relevant literature like **[Seg-20]**.

The presence of nonlinear resonances can break the periodicity of the response. Whereas for weak resonances with the amplitudes less than the ones of higher harmonics (Fig. 6), their effect is also weak (fully superposing first and last fragment in Fig. 6 (b) and (d)), it starts to be visible in Fig. 7 (b) and (d) in which a small deviation becomes visible. Strong resonances (Fig. 8) completely break the periodicity. The effect occurs since in the considered cases the proper resonances have frequencies different from the fundamental one (f) and its multiples. This is the reason of the use of signal tails longer than just one period; for the completely periodic signals it would enough to consider the last periodic fragment only.

It is important to mention that the criterion Eq. (2) does not take into account the possible nonlinear resonances; a more traditional form corresponding to the known results (chapter 4 of **[Jha-20]**) is preferred.

In section 3.2 the nonlinear resonances are considered in a more specific way; it is suggested to use then for a potential selective detection of crack sizes and lengths.

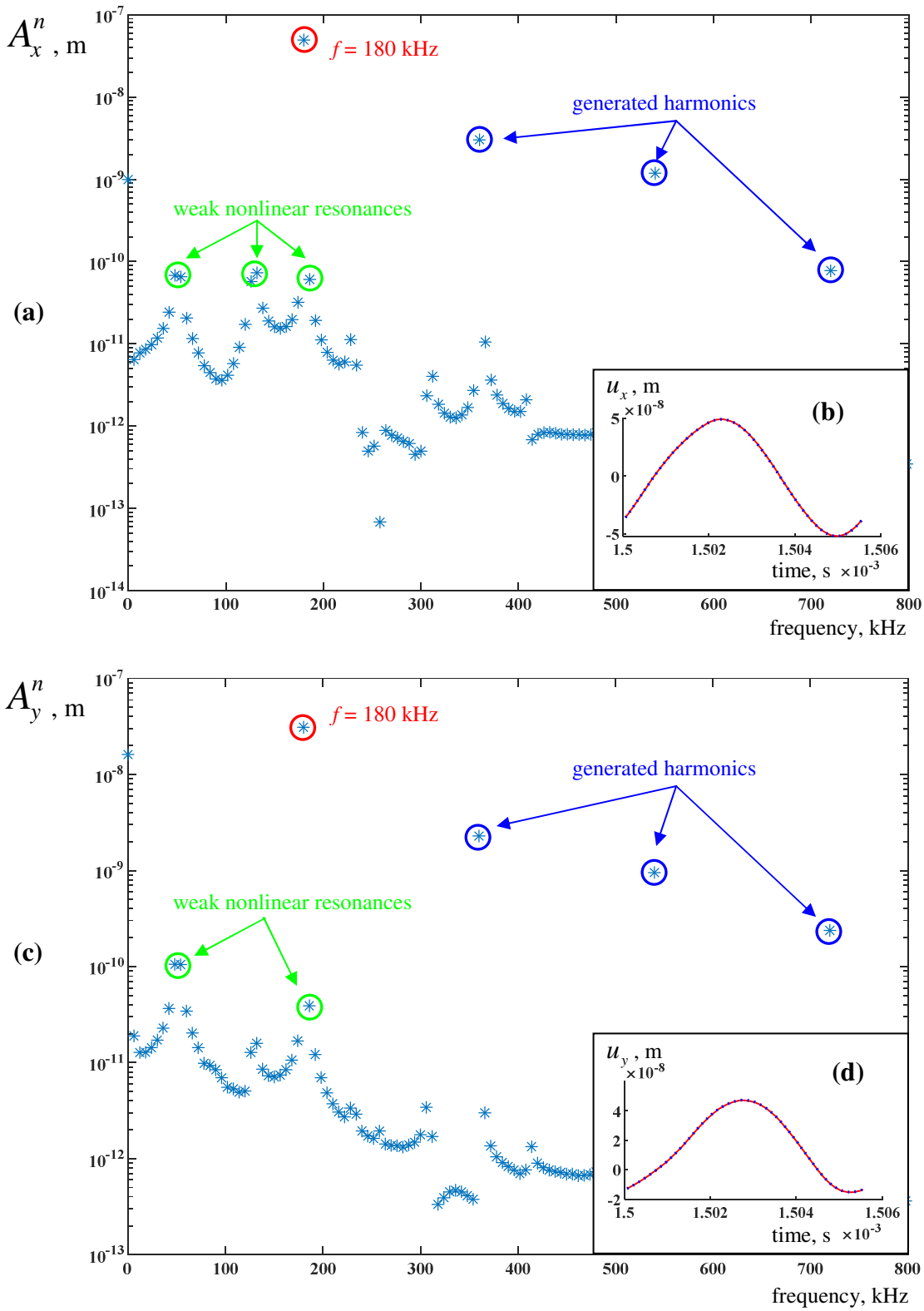

Fig. 6. For the crack of 1 cm length buried at depth of 5 mm : **(a, c)** *spectra* $A_{x,y}^n$ *of displacement* $u_{x,y}$ *on the top surface at the crack center, with the excited frequency* f *=180 kHz marked with red circles, and generated harmonics via nonlinear process marked with blue circles, and with proper nonlinear resonances of the sample marked with green circles;* **(b, d)** *first and last quasi-periods of the signal's tail.*

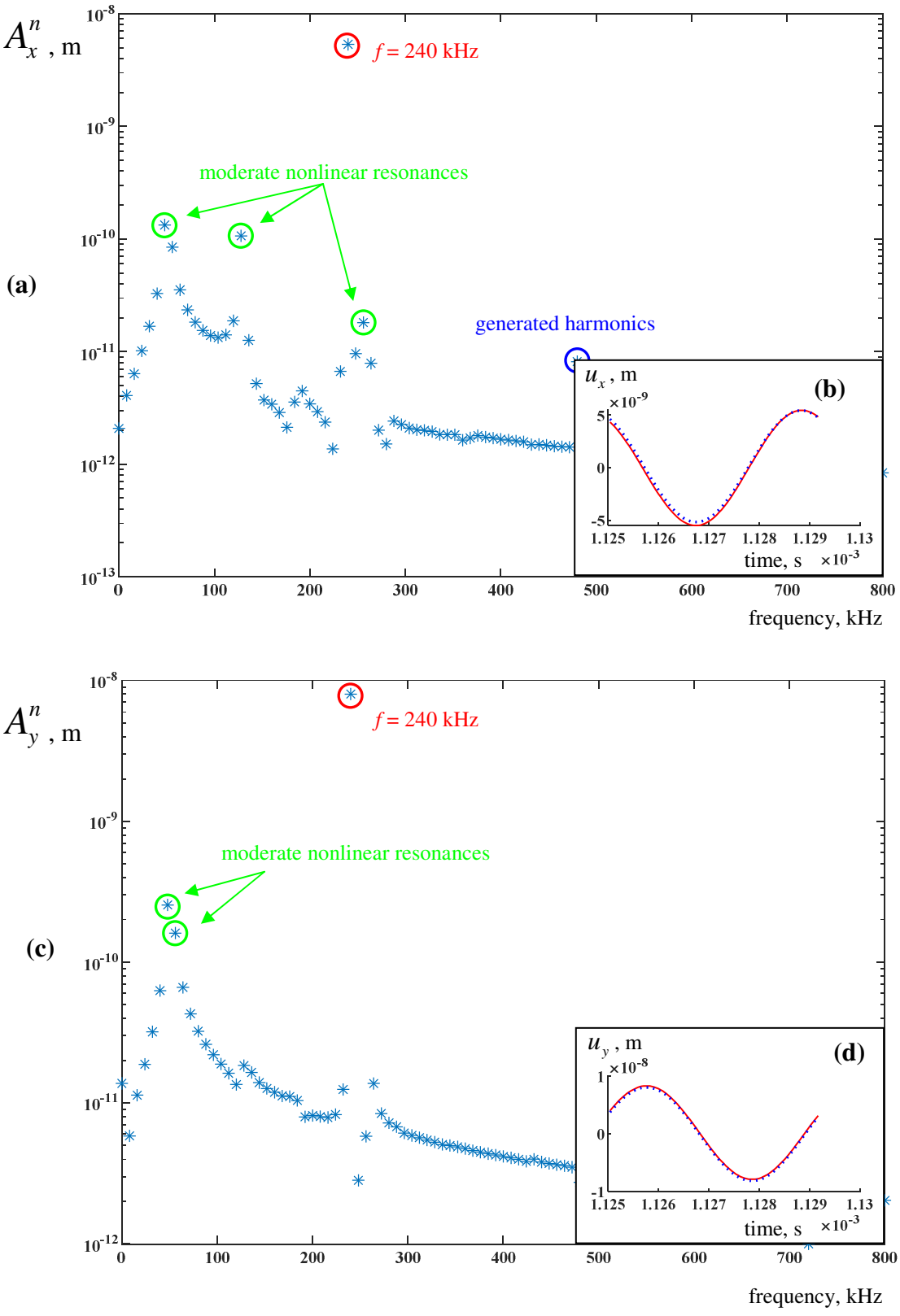

Fig. 7. Similar to Fig. 6 but at excitation frequency 240 kHz.

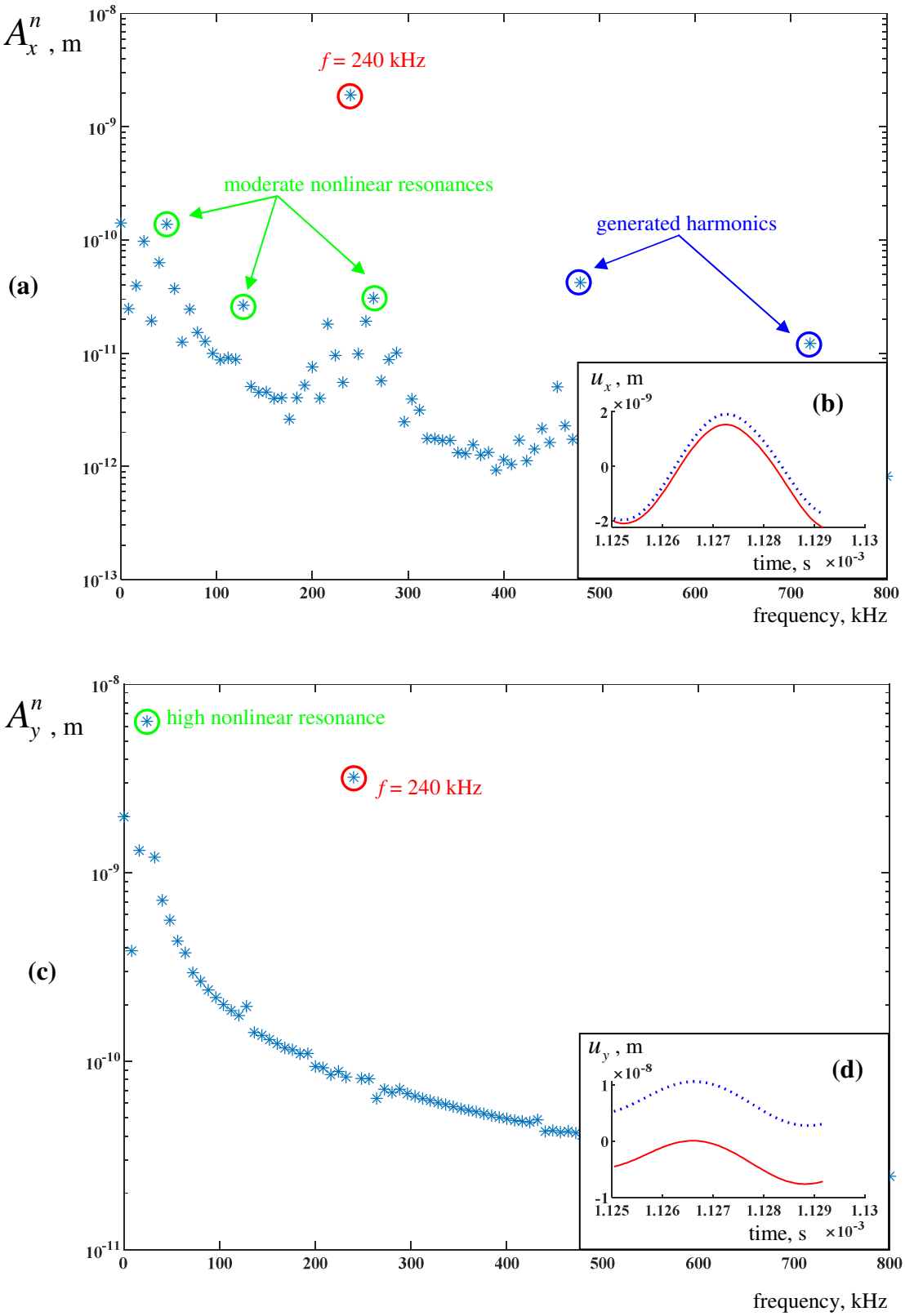

Fig. 8. Similar to Fig. 6 but for a larger crack length (3 cm) excited at frequency 240 kHz.

2.4. Simulated nonlinearity images for various frequencies and damage parameters

2.4.1. Convergence of numerical procedure at the level of nonlinear characteristics

Before presenting a series of images for different parameters, it is important to check the modeling procedure for convergence. This was already done at the level of displacement and stress responses (Chapter II, Section 2.2). Here we want to make sure that the space and time discretization is sufficient for convergence in terms of nonlinear images $I_{x,y}$. To quantify the impact of additional decrease in the spatial element size, we have computed two damage images with the same time step and with mesh element size first original and then reduced with the factor of 1.5. The result is presented in Fig. 9 in which two solid lines almost coincide with two dotted curves indicating original and refined images, respectively. The insignificant difference between these curves characterizes the precision of the numerical method related to finite discretization. In Fig. 9, two examples are presented for various frequencies and crack sizes.

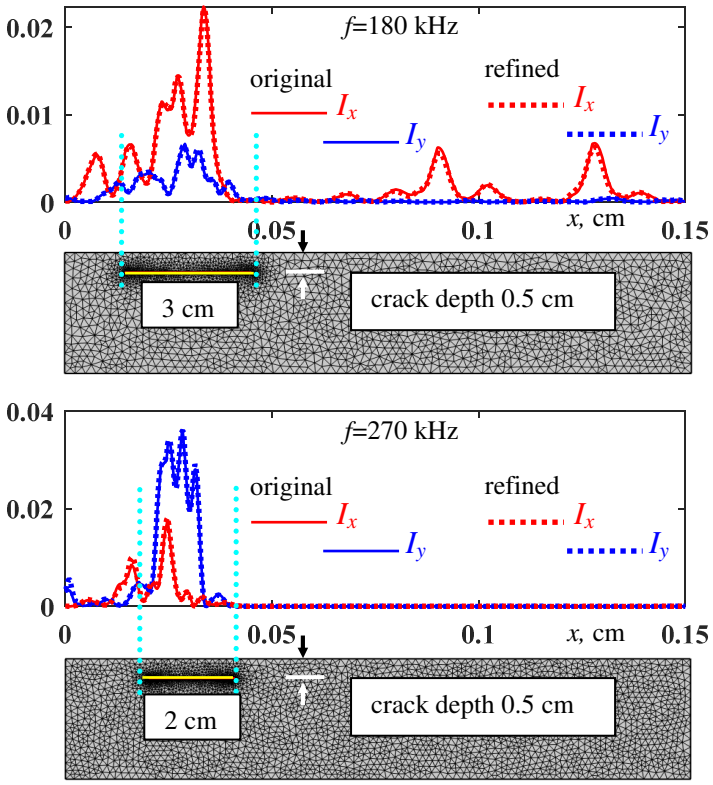

Fig. 9. Demonstration of convergence of the numerical method: solid curves for original images and dotted lines for images obtained on mesh globally refined with a factor of 1.5 coincide with a reasonable precision. Two examples are given for various frequencies and crack sizes, figure taken from **[Ale-23]**.

2.4.2. Crack images for various frequencies and crack sizes

In Figs. 10-17 we present a series of nonlinear images i.e. curves $I_{x,y}$ as functions of *x*-coordinate at the top surface for samples with given material properties (Young's modulus $E = 7 \cdot 10^{10}\, Pa$, Poisson's ratio ν = 0.33, density of 2700 kg/m^3, bulk and shear viscous damping $\eta_b = 167\, Pa \cdot s$, $\eta_v = 60\, Pa \cdot s$, roughness-related coefficient $C = 10^{10}\, Pa^{1/2} m^{-1}$), and for various crack lengths L_{cr} and frequencies *f*. All cracks are centered at the same value C_{cr}=3 cm.

The *x*-coordinates corresponding to the crack are marked in Figs. 10-17 with two dashed vertical lines. The contrast is the principal characteristics related to imaging procedure:

- High values of $C_{x,y}$ indicate correct reconstruction of damage position and extent with weak or absent parasite peaks in the intact zone (see, for instance, images of 3 cm and 2 cm cracks at *f*=300 kHz in Figs. 11 and 13).
- Moderate $C_{x,y}$ levels refer to a more ambiguous situation. For instance, there can be two or more peaks, one correct and the other ones parasite i.e. located at false position, etc. The correct peak can provide moderate $C_{x,y}$, but the presence of the false one generally indicates poor success of imaging (see e.g. Fig. 12, 2 cm crack at *f*=210 kHz, dotted curve).
- Contrasts of about 1 or less signify failure of the imaging procedure (for instance, in Fig. 16, 0.5 cm crack at *f*=240 kHz,).

Results shown in Figs. 10-17 indicate that the detection success (C_x or C_y reaching values of 10^1, 10^2 or more) strongly depends on both frequency and crack size. The dependence on the crack size is obvious; larger cracks generally produce images of higher contrast and are therefore easily detectable. As for the frequency dependence additionally illustrated in Fig.18, it is less evident since at each frequency a nontrivial pattern of stationary waves for each harmonics is formed. There are preferable frequencies such as 300 kHz in our examples at which imaging is successful for any crack sizes considered. At very low frequencies detection is generally worse since the wavelength becomes comparable to the crack size thus poorly activating relative movement of crack faces. Indeed, at 180 kHz the longitudinal and transverse wavelengths equal 3.4 cm and 1.7 cm, respectively. Very high frequencies are also less suitable for imaging as most of acoustic energy is located near the source in that case. Therefore higher excitation amplitudes are needed to maintain a relevant strain $\varepsilon_{cra} \sim 10^{-6}$ at the crack. The frequency range shown in Fig. 18 is selected in accordance to the above limitations. It should also be mentioned that the selection of several frequencies does not

reveal the entire frequency dependence. Restrained computational recourses allowed us to perform computations only for several exemplar frequencies belonging to the range that is most promising for detection. Technically, the calculation time comprising 300 periods corresponds to a COMSOL file size of the order of 30 Gb. The use of frequency sweep to determine optimal excitation frequencies in accordance to the LDR methodology would require even larger calculation time; the COMSOL file will be hard to process in that case.

In Figs 10-17 it can be seen that the nonlinear wave pattern defined in the sense of Eq. (2) generally has a non-trivial structure. In some cases, nonlinear quantity $I_{x,y}$ is concentrated near the crack, whereas in other situations it can be more smeared. The 2D pattern calculated at the top surface can contain additional (parasite) peaks that mask real crack location. However, they reflect physical reality and not result from calculation artifacts. In real experiments images showing parasite peaks are often attributed to imperfect experimental conditions and are disregarded.

Anyway, it seems obvious that, in order to have high-contrast detection, the crack can be efficiently activated and, moreover, the nonlinear wave pattern at that particular frequency should be concentrated near crack and not smeared.

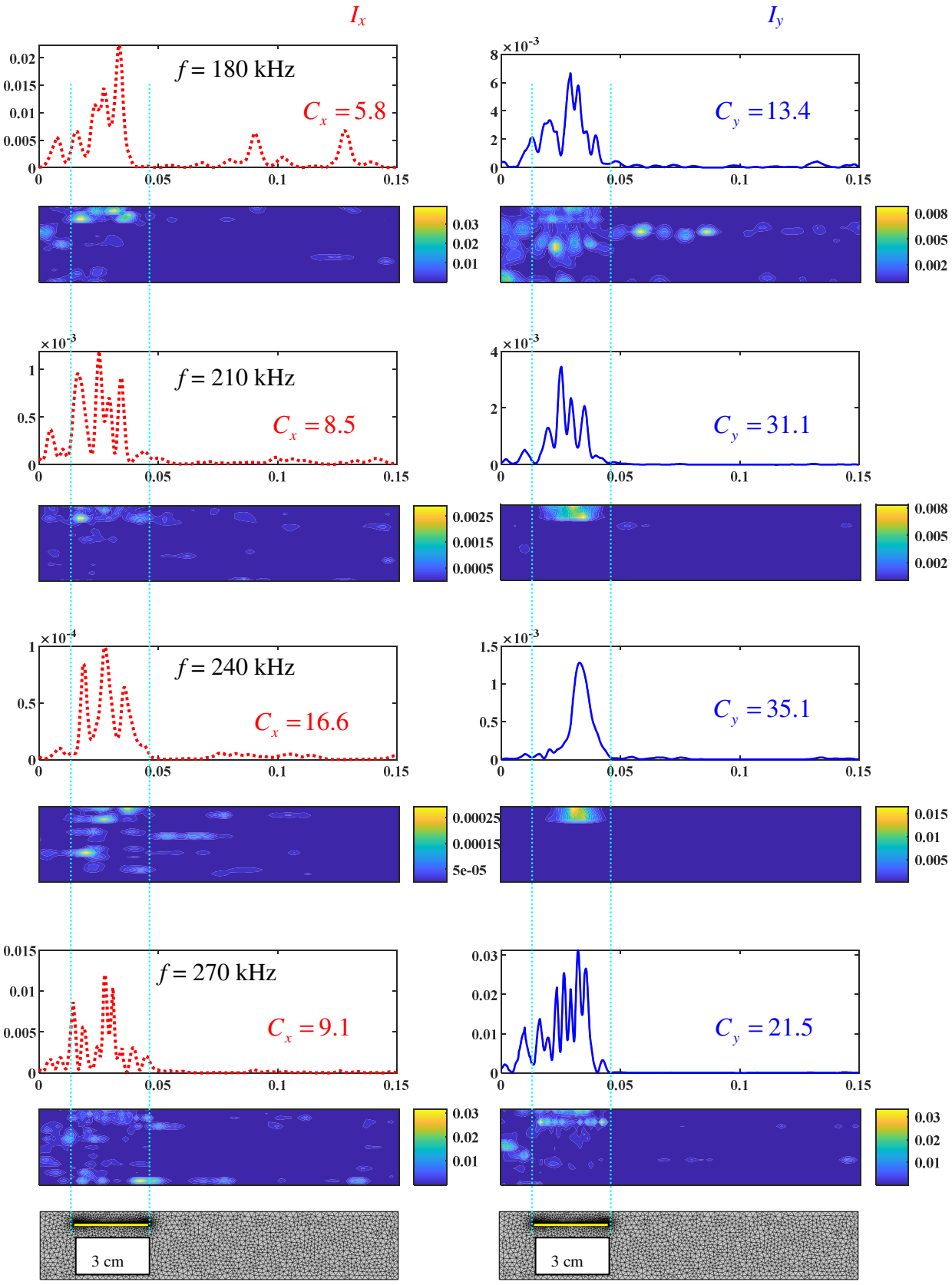

Fig. 10. Nonlinear images $I_{x,y}$ of damage calculated at the top surface (at the top of each series) and in the entire sample (in the middle); meshed sample is shown at the bottom. Here excitation frequency f ranges from 180 to 270 kHz, and crack depth is 0.5 cm.

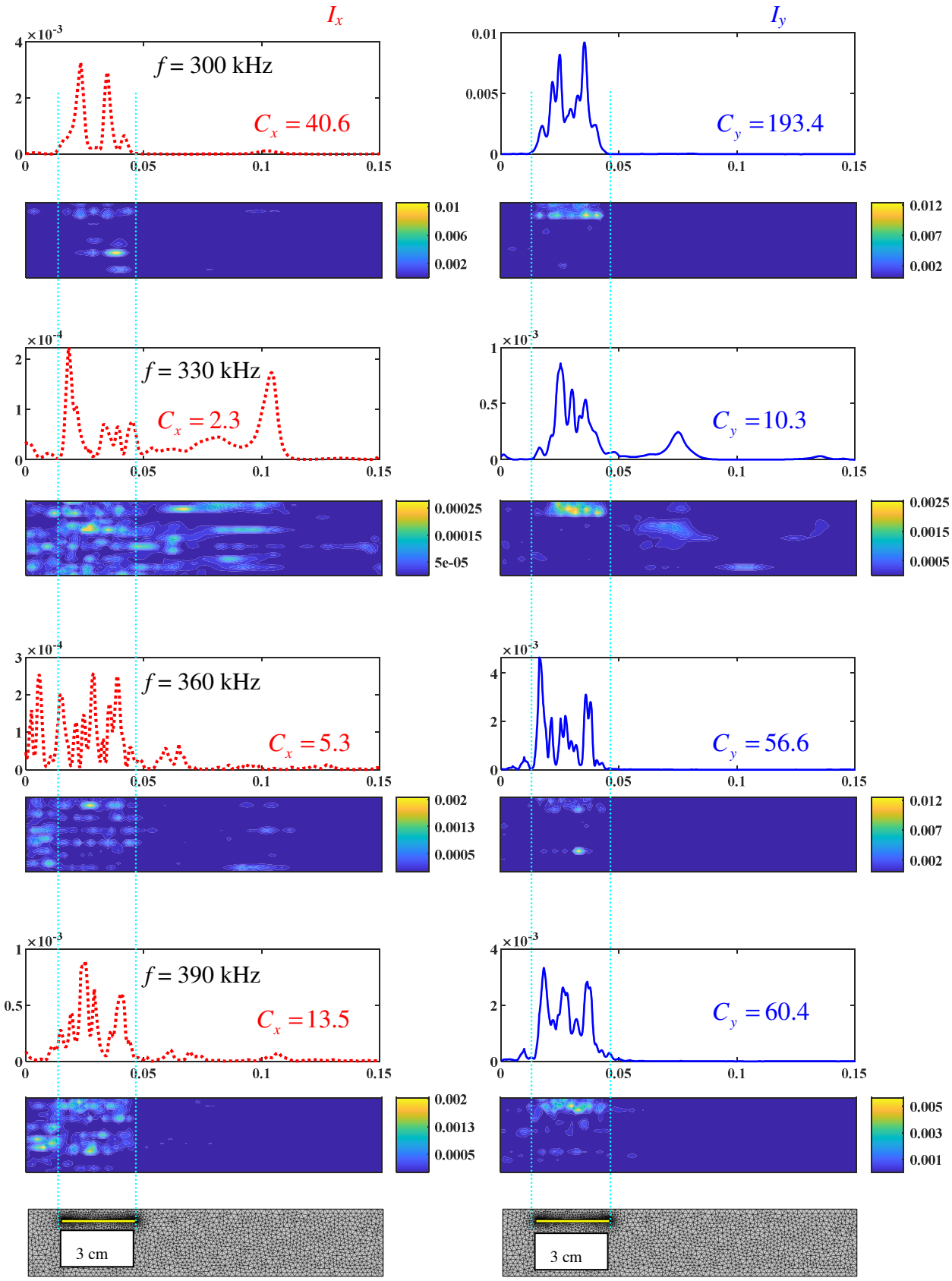

Fig. 11. Similar to Fig. 10 but for the excitation frequency f ranging from 300 to 390 kHz.

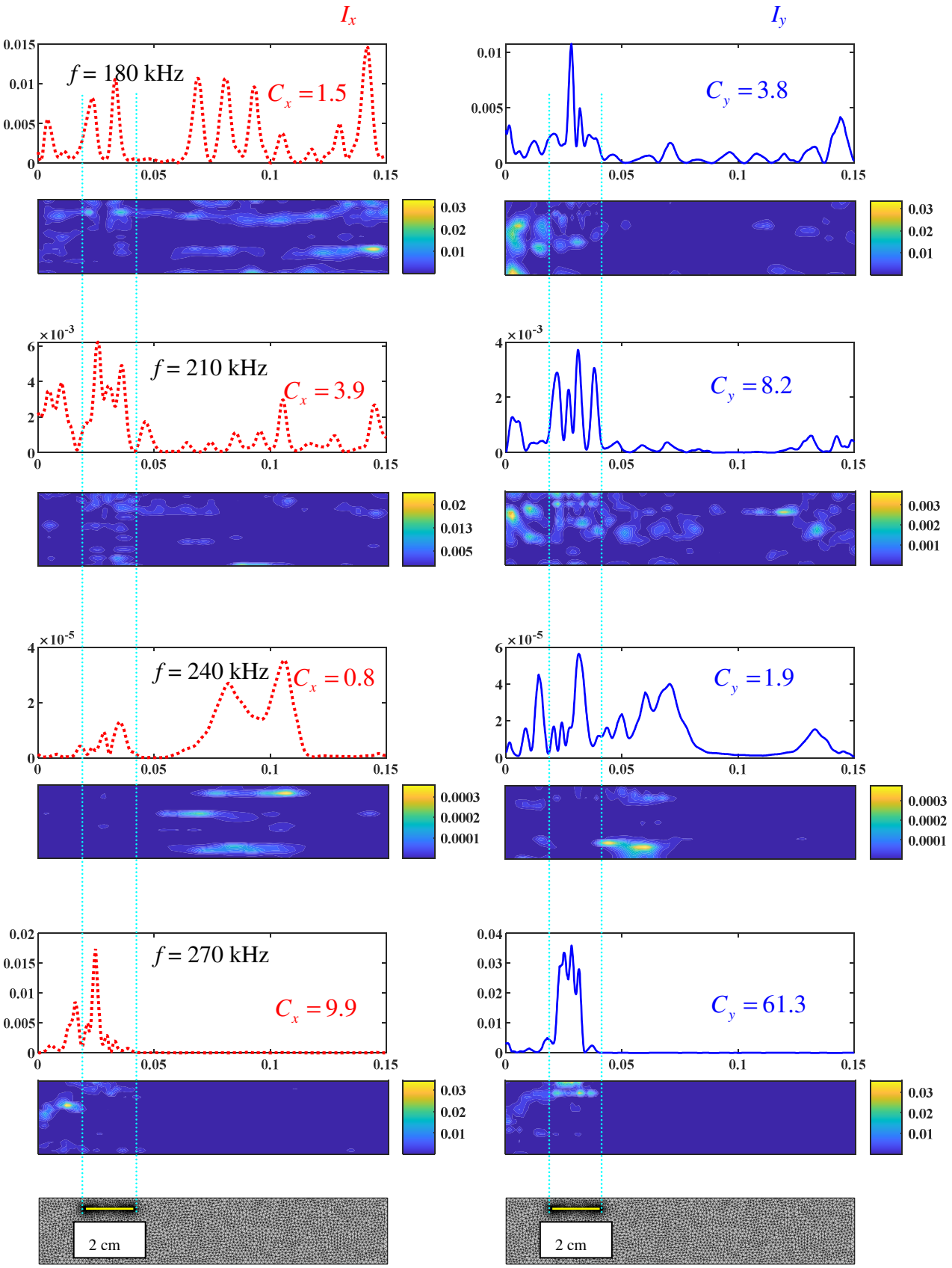

Fig. 12. Same is in Fig. 10 but for 2 cm crack size

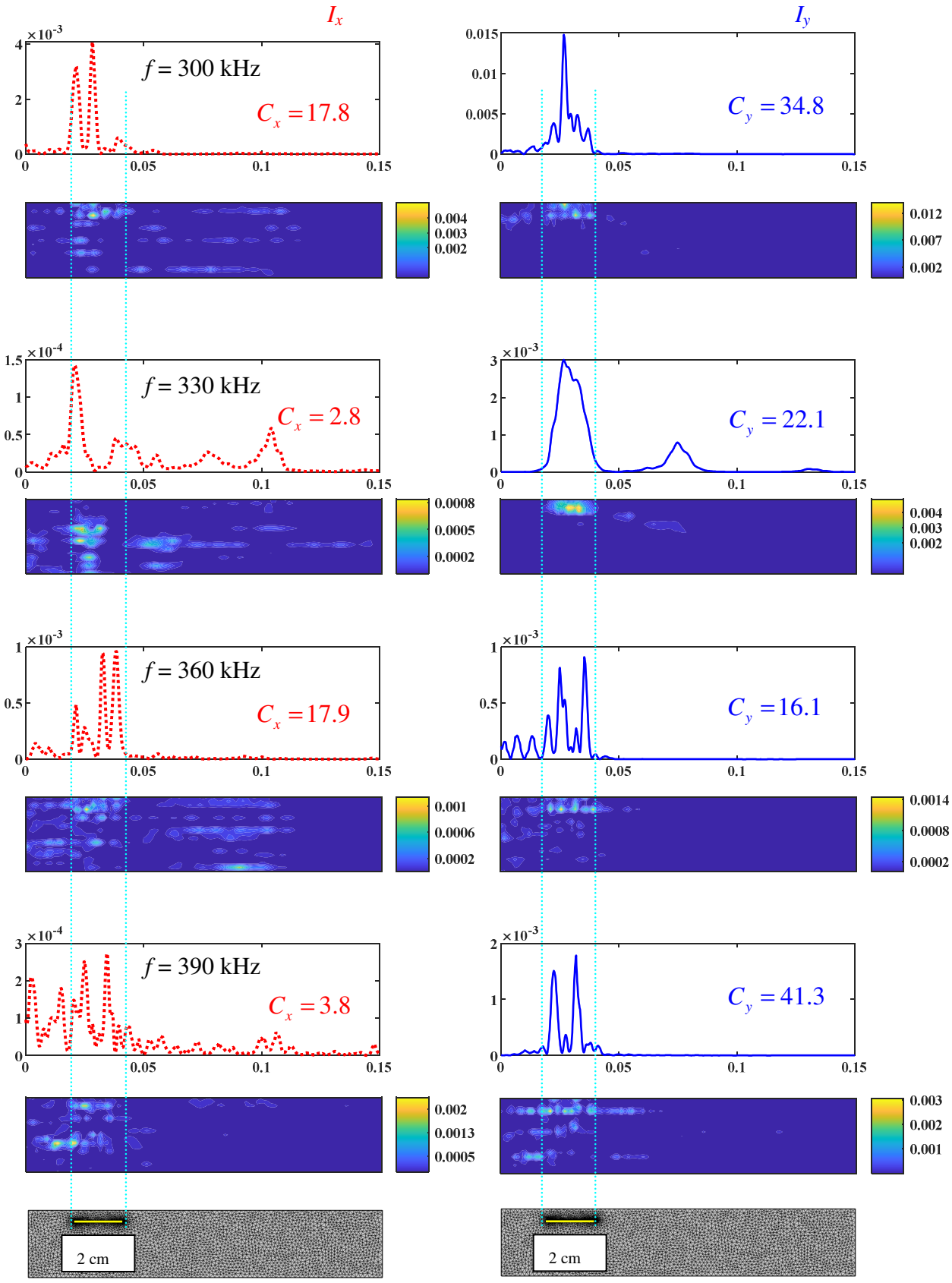

Fig. 13. Same as in Fig. 11 but for 2 cm crack size

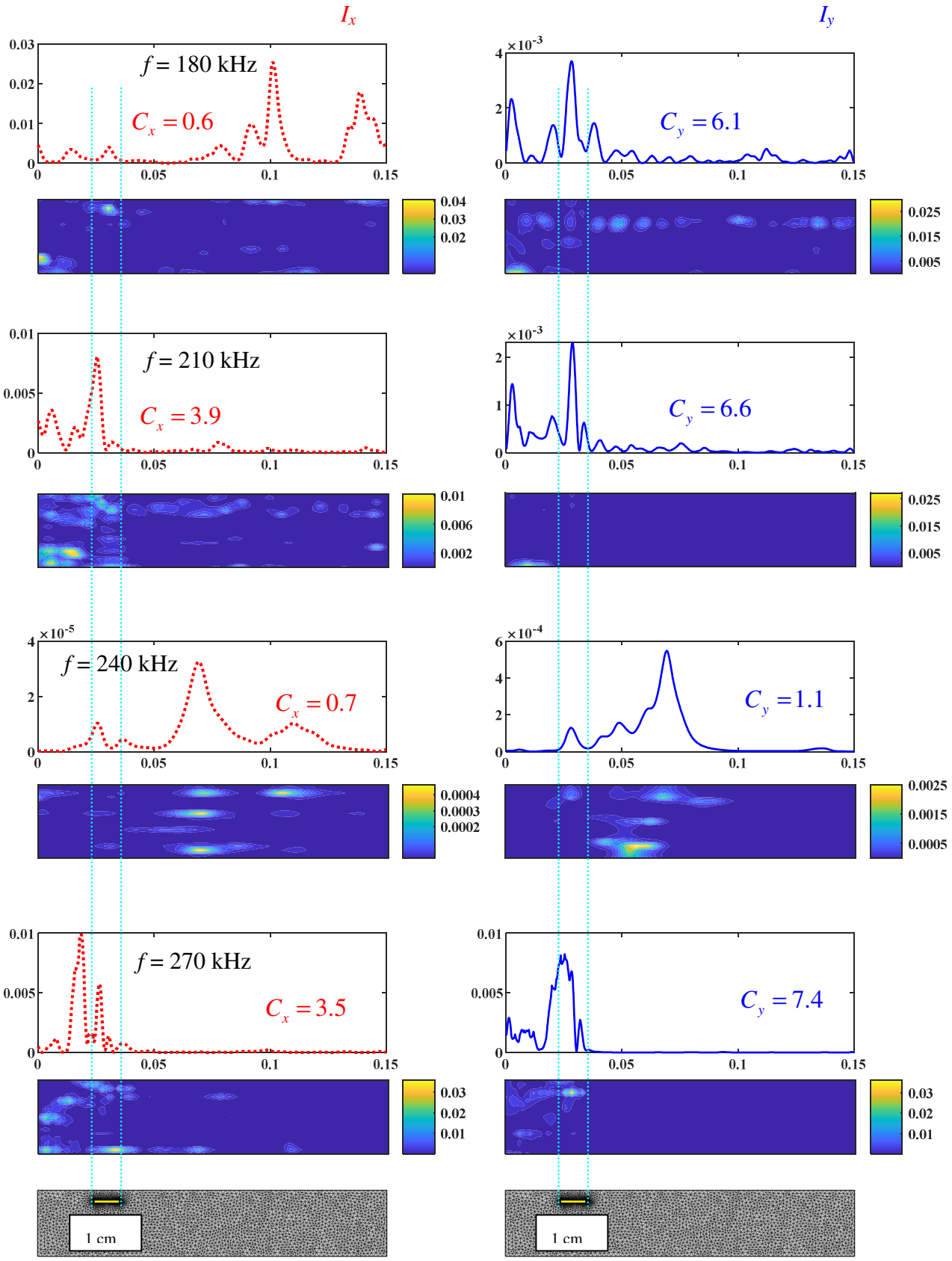

Fig. 14. Same as in Fig. 10 but for 1 cm crack size

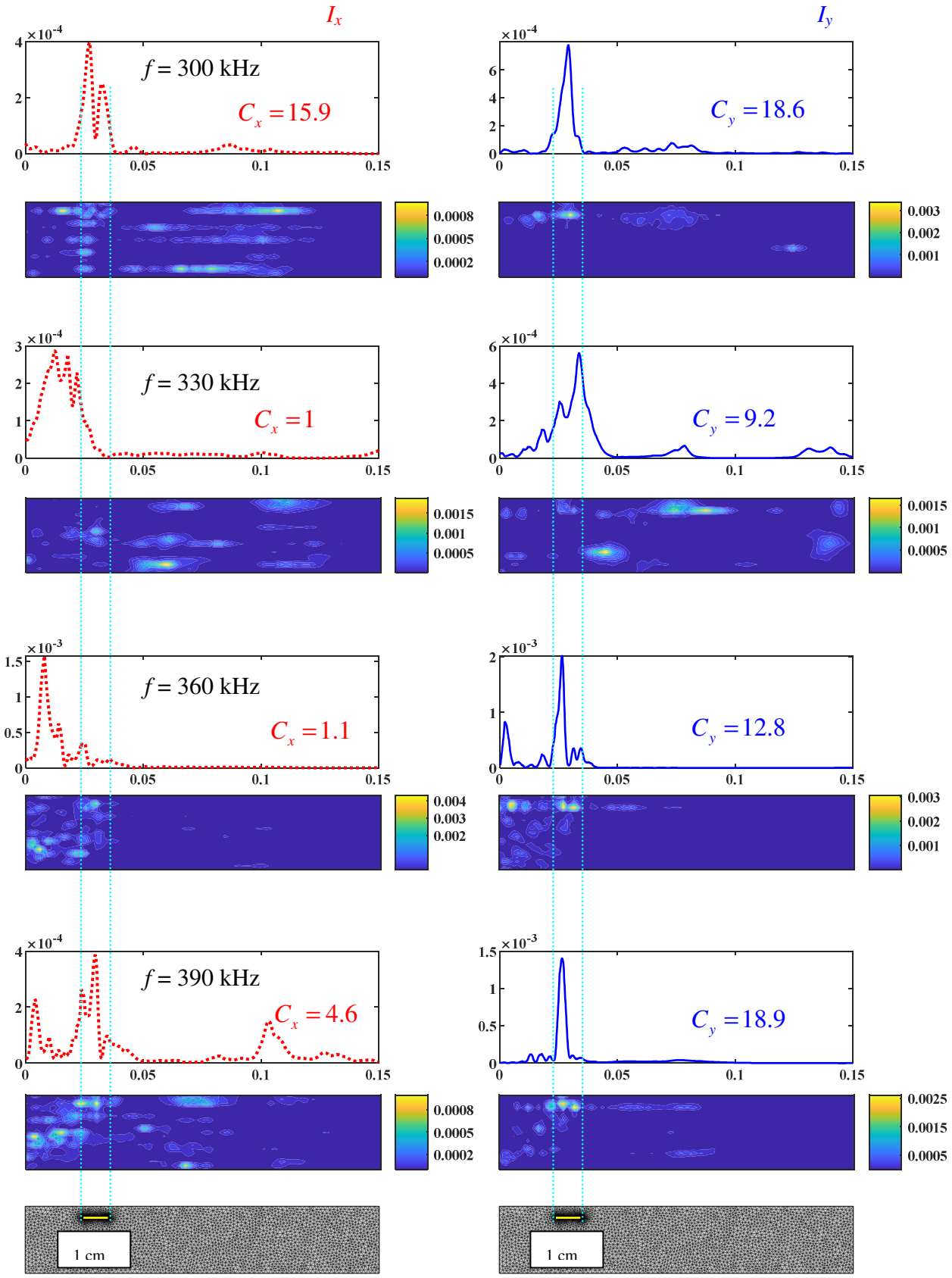

Fig. 15. Same as in Fig. 11 but for 1 cm crack size

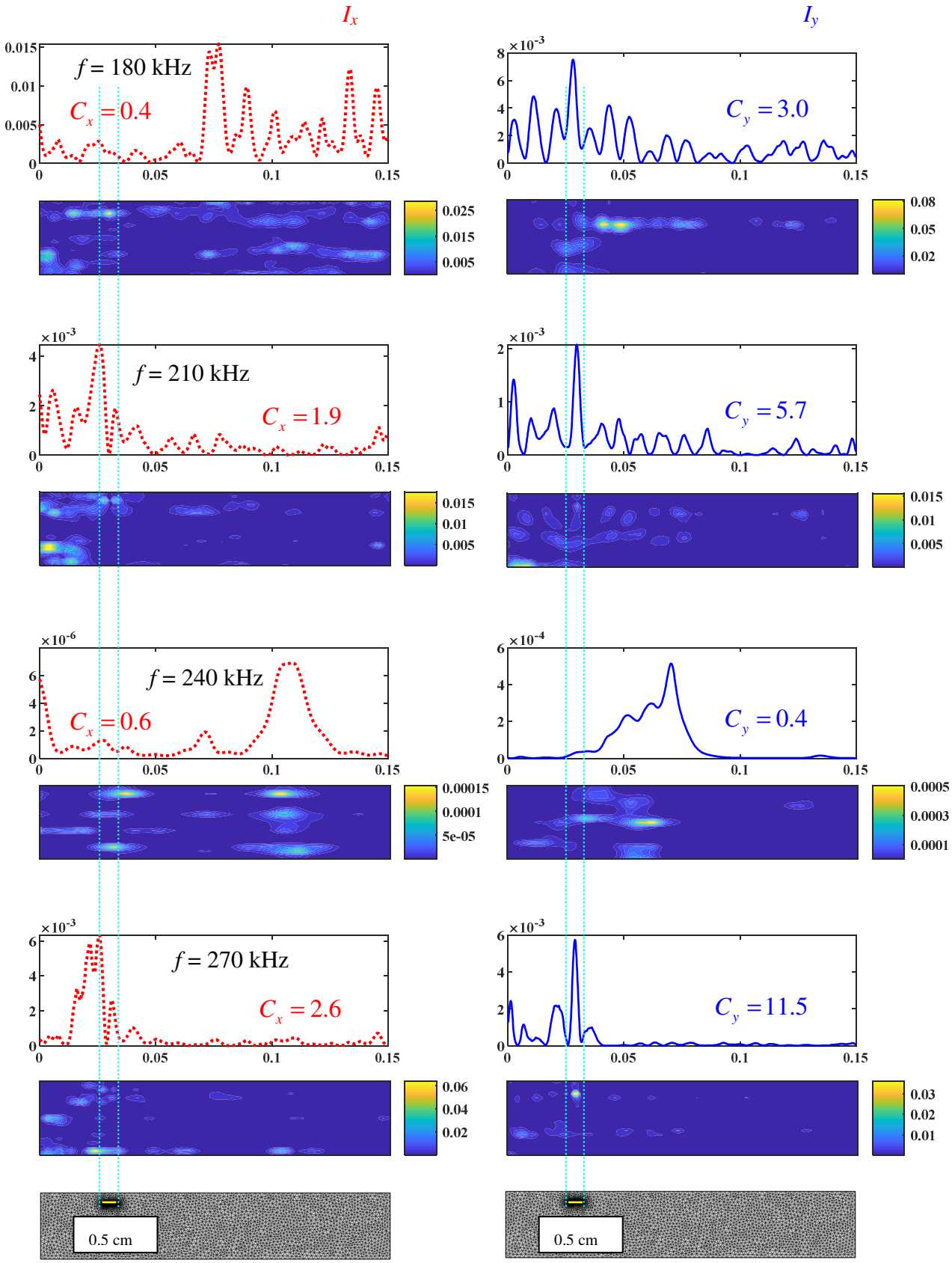

Fig. 16. Same as in Fig. 10 but for 0.5 cm crack size.

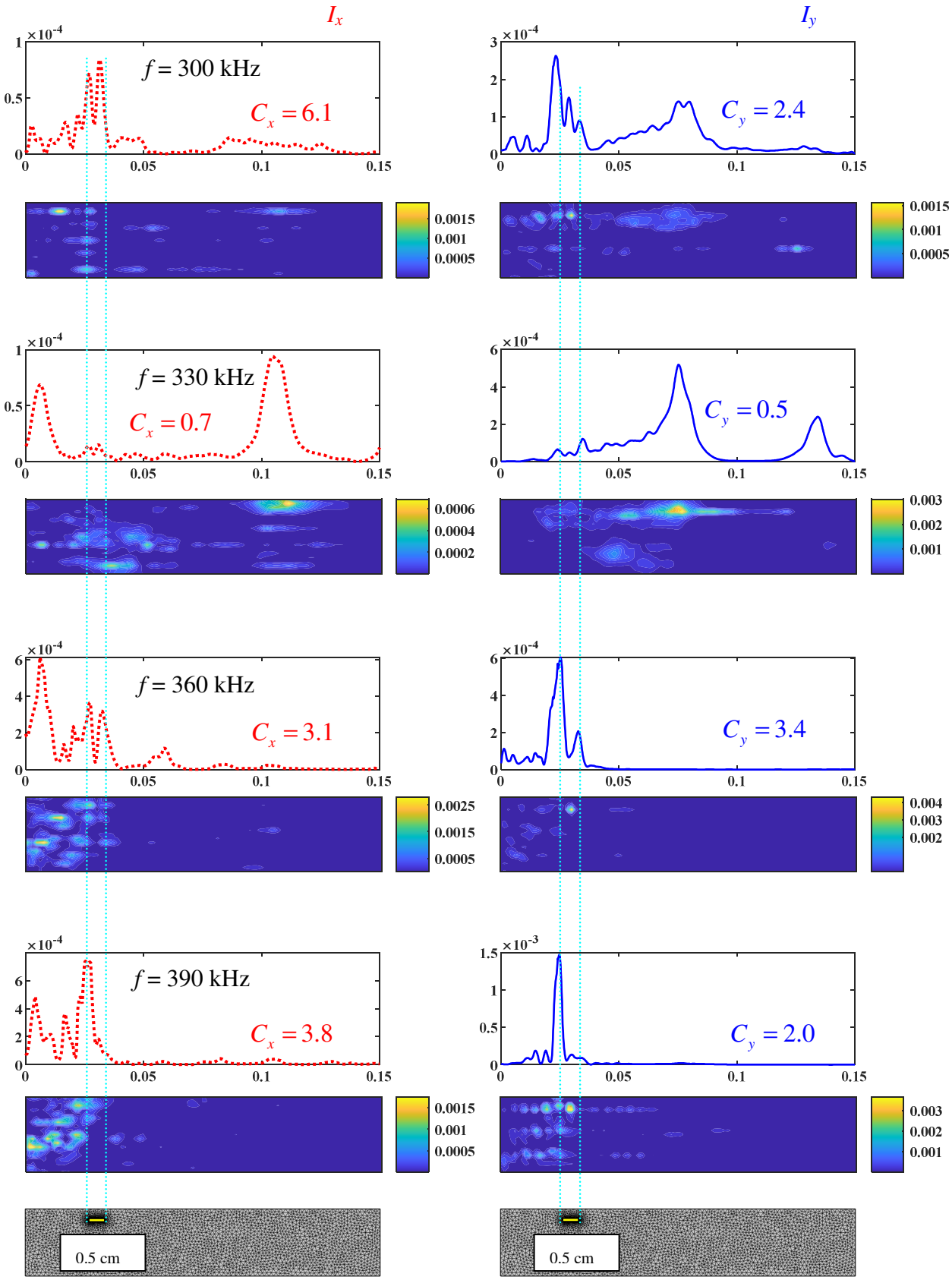

Fig. 17. Same as in Fig. 11 but for 0.5 cm crack size.

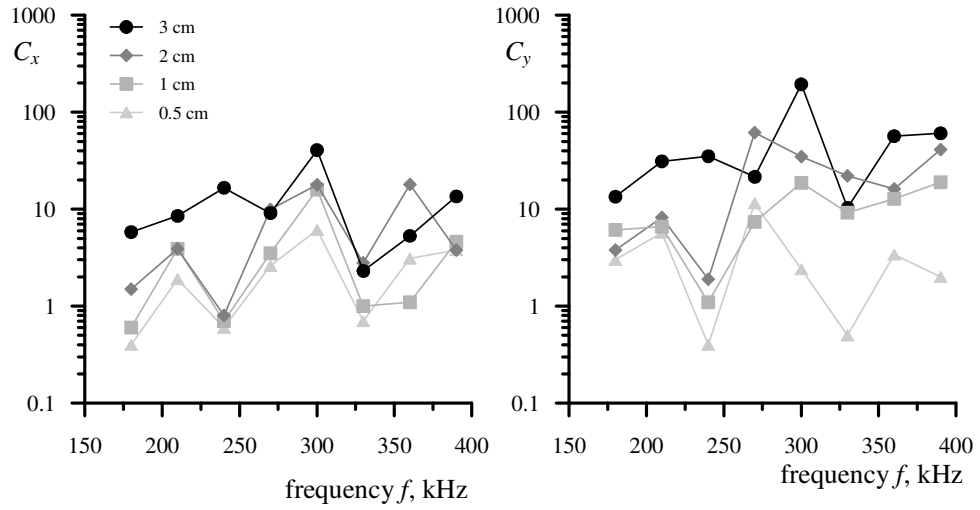

Fig. 18. Frequency dependences of image contrasts $C_{x,y}$ defined as average values $I_{x,y}$ within x-range corresponding to the crack divided by the related averages outside of the crack (Eq. 4). Four different curves in each graph are plotted for various crack sizes, explained in details **[Ale-23]**. *The data correspond to Figs. 10-17.*

Another conclusion drawn from Fig. 18 is that the contrast C_y is generally higher than C_x, with a possible reason related to the highly asymmetric normal reaction curve Eq. (30) of Chapter II in compression and in tension. The effect of totally different normal crack stiffness in the open or closed state can produce a higher nonlinear contribution than friction, while the latter remains an important and non-negligible component of the entire contact interaction.

2.4.3. Effect of roughness parameter *C* and of viscous damping $\eta_{b,v}$ on damage images

The previous section reveals the influence of frequency and crack size on image robustness; however, the impact of two other parameters remains to be evaluated. These are roughness-related coefficient *C* and viscosities η_b, η_v.

The former one is an essential part of the contact model and represents a combination of several characteristics describing, amongst others, composite roughness of inner crack faces, while the other one is *a priori* known material constant. As mentioned, here we use a guessed but realistic value of *C* coefficient, and examplar magnitudes for η_b, η_v which are highly exaggerated for metals and realistic for epoxy-based composites. In this situation, it is important to make sure that the uncertainty related to the choice of these parameters does not considerably impact the final images of damage.

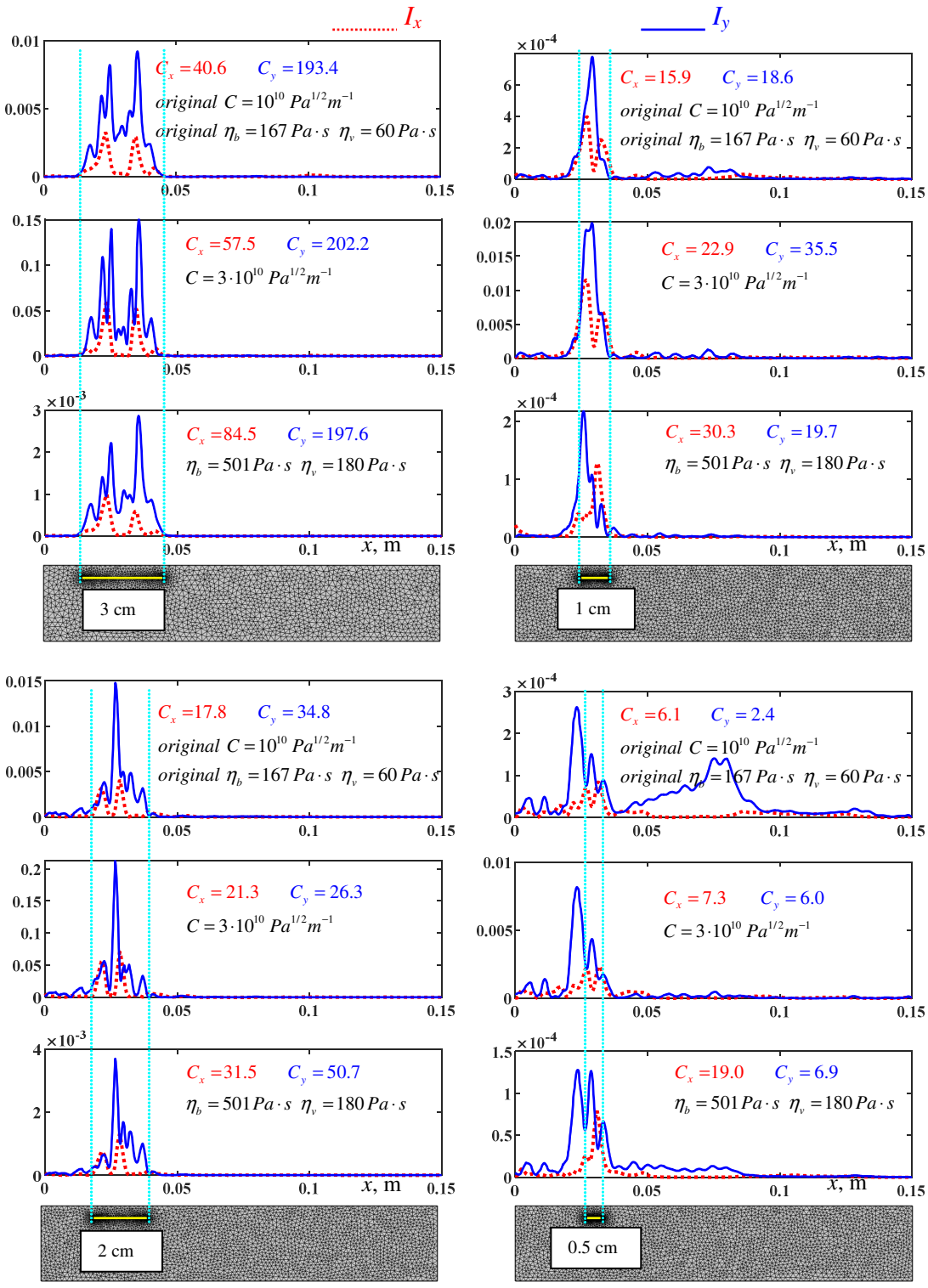

Fig. 19. Impact of roughness parameter C and attenuation $\eta_{b,v}$ on nonlinear images of damage at f=300 kHz. For each crack size, three images are plotted: one with original values of C and $\eta_{b,v}$, and two with increased C and $\eta_{b,v}$, respectively. The crack depth is 0.5 cm in each case. Figure corresponds to **[Ale-23]**.

In Fig. 19 it is shown that a considerable variation in each of C and $\eta_{b,v}$ results in a weak shape change in $I_{x,y}$ together with an appearance of a scaling factor. Correspondingly, the

image contrast is also affected slightly that makes us hope that the possibility to detect a crack in a certain configuration weakly depends on these two parameters. The illustration is made for the optimal frequency f=300 kHz found in the previous section.

2.4.4. Crack images for various crack depths

Another question that remains unanswered so far is about an influence of a crack depth on crack visibility via surface stationary wave measurements. Without pretending to present a full parametric study, here we discuss some results for large cracks (3 and 2 cm length) buried at different depths (Fig. 20).

As in Section 2.4.3, the excitation frequency f is fixed at 300 kHz to potentially maximize the contrast, although for various depths the optimal frequency can shift. As expected, visibility of cracks generally drops as long as their depth increases. There are, however, two exceptions encountered for a crack of 2 cm length buried at 2 cm and 2.5 cm (two last plots at the right in Fig. 20, dotted curve for C_x).

A possible explanation can be related to specific features of stationary wave patterns at higher harmonics. Indeed, our earlier numerical results **[Del-18]** indicate a nontrivial radiation diagram of a crack insonified by a sinewave signal of finite duration. For infinite in time sinewave excitation, a complex radiation diagram should remain including several maxima and minima (or "petals") as well as diffused components. From that point of view, all peaks in images shown in Figs. 10-17, 19 and 20 can eventually be interpreted as "petals" in the radiation diagram. For cracks located close to the surface, the petals could not diverge far away as for deep cracks and therefore produce higher contrast.

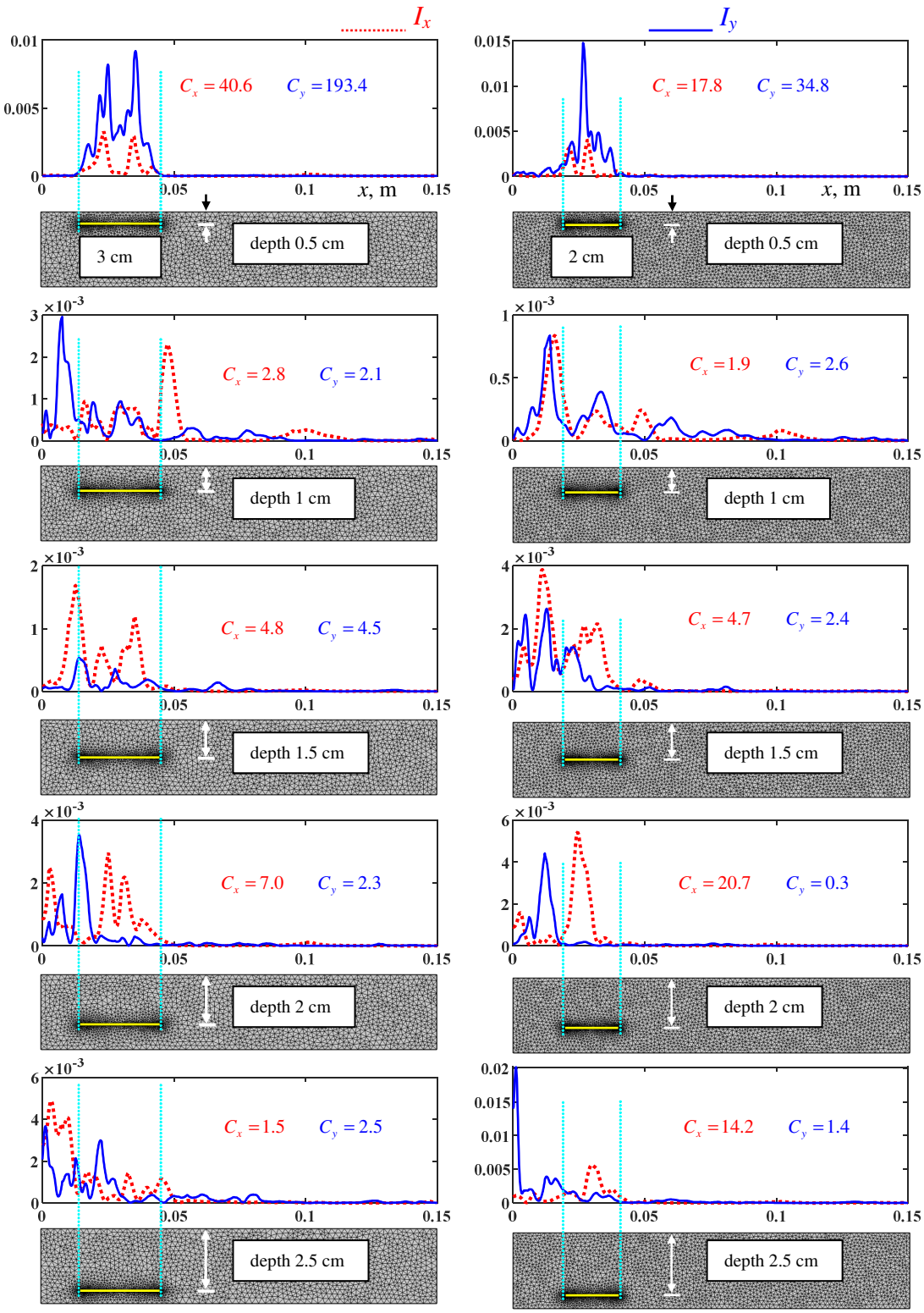

Fig. 20. Nonlinear images for samples containing a crack of 3 cm and 2 cm length (at the left and at the right, respectively) buried at depths of 0.5, 1, 1.5, 2, and 2.5 cm. The samples are excited by a continuous wave of a frequency 300 kHz. Figure source **[Ale-23]**.

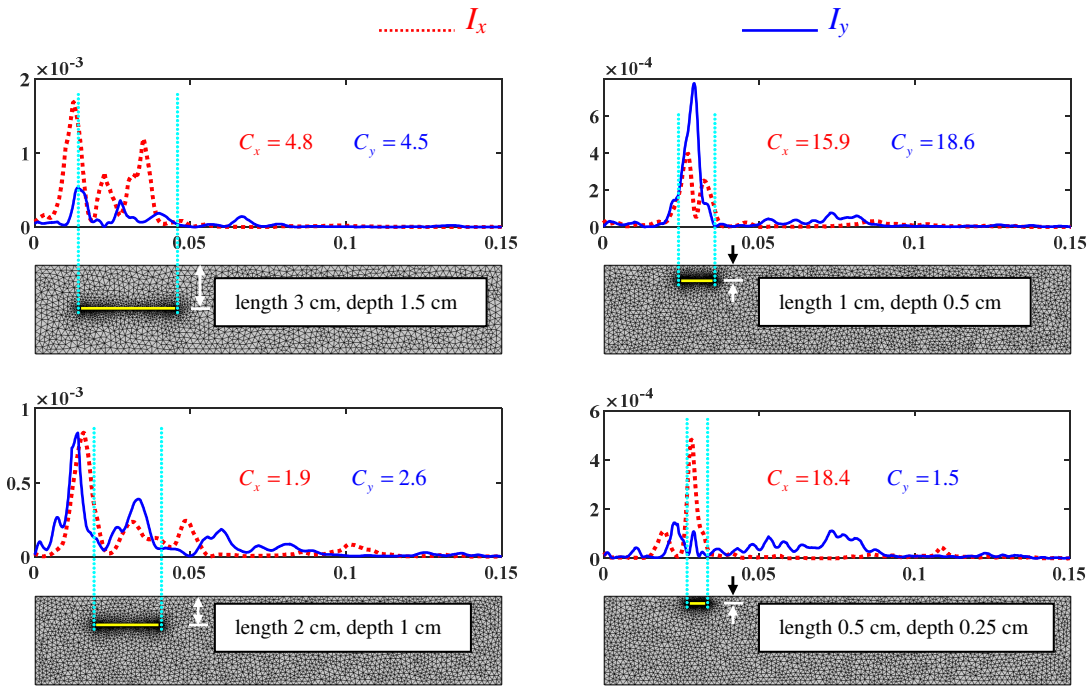

Fig. 21. Nonlinear images of cracks having the same length/depth ratio in samples excited at 300 kHz. Figure taken from **[Ale-23]**.

It is important to mention that the radiation diagram for stationary waves depends not only on geometric parameters of the crack but also on geometry of the entire calculation domain as it represents a result of global interference in the sample. To illustrate this fact we plotted four damage images for cracks having the same length/depth ratio (Fig. 21). In these particular cases, the results indicate that crack depth is more important than the length; tiny cracks located very close to the surface are still visible.

2.5. Conclusions

In Section 2, we applied the previously developed numerical MMD-FEM method of solving acoustic problems in materials with frictional cracks to imitate nonlinear acoustic imaging techniques. As a first step, we considered a number of 2D plate fragments with a crack parallel to plate's surfaces. The samples were excited by a harmonic acoustic wave having a certain frequency. After decay of the transient regime, the solution is presented in a form of a stationary wave whose harmonics are generated by contact acoustic nonlinearity associated with the presence of crack. These results have been recently published in **[Ale-23]**.

Numerical modeling allowed us to identify cases where successful detection of crack position and extent is possible or not. To quantify the image quality, we introduced image contrasts with respect to u_x and u_y wave components. Then, through a series of examples, we studied their dependences on the excitation frequency, on the crack length and depth, as well as on

parameters related to crack roughness and material attenuation. Numerous computer simulations suggest the following conclusions:

- In the framework of the proposed MMD-FEM model, it is possible to detect a vast multitude of cracks with different lengths and depths in a way similar to real experiments (e.g. via laser vibrometry).
- There exist optimal frequencies at which imaging is more robust.
- Image quality does not depend on material and geometry parameters in a simple and monotonous way; rather, examining crack depth proves more crucial than its length in accurately assessing structural strength and avoiding misidentification of surface-level issues. This complexity arises from the formation of a complex stationary wave pattern in the generated harmonics in each case.
- Even small cracks but located close to the surface are visible via nonlinear analysis of the surface fields.
- There is an important technical limitation related to the time of stationary wave formation; in real experiments this waiting time does not impose any difficulty while in numerical modeling the calculation time becomes high unless strong material attenuation combined with low-reflecting boundary conditions are used.

3. Frequency mixing

Besides the methodology based on the single frequency excitation and on detection of the generated harmonics, there exists also a method that uses two sinusoidal signals on input. While exiting two frequencies f_I and f_{II}, one expects that damage-related nonlinearity will generate signal components with mixed or combination frequencies, $f_I \pm f_{II}$. From an experimental point of view, such an approach is preferable since higher harmonics can be generated in the measuring system due to its imperfect linearity, while the combination frequencies can appear only due to damage.

In this Section, we extend our MMD-FEM model onto this case also by assuming $f(t) = A_I \sin 2\pi f_I t + A_{II} \sin 2\pi f_{II} t$ (see Fig. 1). It is convenient to relate f_I and f_{II} through some base frequency f_B by assuming, for instance, $f_I = 3f_B$, $f_{II} = 5f_B$. In that case, all combination frequencies, even of higher order, will coincide with one of the frequency grid node.

The period of such a signal is $1/f_B$. Keeping other modeling parameters values as in the previous section, we observe 100 periods of acoustic excitation, having in mind that the level

of attenuation ensures stable stationary waves formation with lower anharmonicity than the one generated by the damage-induced nonlinearity. Low-reflecting boundaries aid energy dissipation, effectively shortening transient phase. Other parameters here take the same values as previously: Young's modulus $E = 7 \cdot 10^{10}\, Pa$, Poisson's ratio ν = 0.33, density of 2700 kg/m³, bulk and shear viscous damping $\eta_b = 167\, Pa \cdot s$, $\eta_v = 60\, Pa \cdot s$, and roughness-related coefficient $C = 10^{10}\, Pa^{1/2} m^{-1}$. All cracks are positioned with a uniform center at C_{cr} =3 cm. The variable excitation amplitudes $A_{I,II}$ (with $A_I = 6.6 \cdot 10^{-8}$ m and A_{II} = 1.2 A_I) have been implemented across all frequencies to ensure a strain value ε_{cra} approximately at 10^{-6} or higher within the vicinity of the crack.

As previously, the transition process duration and the beginning of the stationary solution is established for the intact sample. The related deviation is guaranteed to be less that a typical image value. The aperiodicity can only be created by proper nonlinear resonances related to damage, which is discussed in the next section in more detail.

3.1. Generated harmonics and excited nonlinear defect resonances

As previously, our consideration is based on the synthetic u_x and u_y time curves at various x-points (specifically 1000 points) situated on the upper surface of the sample and on the subsequent Fourier analysis of the stationary solution i.e. the concluding signal's "tail" free of the transient regime influence.

Suppose that the stationary tail of the signal determined for the intact sample has the duration N_p times the quasi-period f_B. Then the base frequency f_B will have number N_p in the Fourier spectrum. Excitation at f_I and f_{II} will produce mixed frequencies $f_I \pm f_{II}$ and, if nonlinearity and the excitation amplitudes are strong enough, second-order interactions as well. Anyway, frequencies f_m generated as a result of such a process will be multiples of f_B (f_m=$m\, f_B$), where m= 1, 2,…, and the wave field will remain periodic at any point of the sample.

This frequency content cannot be modified by the presence of linear resonances in the system, however, if it comprises some nonlinear resonance features, new frequencies can appear. Since the resonances are nonlinear and therefore amplitude-dependent, the new frequencies will differ from f_m=$m\, f_B$. Correspondingly, the signal tail will loose periodicity.

It is remarkable that the nonlinear resonances are more frequent for the frequency mixing case than for the harmonic generation. A possible reason is that the spectrum contains a lot of strong harmonics f_m=$m\, f_B$, whereas the higher harmonics generated in the single frequency

excitation case quickly weakens as long as their order increases. Richer harmonic content has more chances to excite proper nonlinear resonances.

In accordance with the above considerations, it makes sense to introduce two separate nonlinear criterions based on the nonlinear frequency mixing:

$$I_{x,y}^{NL} = \sum_{\substack{n \neq I,II \\ n=mf_B}} \frac{\left(A_{x,y}^{n}\right)^2}{\left(A_{x,y}^{I}\right)^2 + \left(A_{x,y}^{II}\right)^2}, \tag{5}$$

and on the nonlinear resonances

$$I_{x,y}^{LDR} = \sum_{n \neq mf_B} \frac{\left(A_{x,y}^{n}\right)^2}{\left(A_{x,y}^{I}\right)^2 + \left(A_{x,y}^{II}\right)^2}. \tag{6}$$

As indicated above, the criterion $I_{x,y}^{NL}$ based on frequency mixing comprises all harmonics multiples of f_B, except the excitation frequencies f_I and f_{II}. In contrast, the second criterion contains all other frequency components i.e. it takes into account resonances.

Each of these criterions as well as their sum

$$I_{x,y} = I_{x,y}^{NL} + I_{x,y}^{LDR} \tag{7}$$

can be indicators of damage. In what follows as consider them separately.

Figs. 22-35 illustrate the spectra of the stationary solution (a) and the nonlinear images Eqs. (5)-(7) plotted together with the meshed sample with the crack indicated (b). As in the previous section about harmonic generation (Section 2.2, Figs. 4-5) we added also the entire record of $u_{x,y}$ (c) as well as their first and last fragments shown together in set (d). The following exemplar cases with at the same frequency f_B=40 kHz are illustrated:

- Figs. 22-23: crack of 2 cm length and 5 mm depth, weak resonance in the u_x spectrum;
- Figs. 24-25, crack of 3 cm length and 2.5 mm depth, no resonance;
- Figs. 26-27, crack of 3 cm length and 5 mm depth, strong resonance in the u_x spectrum and very strong resonance in the u_y spectrum;
- Figs. 28-29, crack of 3 cm length and 10 mm depth, resonances are masked by stronger harmonics;
- Figs. 30-35, crack of 1 cm length and 2 mm depth, for the original amplitudes as well as for amplitudes $\sqrt{10}$ and 10 times weaker, resonances occur in the u_x spectrum at frequencies independent on the excitation amplitudes, and they also occur in the u_y spectrum at other frequencies, which are also independent on the excitation amplitudes.

It can be seen that the structures of resonances is quite complex, and that a more profound study is necessary that would requite many more examples that would possibly allow to associate the resonance frequencies with damage features. The resonances can be very strong as in Fig. 27 where they completely destroy the periodic behavior, or they can be masked by stronger harmonics as in Figs. 24-25. Due to this fact, the $I_{x,y}^{LDR}$ criterion is of secondary importance, since in many situations its value is negligible while the $I_{x,y}^{NL}$ criterion identifies damage in a robust way (Fig. 23).

One important feature deserves more attention. The concluding series Figs 30-35 is made for the same sample geometry, same frequency as the other images, and for three different amplitude levels. It can be immediately seen that the presence of the crack strongly modifies the propagation conditions for the excitation frequencies whose values at the crack are not proportional to their relative strengths (factor 1.2) near the transducer. We clearly identify three resonance frequencies for the u_x-component (51.2, 129.2, and 209.2 kHz) and three partly intersecting resonance frequencies for the u_y-component (51.28, 70.7, and 129.2 kHz). The resonance strengths can vary due to different excitation conditions, but the resonance frequencies do not depend on the excitation amplitude. This feature makes them similar to subharmonics **[Sol-04]** experimentally found for strongly excited damages materials. Note also that resonance frequencies for multi-cracked solids **[Ost-01]** usually depend on the excitation amplitude (they decrease as long the amplitude increases indicating softening amplitude-dependent behavior). However, we still prefer call these resonances nonlinear since their amplitudes depend on the excitation level in a nonlinear way.

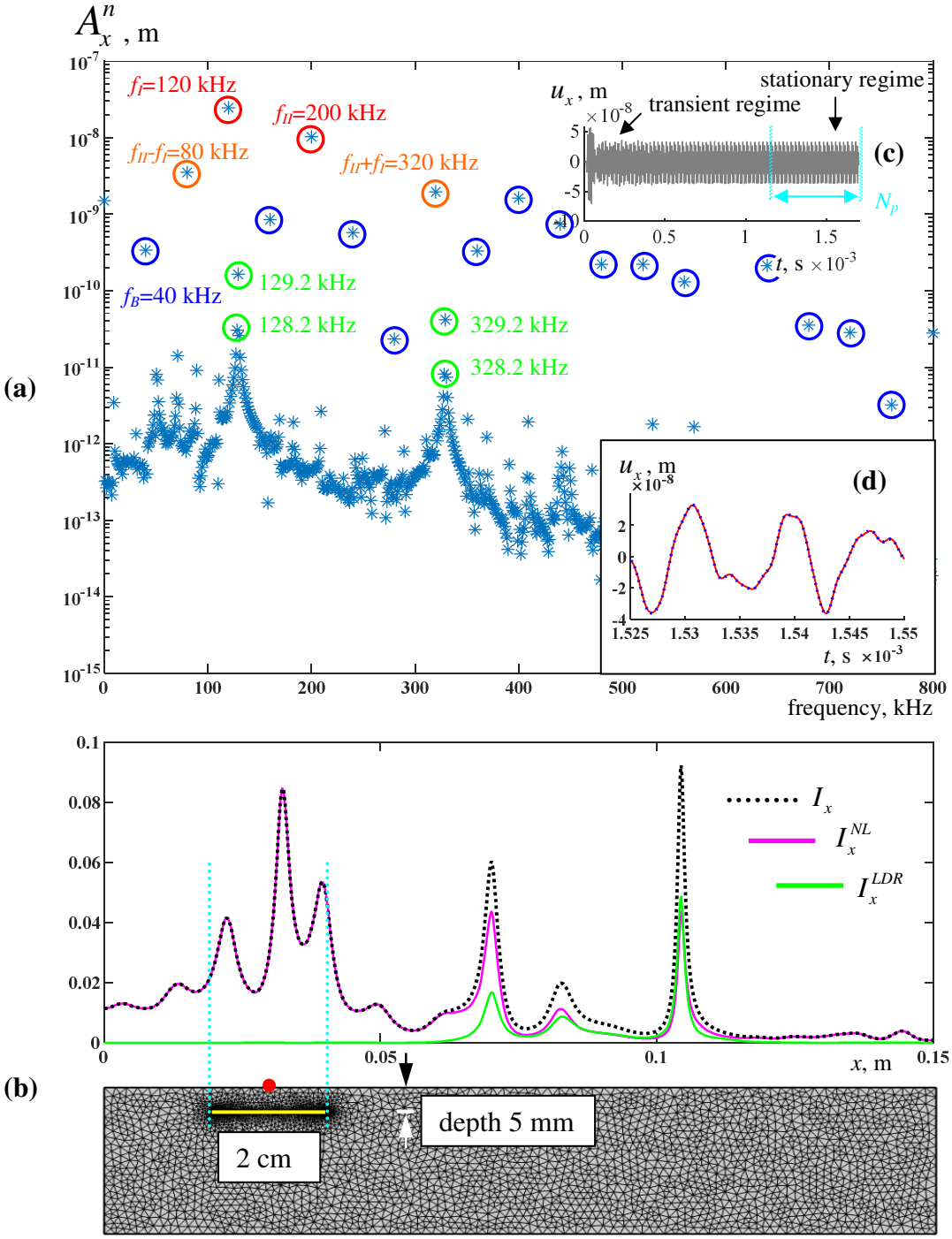

Fig. 22. For the crack of 2 cm length buried at depth of 5 mm : ***(a)*** *spectrum* A_x^n *of displacement* u_x *on the top surface at the crack center (*x=C_{cr}*, red dot in* ***(b)****), with the excited frequencies* $f_{I,II}$ *marked with red circles, combination frequencies* $f_I \pm f_{II}$ *marked with orange circles, and other frequencies generated via nonlinear process marked with blue circles, and LDR components with green circles;* ***(b)*** *images* I_x^{NL}, I_x^{LDR} *calculated accordingly to Eqs. (5)-(6) (pink and green lines) together with their sum* I_x *(black dotted line);* **(c)** *full record of* u_x *over time on the top surface at the crack center;* **(d)** *first and last quasi-periods of the stationary signal's tail.*

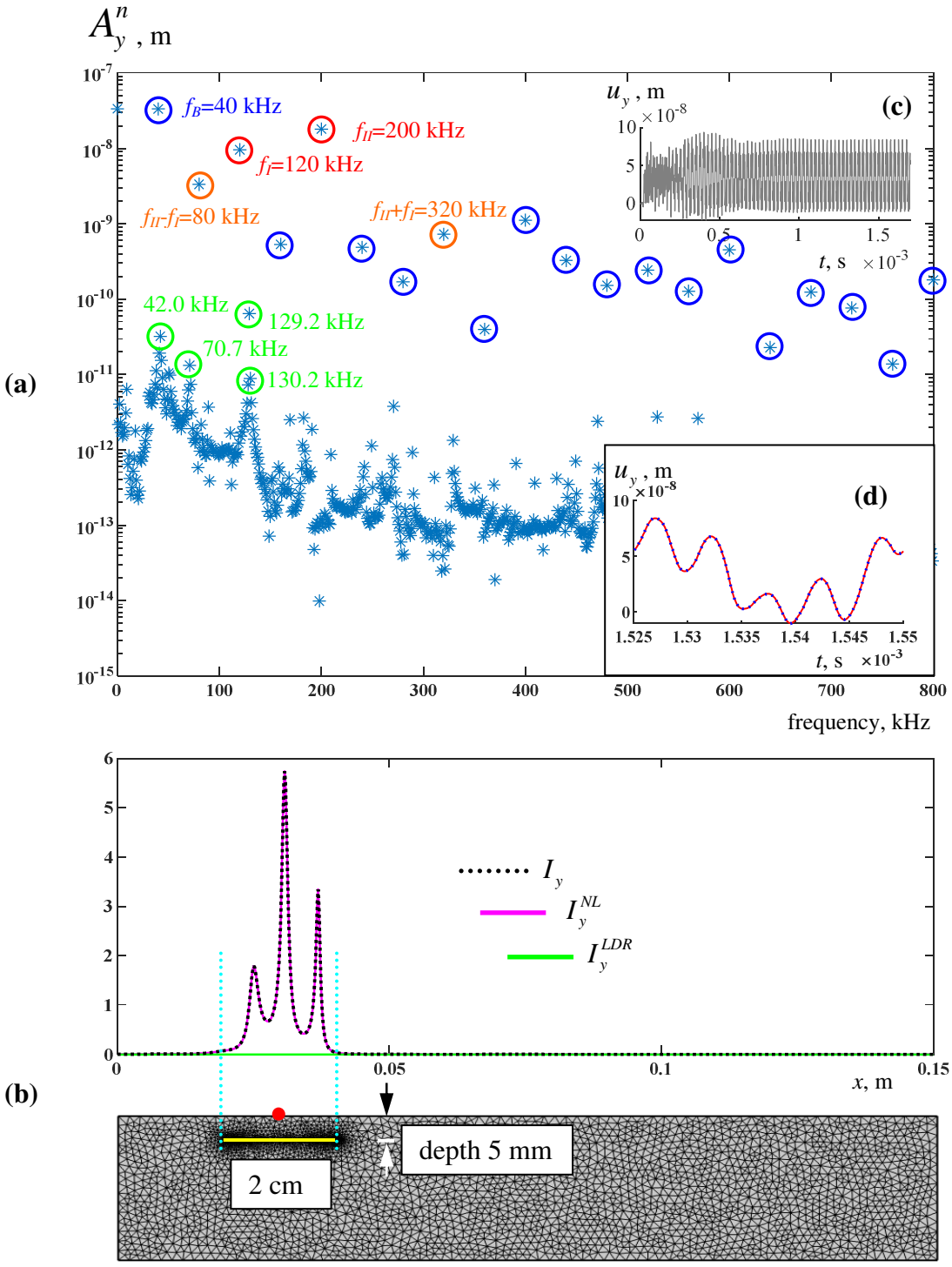

Fig. 23. Same as Fig. 22 but for the y-component.

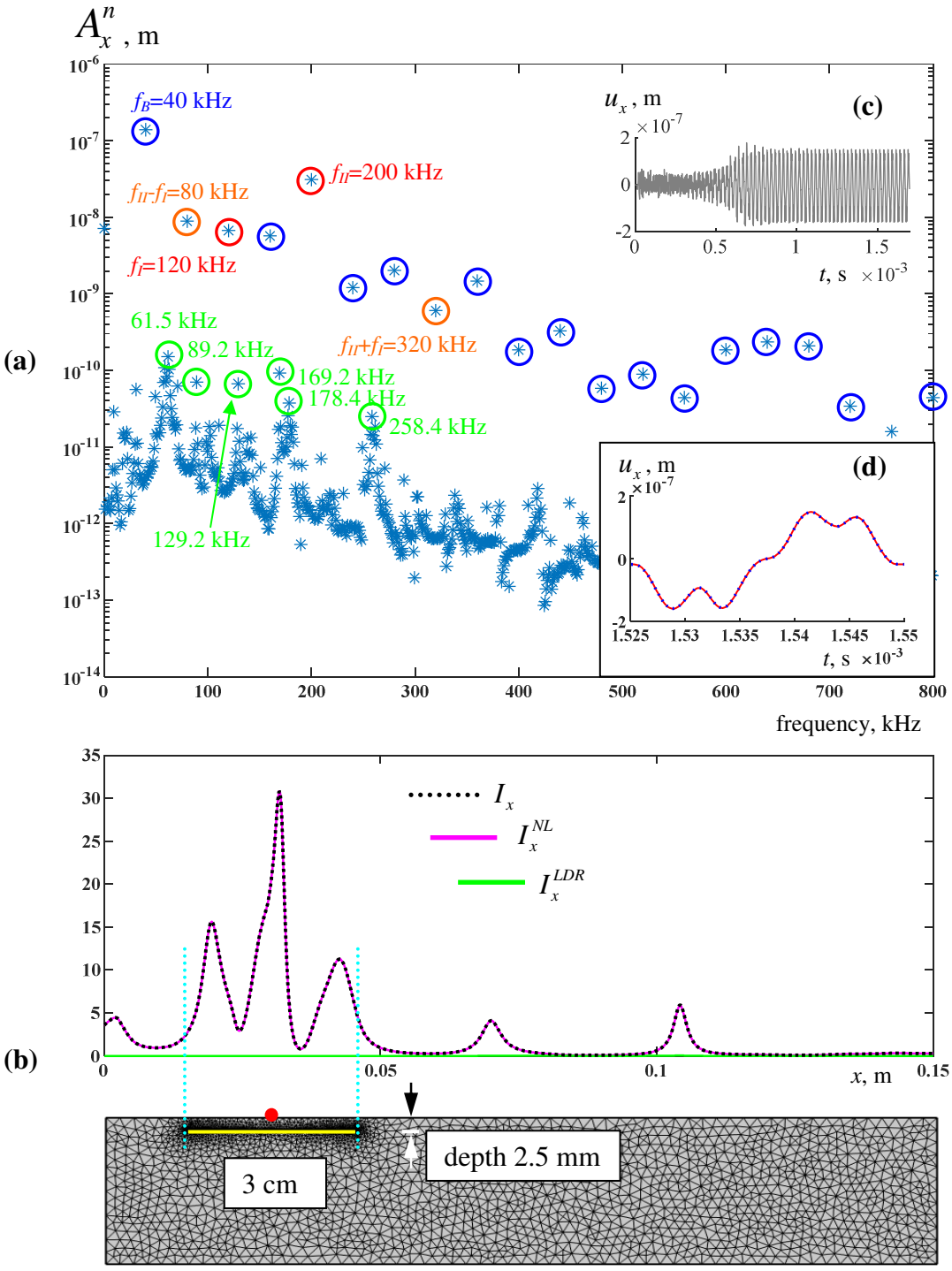

Fig. 24. Same as Fig. 22 but for the crack of 3 cm length buried at depth of 2.5 mm.

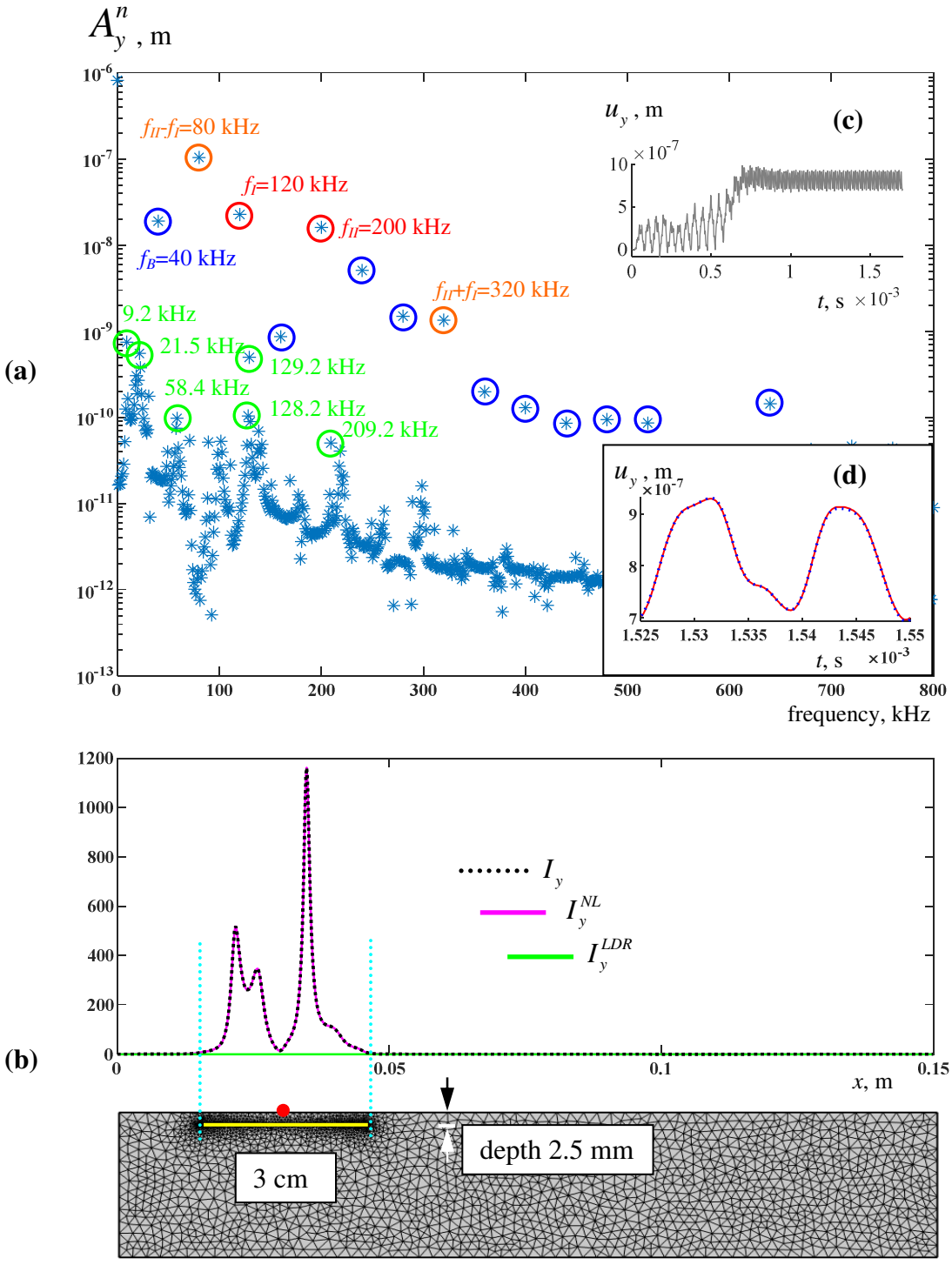

Fig. 25. Same as Fig. 24 but for the y-components.

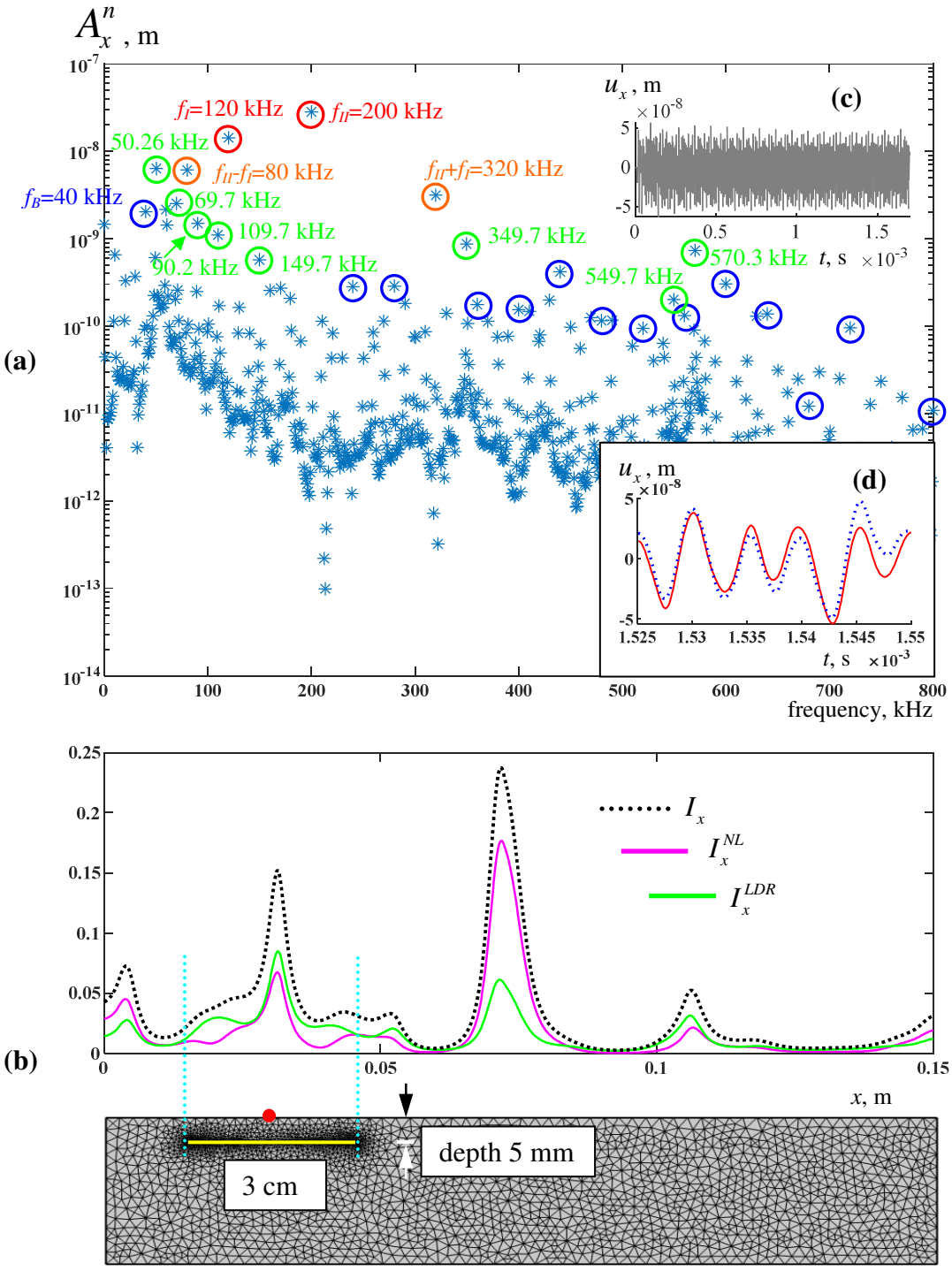

Fig. 26. Same as Fig. 22 but for the crack of 3 cm length buried at depth of 5 mm.

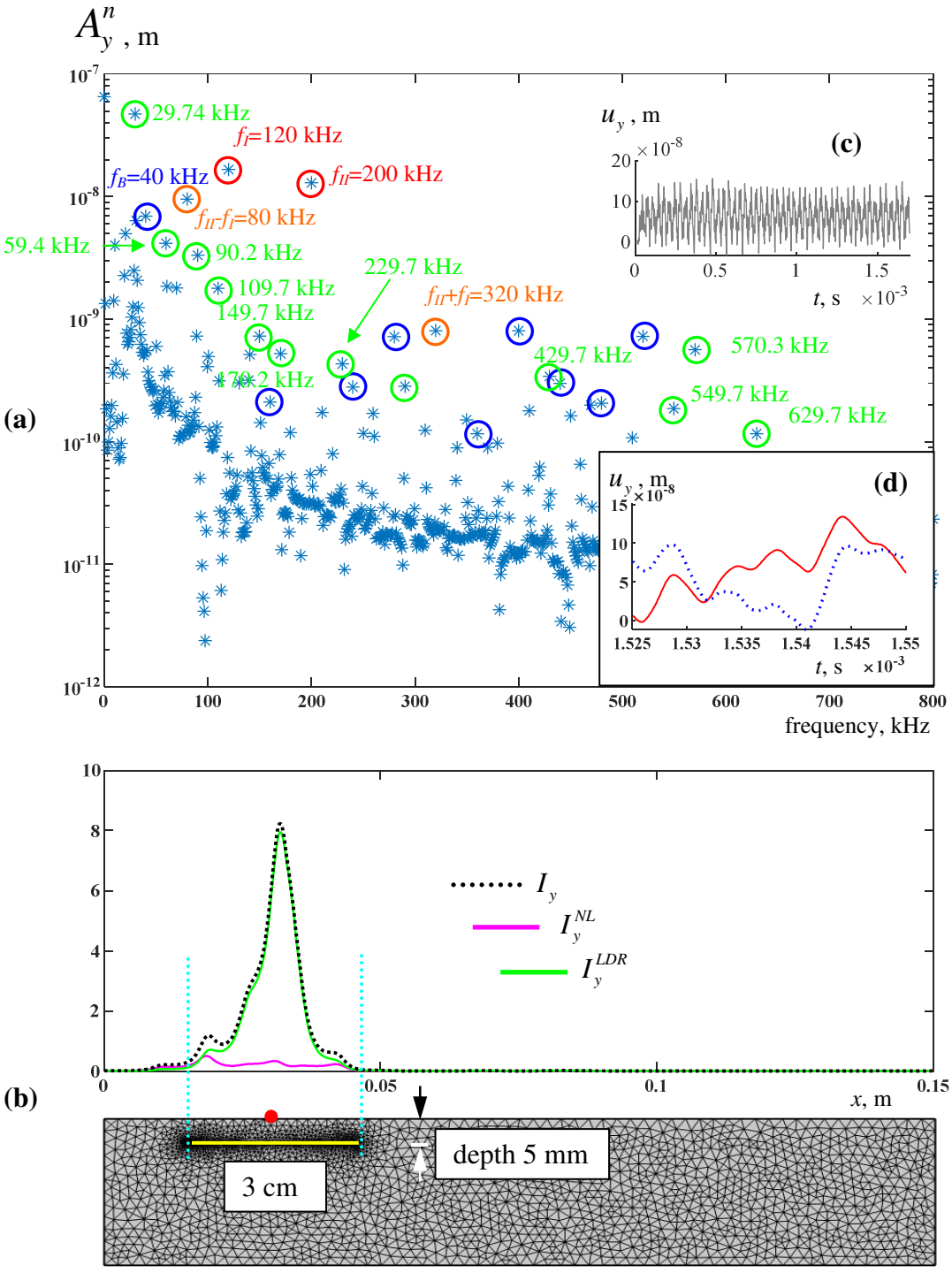

Fig. 27. Same as Fig. 26 but for the y-components.

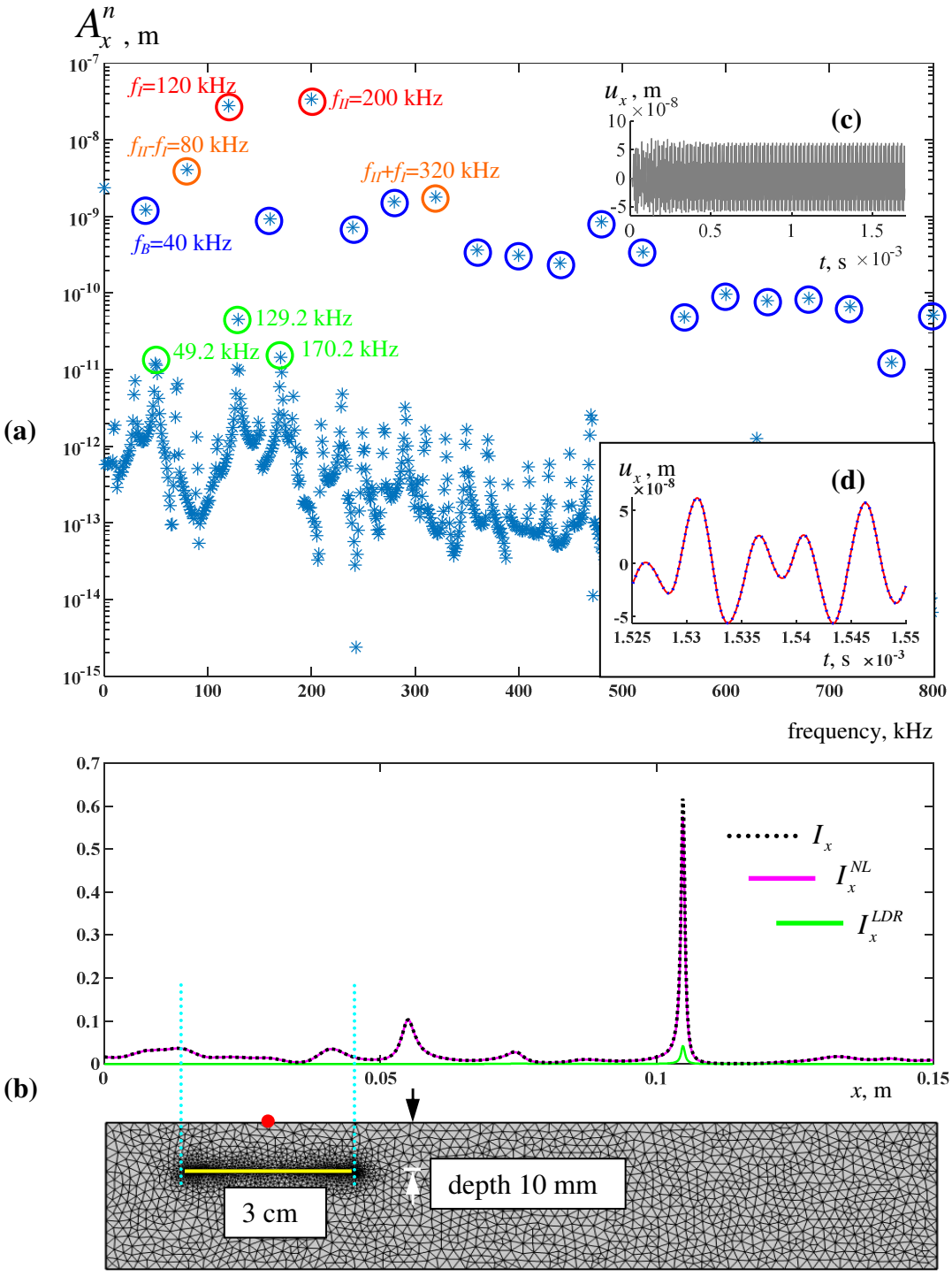

Fig. 28. Same as Fig. 22 but for the crack of 3 cm length buried at depth of 10 mm.

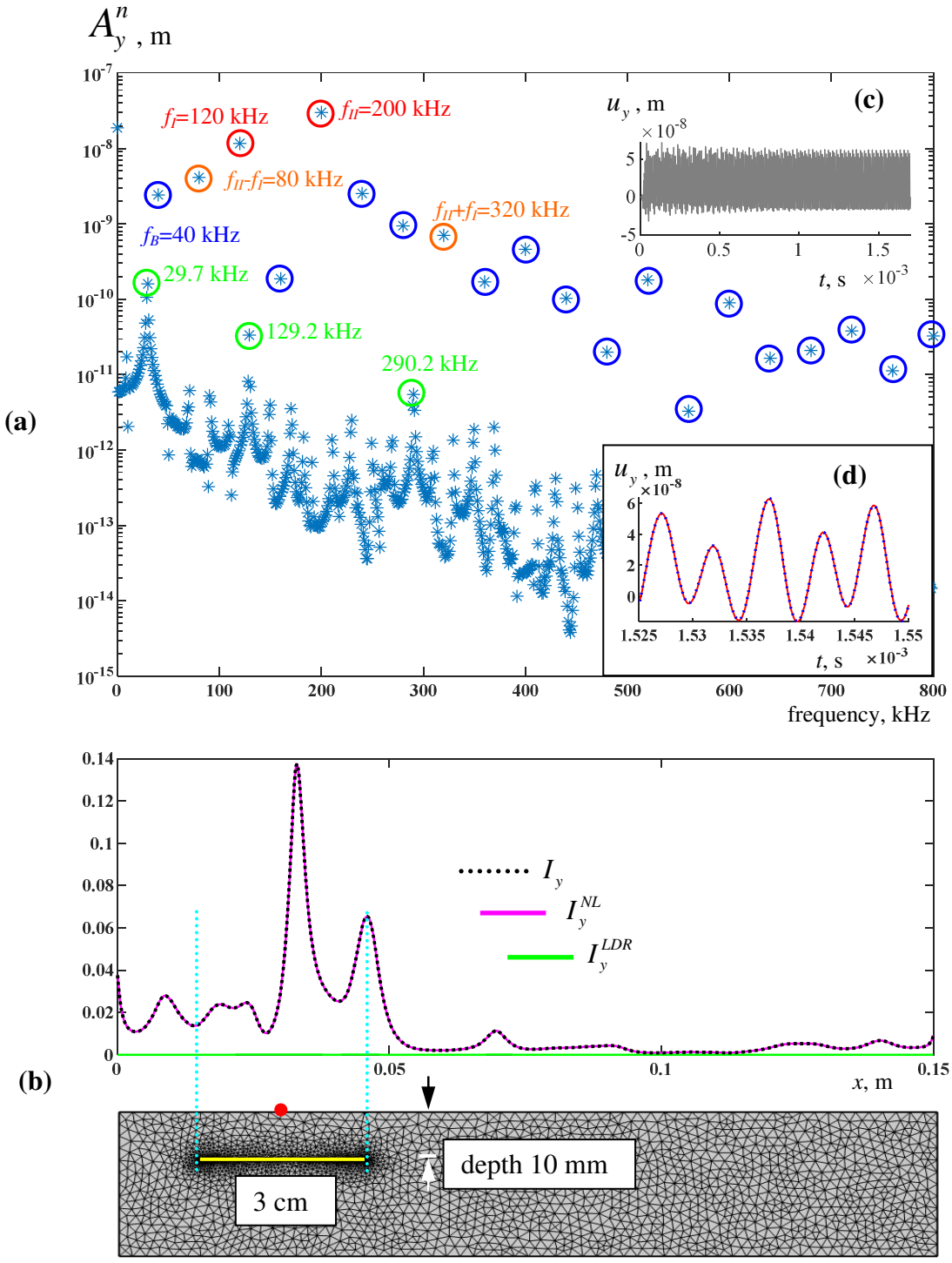

Fig. 29. Same as Fig. 28 but for the y-components.

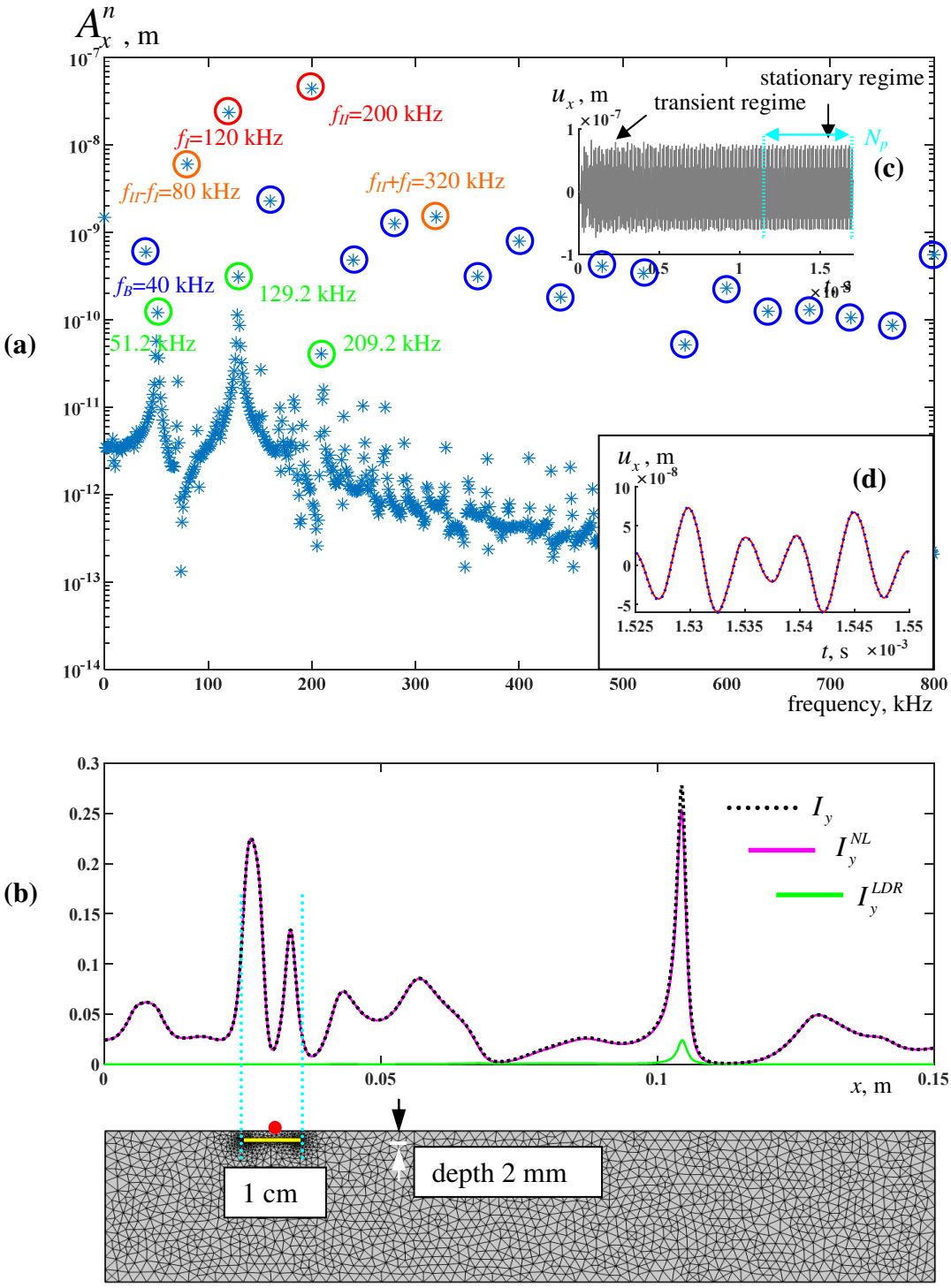

Fig. 30. Same as Fig. 22 but for the crack of 1 cm length buried at depth of 2 mm.

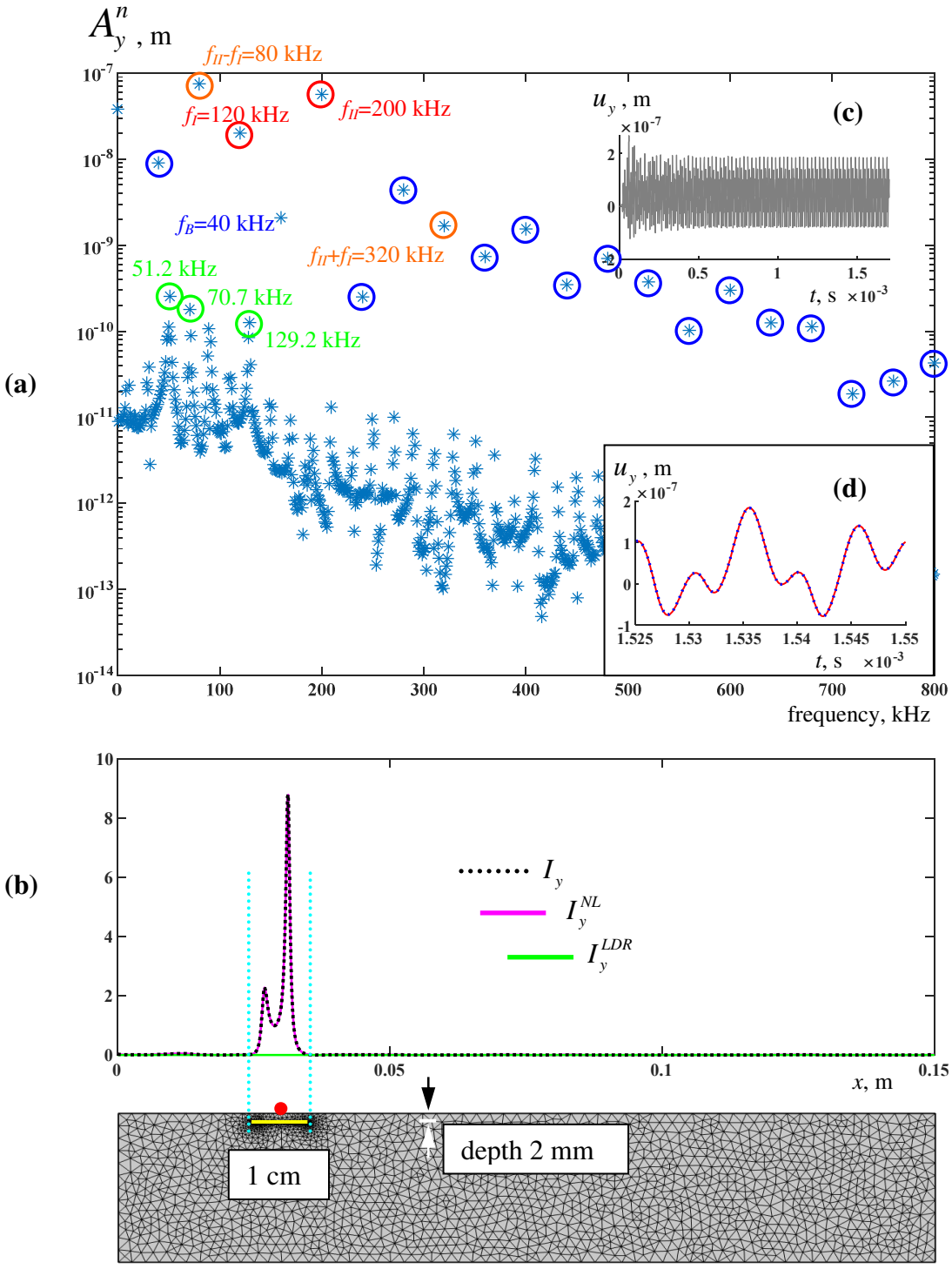

Fig. 31. Same as Fig. 30 but for the y-components.

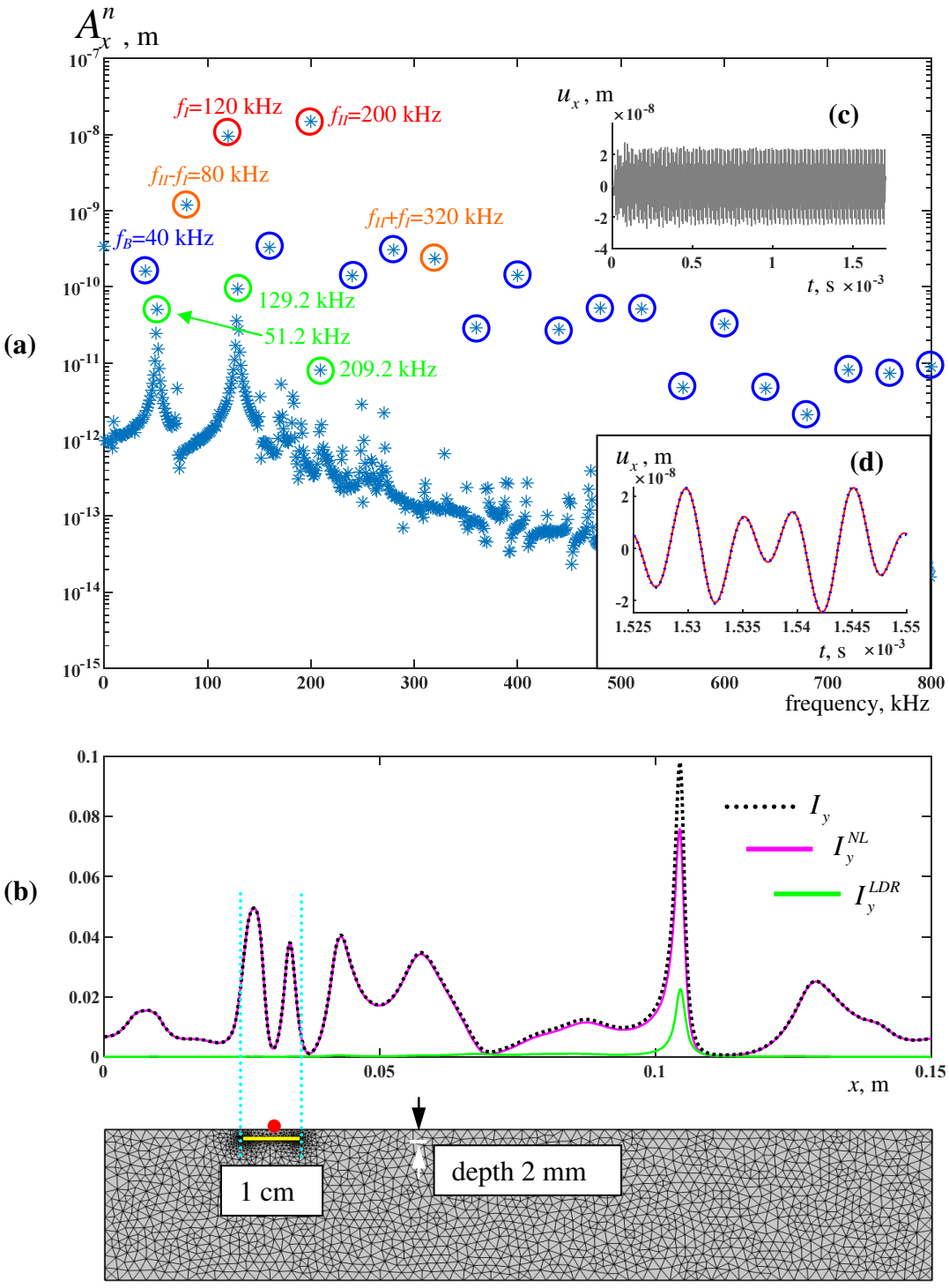

Fig. 32. Same sample geometry as in Fig. 30 but for the excitation amplitudes A_I and A_{II} both reduced in $\sqrt{10}$ times.

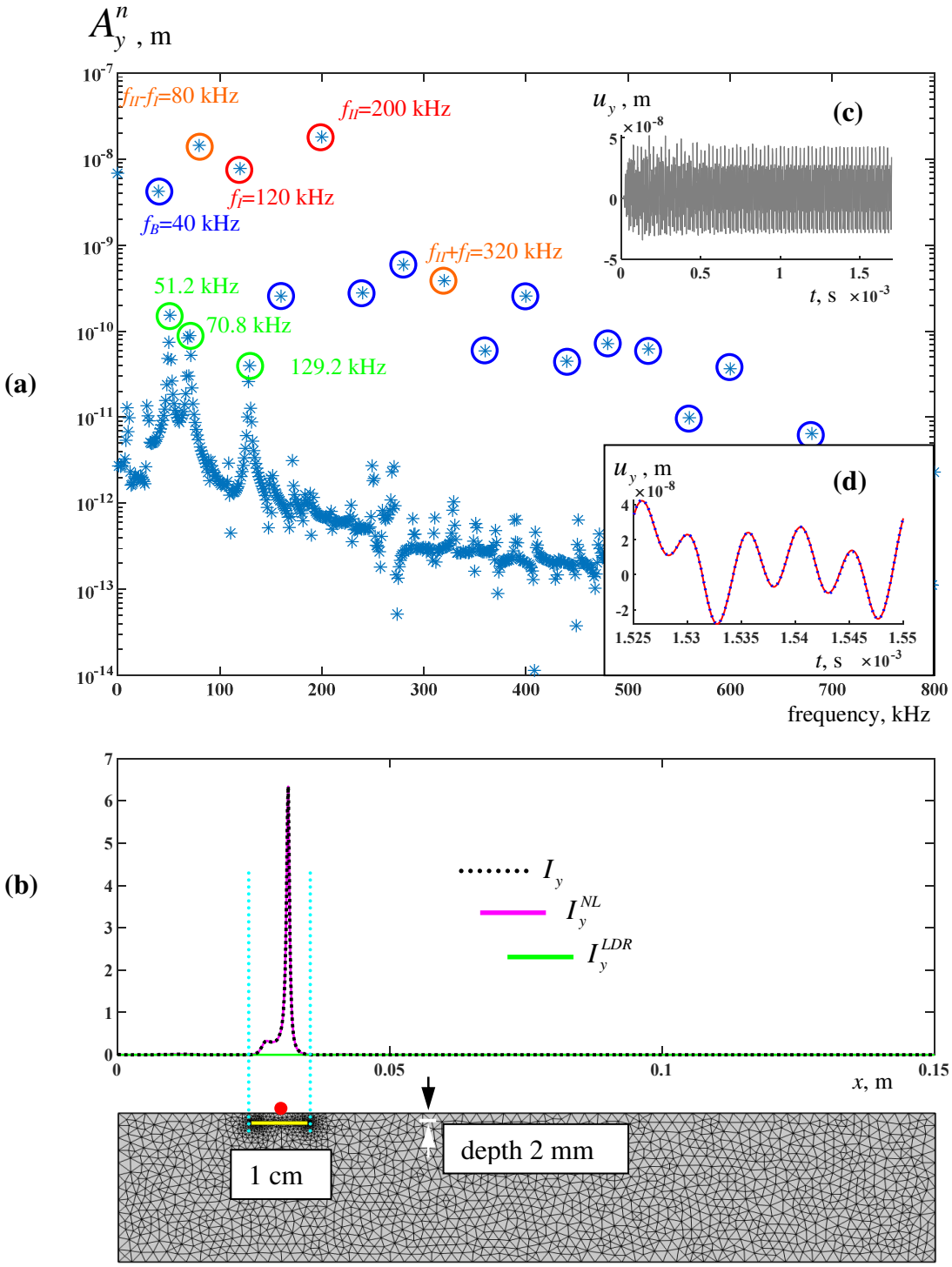

Fig. 33. Same as Fig. 32 but for the y-components.

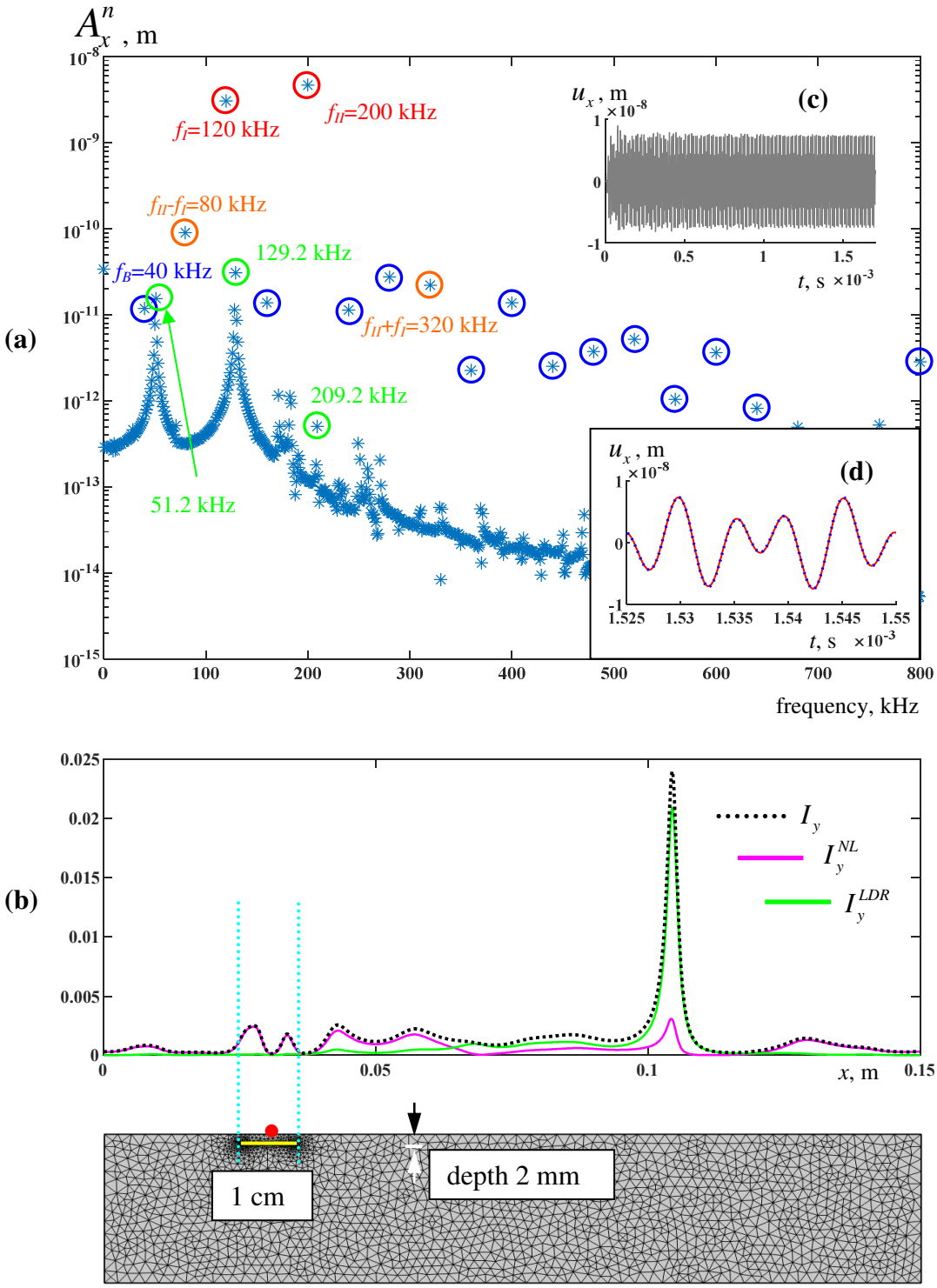

Fig. 34. Same sample geometry as in Fig. 30 but for the excitation amplitudes A_I and A_{II} both reduced in 10 times.

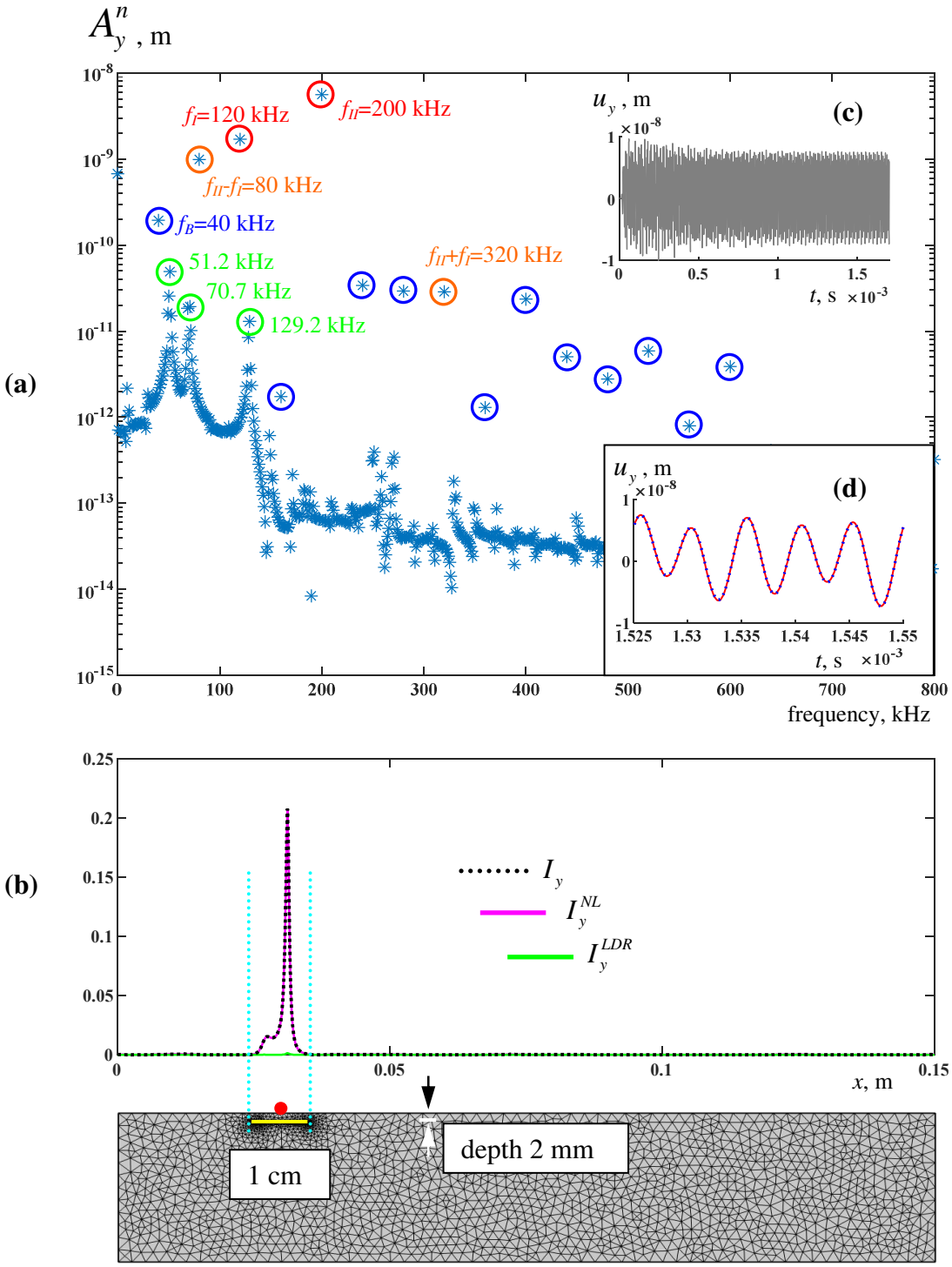

Fig. 35. Same as Fig. 34 but for the y-components.

3.2. Characterizing different types of resonances

The nature of the nonlinear resonances has to be better understood. However, it is possible to suggest some hypotheses. There exist at least two mechanisms having resonant and nonlinear properties at the same time. Firstly, a crack parallel to the surface represents a resonator of Fabry-Pérot type. Its nonlinear character follows from the fact that the crack interface is not a usual boundary of free or fixed kind, but an entity with highly nonlinear boundary conditions. Correspondingly, the resonance condition can represent a relationship analogous to the one concerning the number of half-wavelengths per distance between faces, but having an important nonlinear component. The resonance Fabry-Pérot type is essentially determined by the crack depth and not by its length.

Secondly, the crack is not just a sound reflecting inner boundary, but an interface with contact interaction. An attempt to enlarge the crack aperture results in elastic deformation of a material zone surrounding the crack. At the same time, an attempt to shrink it also produces strain in material together with activation of contact interaction at the interface. In the both cases, a kind of nonlinear restoring force appears that assumes the existence of some spring constant (or curve). Father, the strained surrounding material zone has some inertia. In this situation, it can be concluded that the crack interface has properties of nonlinear mass-spring resonator. Its resonance frequency will essentially depend on the crack length and not on its depth.

There could also be a case of a membrane resonance appearing when the layer of material located above the crack is very thin. As for the mass-spring resonator, the resonance here is also of mechanical type. However, strong dependence both on depth and size is expected in that case, since the depth determines the membrane thickness and therefore its stiffness, while the length remains an essential parameter affecting the stiffness as well. Note that a very thick membrane tends to the case of mass-string resonance.

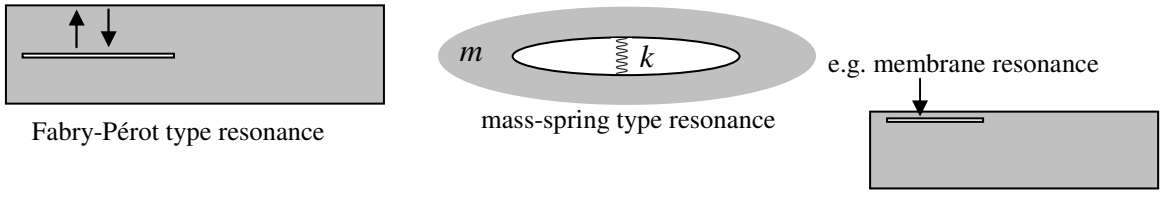

Fig. 36. Illustration for possible mechanisms of nonlinear resonances in a solid with a crack.

With this hypothesis on the resonance nature in mind, we consider a specific resonance shown in Fig. 35 at moderate excitation level corresponding to the first strain invariant of order of

$6 \cdot 10^{-7}$ near the crack. Namely, it is the resonance frequency of 51.2 kHz appearing in the A_y^n spectrum. To attribute it to a certain resonance type, we performed a series of computations for different crack lengths and constant crack depth, and then for different crack depths and constant crack length. The result is depicted at Fig. 37. It can be concluded that the resonance in Fig. 36 is of the mass-spring type. This is not surprising since the longitudinal and transverse wavelengths equal 15.5 cm and 7.8 cm for that frequency that excludes a Fabry-Pérot type resonance formation for the crack depth of several millimeters.

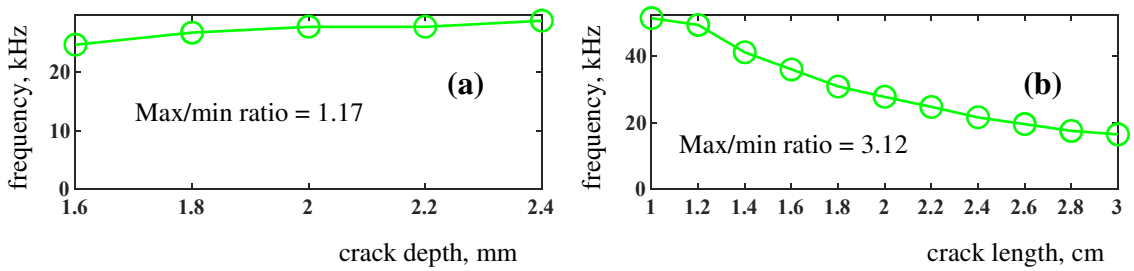

Fig. 37. The dependences of resonant frequency identified at Fig. 34 (see set (a) *showing resonance at 51.2 kHz) on crack depth and on crack length. In set* **(a)***, the crack depth varies between 1.6 and 2.4 mm at fixed crack length 2 cm. In set* **(b),** *the crack length varies between 1 and 3 cm at fixed crack depth 2 mm.*

Analysis of the resonance type can present an additional opportunity for modeling-based diagnostics. Suppose that, even with absent modeling and experiment agreement at the level of particular wave displacements, the resonance type and frequency is reproduced by the model correctly. Then, by performing the MMD-FEM modeling for different crack lengths and depths in order to match the calculated resonance frequency with the experimental one, actual crack parameters can be reconstructed in a way complementary to imaging on the basis of nonlinear criterions.

3.2. Crack images for various base frequencies

Figs. 38-43 portray a sequence of nonlinear images i.e. curves $I_{x,y}^{NL}$ and $I_{x,y}^{LDR}$, computed at the top surface. These images correspond to samples possessing designated material properties. The contrast values $C_{x,y}$ introduced in Section 2.1 are calculated for the total criterion $I_{x,y} = I_{x,y}^{NL} + I_{x,y}^{LDR}$. The main distinguishing features of the imaging procedure are represented by the contrast in values: a high value signifies a successful imaging outcome, a medium value indicates a situation that is unclear, and a low value denotes a failure.

As depicted in Figs. 38-43, the contrast illustrates the interpretation of imaging procedure success in the following manner:

- Elevated C_y values signify accurate reconstruction of both the position and extent of damage, characterized by weak or nonexistent parasite peaks in the undamaged zone (as observed in images for f_B=30 kHz for 3 cm crack length). However, some instances with relatively lower C_x values compared to C_y raise uncertainties regarding the efficacy of the imaging procedure.
- Intermediate $C_{x,y}$ values suggest accurate reconstruction of both damage position and extent, accompanied by faint or non-existent parasite peaks within the undamaged zone (illustrated, for instance, in images corresponding to f_B=60 kHz, f_B=70 kHz and f_B=80 kHz for 3 cm crack length).
- Contrasts measuring approximately 10 or below indicate a situation that is less clear. This scenario might involve the presence of multiple peaks, with one being accurate and the others being parasitic - meaning they are situated at incorrect positions, etc. The accurate peak might yield moderate $C_{x,y}$ values, but the existence of the incorrect one usually signifies limited success in imaging effectiveness (as observed, for instance, at f_B=90 kHz for 3 cm crack length and f_B=30 kHz for 2 cm crack length)

As we have seen before for imaging based on harmonic generation, the structure of the nonlinear acoustic field is not necessarily concentrated near the crack. This is additionally illustrated by the nonlinear criterion $I_{x,y}^{NL}$ calculated in the entire 2D domain. Depending on the damage parameters and the excitation frequencies, the $I_{x,y}^{NL}$ distribution can have a clear maximum around the crack, as in Fig. 39 for I_x^{NL} at f_B=60 kHz, or it can be completely smeared, as in Fig. 42 for I_x^{NL} at f_B=80 kHz. Multiple parasite extrema can also appear in the calculation domain as in Fig. 41 for I_x^{NL} at f_b=40 kHz. Note that 2D images for the nonlinear criterions are not available experimentally; this is a point when numerical simulations can be of use.

In many cases, such as all instances in Fig. 39, I_y at f_B=70 and 80 kHz, etc, strong nonlinear resonances are present. They can tremendously increase the image contrast in comparison with the nonlinear criterion (see, for instance, C_y at f_B=50 kHz in Fig. 38), but does not change the situation when damage detection is unsuccessful (I_x at f_B=40 kHz in Fig. 38). They can also enhance parasite extrema as in the case illustrated in Fig. 42 with I_x at f_B=80 kHz.

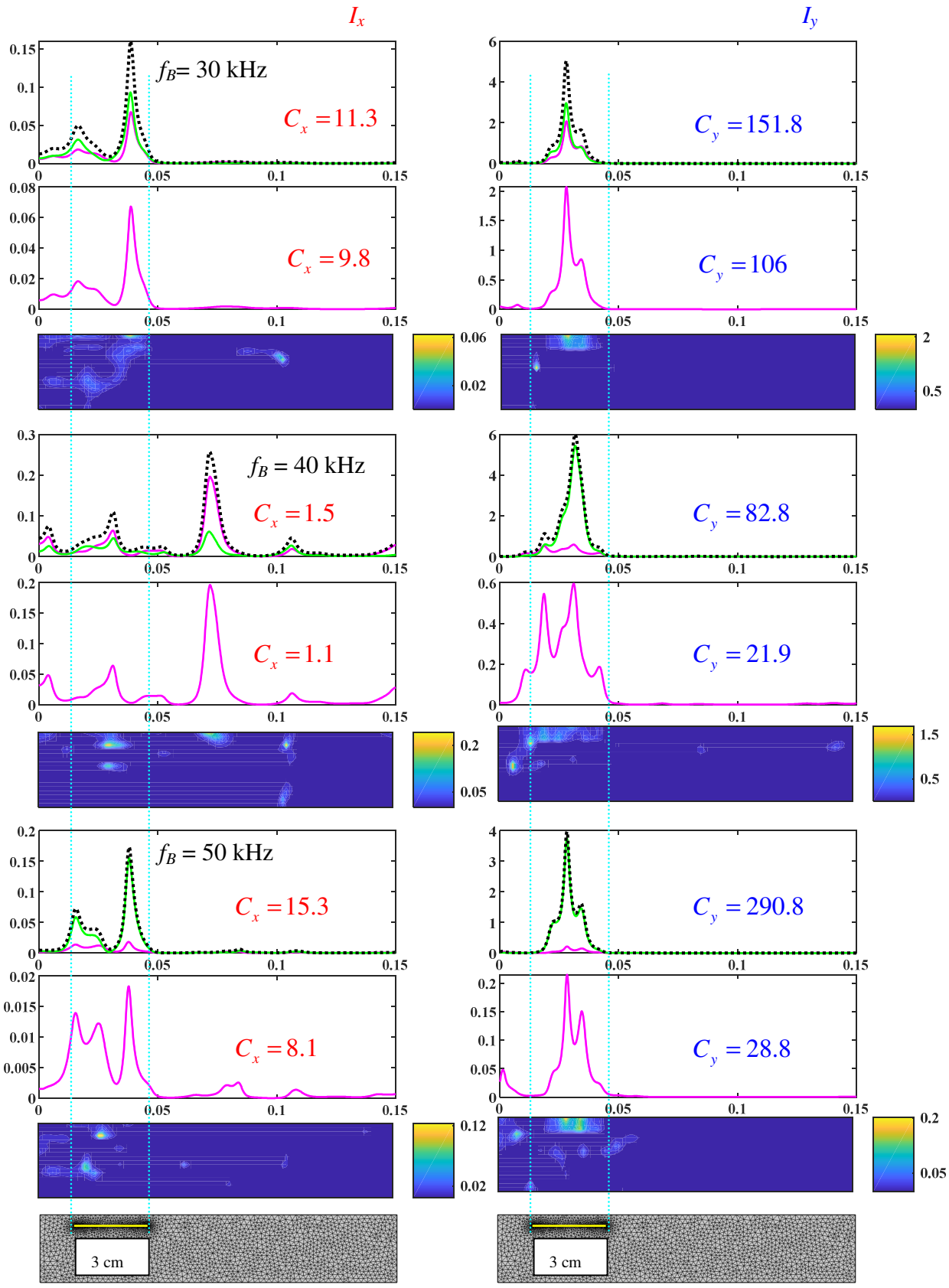

Fig. 38. Nonlinear images $I_{x,y}^{NL}, I_{x,y}^{LDR}$ *calculated accordingly to Eqs. (5)-(6) (pink and green lines) together with their sum* $I_{x,y}$ *(black dotted line) at the top surface of sample with 3 cm crack. Images* $I_{x,y}^{NL}$ *are also presented alone both at the top surface and in the entire calculation domain.*

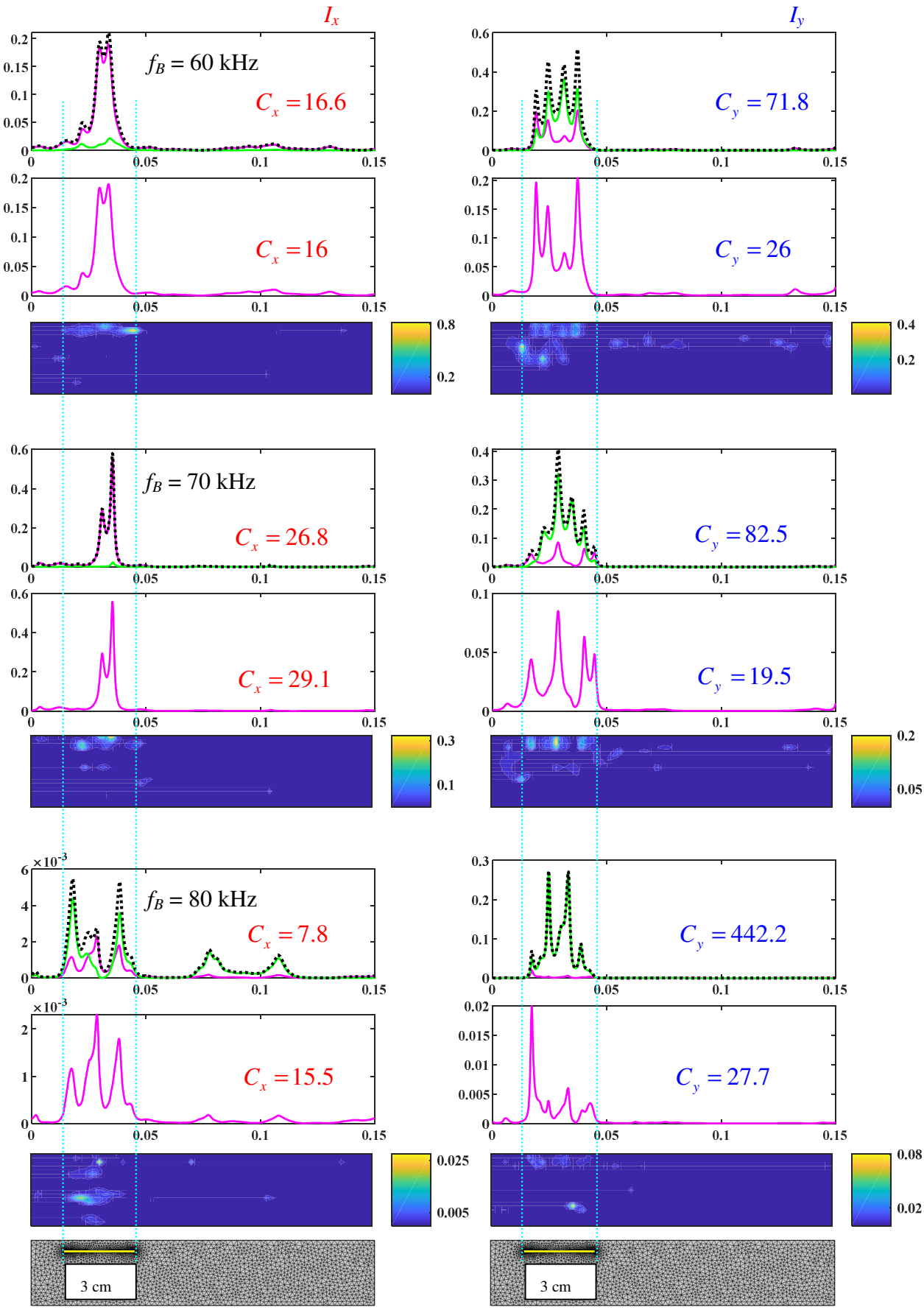

Fig. 39. Same as Fig. 38 but for a frequency ranging from 60 to 80 kHz.

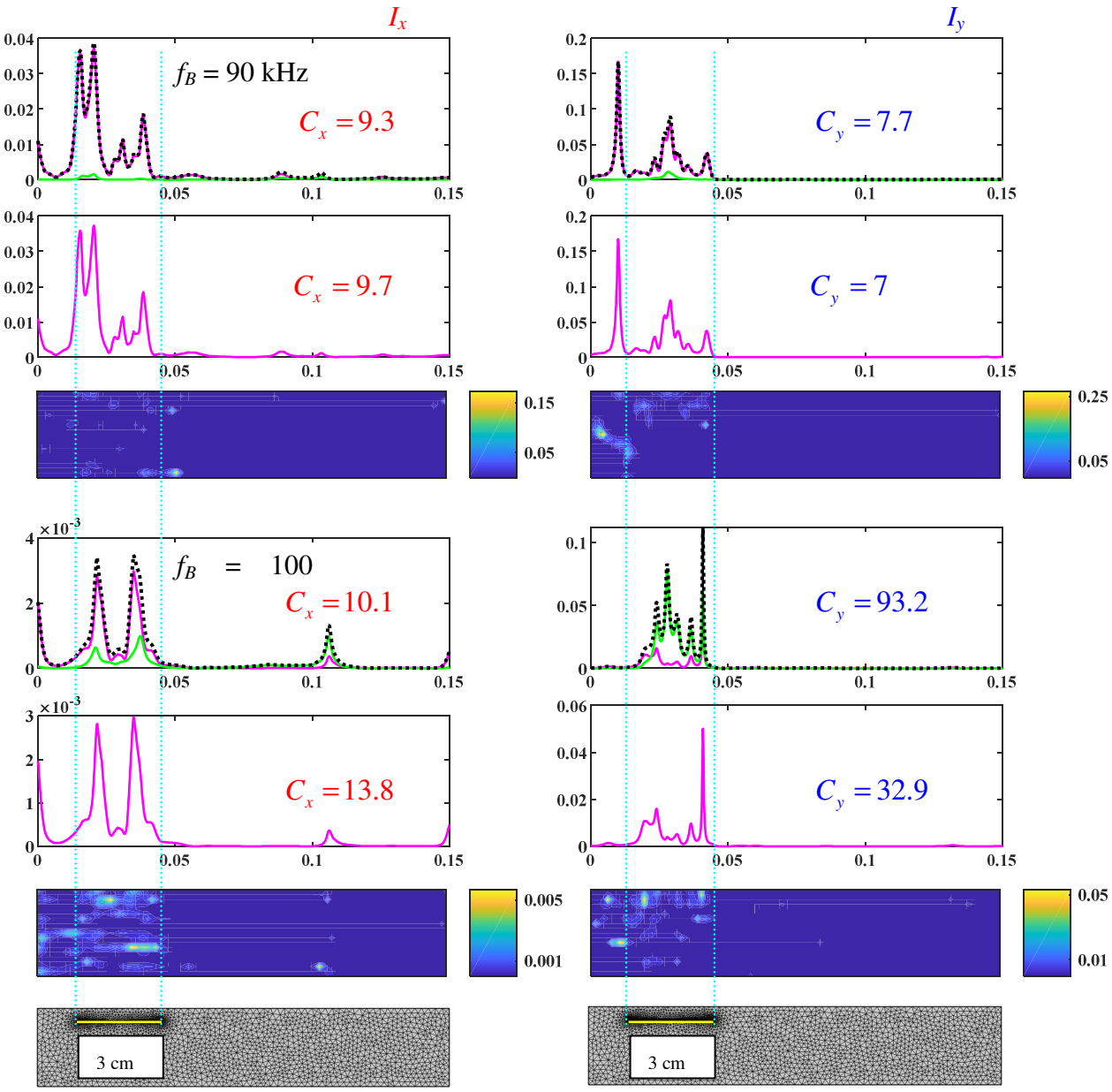

Fig. 40. Same as Fig. 38 but for a frequency ranging from 90 to 100 kHz.

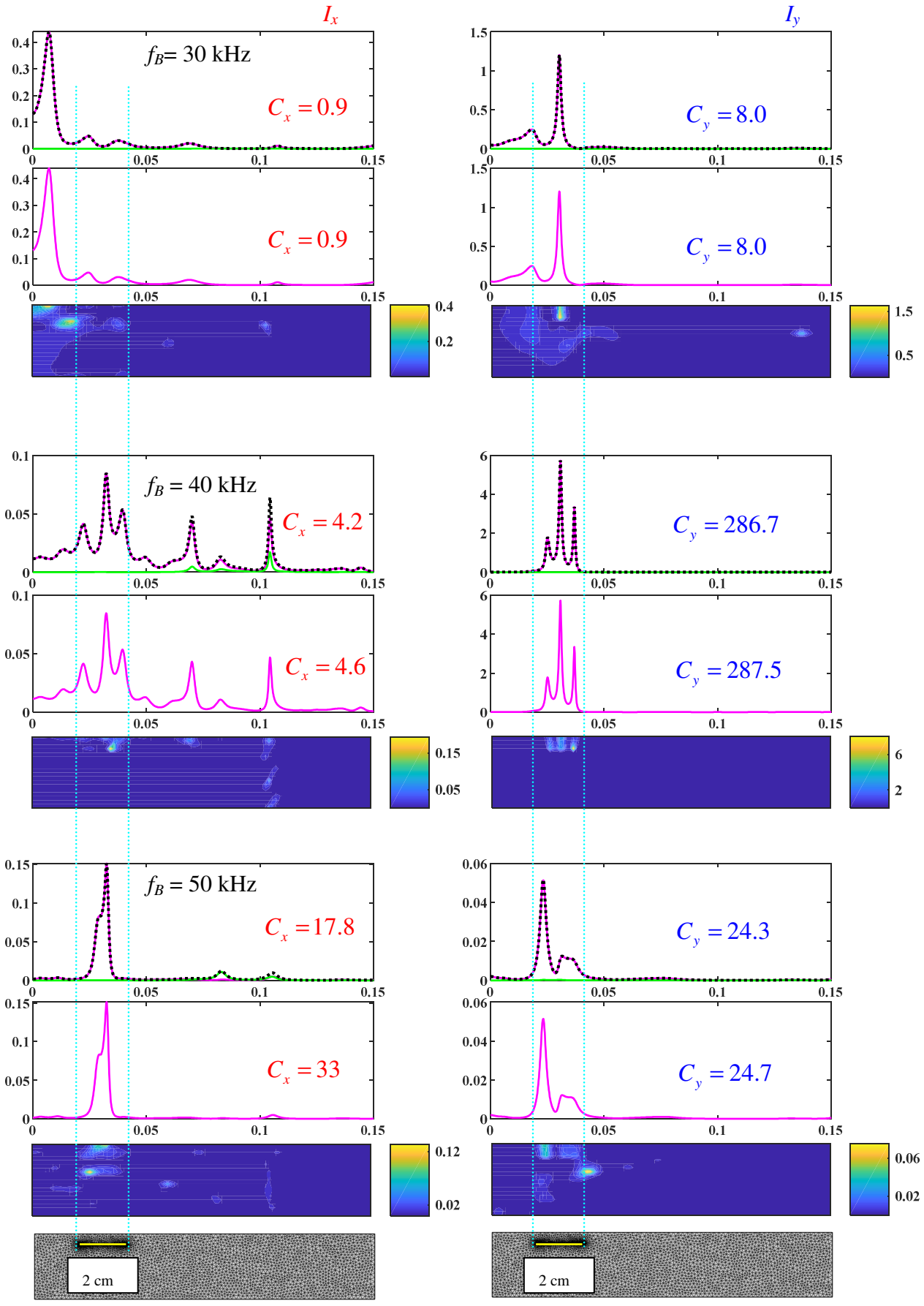

Fig. 41. Same as Fig. 38 but for the crack of 2 cm length

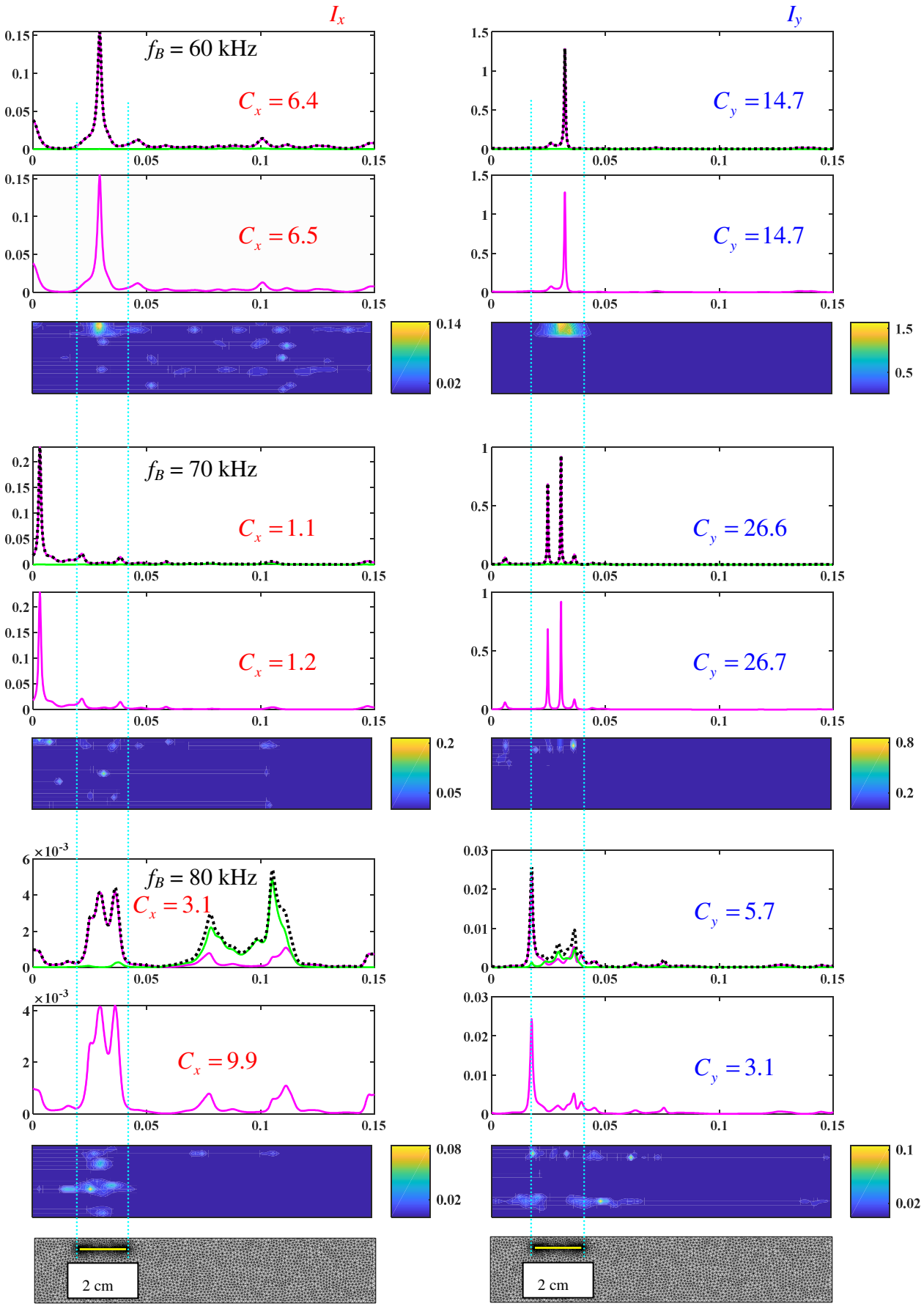

Fig. 42. Same as Fig. 39 but for the crack of 2 cm length.

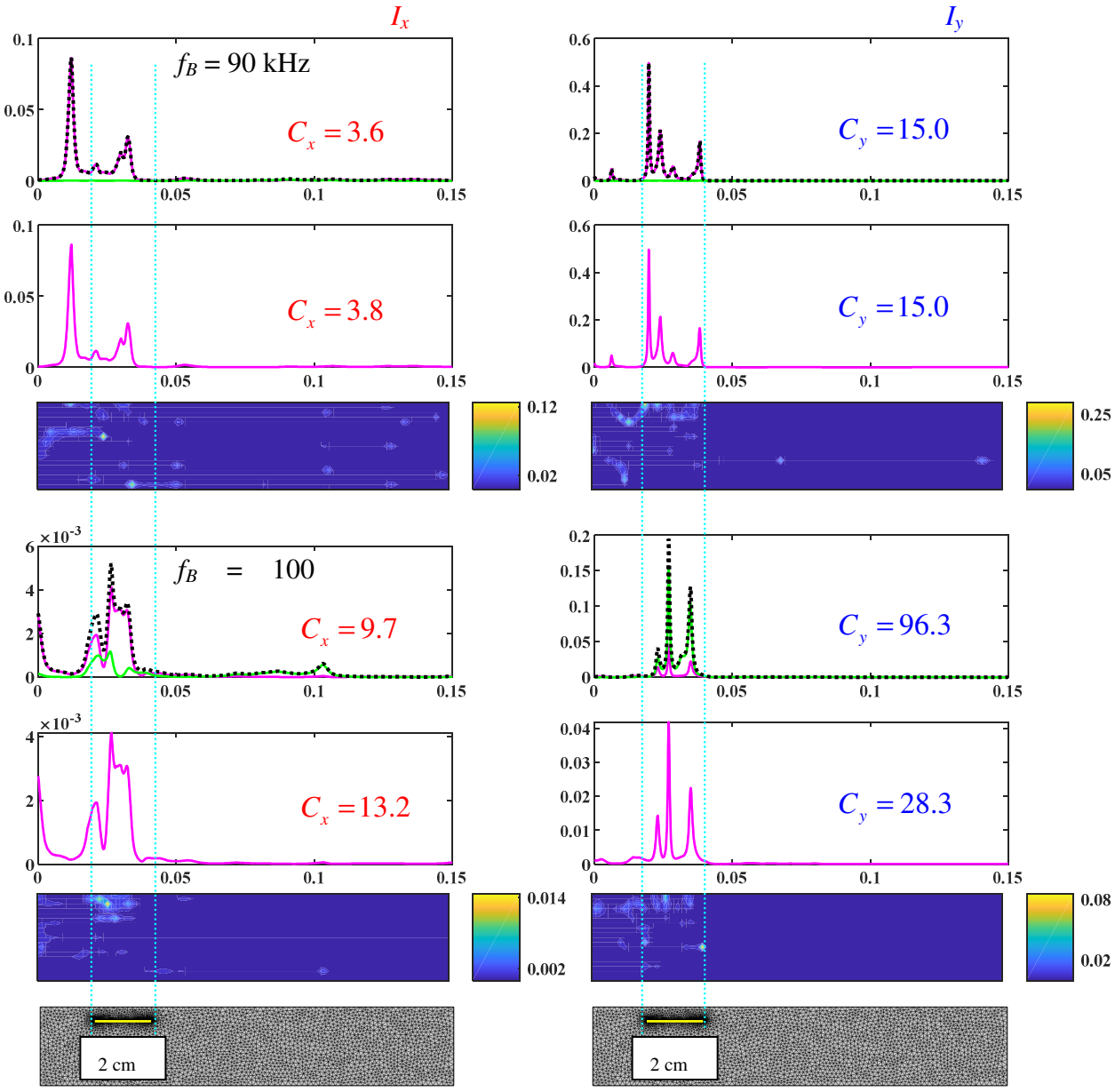

Fig. 43. Same as Fig. 40 but for the crack of 2 cm length.

3.3. Conclusions

The two-frequency mixing process with parameters considered here generate strong sum and difference harmonics, as well as proper nonlinear vibrations in many cases, producing very high values of the nonlinear criterion $I_{x,y}$ defined on the basis of all harmonics which are not present in the excitation signal. In some situations, the nonlinear resonant vibrations dominate and become comparable with the excitation amplitudes in the spectrum. This behavior can be seen as a typical feature of extremely nonlinear barely open cracks (with no prestress).

Generally, the use of the frequency mixing process results in a clear high-contrast detection of at least of relatively large cracks, as considered here. In addition, a hypothesis on the nature of nonlinear resonances, once validated, can help detect crack depth or length separately.

Chapter IV: Qualitative comparison of model and experiment

Geometry and model parameters considered in the previous Chapter were most "comfortable" from the point of modeling, meaning that their choice was in the sake of geometric simplicity and reasonable computation time. Here our task is to gradually modify geometric parameters in order to get closer to a real case for which experimental vibrometry data are available. The resemblance is not, however, complete, since our MMD-FEM modeling is limited to a 2D situation in the framework in this thesis, whereas real samples are three-dimensional. In what follows we will show a series of modeling results that will progressively tend to the experimental conditions at least at the level of sample sizes. Despite the gap between experimental and modeling situations remains, it is possible to establish a qualitative agreement between synthetic and real images of damage.

1. Available experiment on laser Doppler vibrometry

In this section, we followed findings on delamination detection in composites through local defect resonance done by Segers **[Seg-20]**. His research work contributed to non-destructive testing by extending the capabilities of methods that use the local defect resonance (LDR) phenomenon, which enable precise visualization of cracks and delaminations in materials at moderate acoustic excitation levels.

As the author explained in his article **[Seg-20]**, a delamination in carbon fiber reinforced polymer sample generates acoustic nonlinearity. The excitation at the LDR frequency allows one to focus the acoustic energy near the defect i.e. to activate it in a most efficient way. Then, standing waves generated in the sample via a continuous sinewave source excite higher harmonics that can be detected from shallower and deeper side of the sample. In this thesis, we used a similar methodology that makes it possible to compare experimental and modeling results at least in the qualitative manner. Unfortunately, quantitative comparison is still not possible due to significant differences in sample geometry and material parameters.

The experiment has been performed on a sample with dimensions of 290x140x2.2 mm^3 having a delamination of 20x20 mm^2 in size. This delamination is created by putting metal foil of a 25 μm thickness in between plies. An LDR frequency in such a system was found to be 27 kHz; this was the frequency of the continuous sinewave excitation in the imaging experiments **[Seg-20]**. Of course, due to differences in parameters this frequency does not

correspond to the LDR in our modeling case. However, for qualitative comparison, we cite here the results of the imaging procedure (Fig. 1)

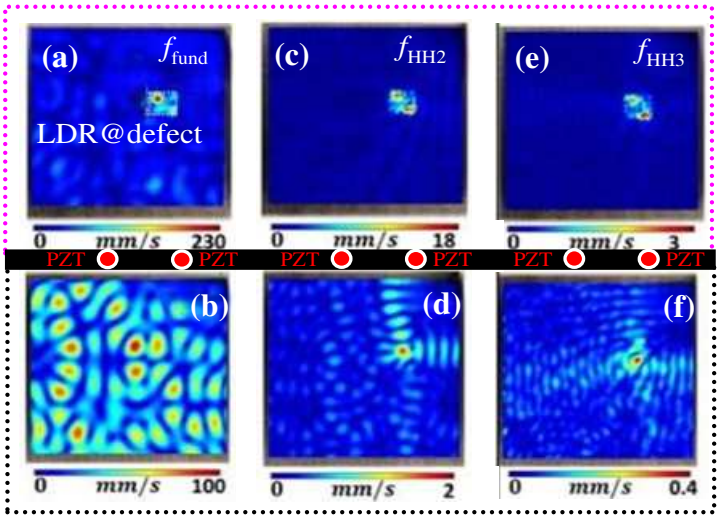

Fig. 1. Observations from experiments on particle velocity patterns **(a)**-**(f)** *made at the fundamental excitation frequency f_{fund} as well as at the second (f_{HH2}) and third (f_{HH3}) harmonic frequencies. The images are taken on the shallow and deep plate sides relative to the delamination position* **[Seg-20]**.

As it can be seen from Fig.1, the delamination, when subjected to harmonic excitation at the LDR frequency, can be detected from both side of the sample via the harmonics imaging.

During this PhD research I got an opportunity to collaborate with the NDT & SHM laboratory at Ghent University. The goal of this collaboration was not to present new experimental results but to gain exposure to experiments. Getting proficiency in applying established methodologies, specifically the scanning laser Doppler vibrometer (SLDV) measurement techniques detailed in **[Seg-21]**, forms a crucial foundation. This contributes to better understanding of future simulations.

The use of images from **[Seg-20]** ensures transparency, contributing insights without introducing new experimental results. Using the same setup used by J. Segers in his research (**[Seg-20], [Seg-21]**) for laser Doppler vibrometry, we present the experiment details:

- A sample of composite fiber reinforce polymer CFRP used with a delamination.
- For inducing vibrations, two low-power piezoelectric actuators (EPZ-20MS64W Ekulit) are affixed to the deep side surface using phenyl salicylate adhesive. Throughout the experiments, both actuators receive identical signals.
- Amplification of the voltage supplied to the actuators is achieved using a Falco Systems wma-300 voltage amplifier.

- The 3D infrared scanning laser Doppler vibrometer from Polytec (PSV-500-3D-Xtra) is utilized to capture full-field surface vibrations.
- In this investigation, only the out-of-plane velocity component V_Z is considered. Vibrations are measured from both the shallow side and the deep side.

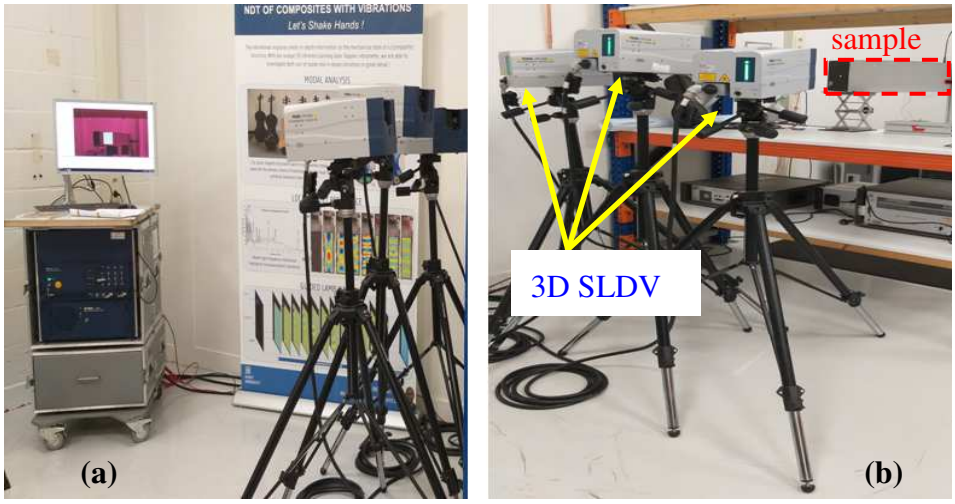

Fig. 2. Experimental setup **(a)** *SLDV control unit* **(b)** *Visualization of a test specimen positioned in front of a 3D scanning laser Doppler vibrometer setup.*

Fig. 2. illustrates the arrangement for scanning a delaminated sample with 3D scanning laser Doppler vibrometer. With this initial overview of the experiment, our understanding was significantly enhanced, aiding us in the development of a more realistic geometry during our modeling process. Additionally, Segers's research findings served as a foundation, prompting us to transition from comfortable conditions to a more realistic representation, as detailed in the following section of this chapter.

2. MMD-FEM simulations in conditions closer to the experiment

In this Section we describe a set of modeling results obtained in conditions progressively approaching the real experimental situation discussed in Section 1. It is important to mention that there is still a gap in parameters and conditions between theory and experiment. The primary difference is in the number of dimensions: the simulations are in 2D due to high computational expenses related to the stationary wave formation, although a 3D code has already been developed **[Ale-19]**. Another feature is that the experimental methodology use the LDR concept i.e. the excitation frequency is specially adjusted to excite the defect is a most optimal way. In contrast, in our modeling we do not try to optimize the excitation in terms of frequency because of time-domain nature of our calculations and their computation cost. Anyway, in 2D and in 3D the LDR frequencies are different that does not allow to compare the results directly in the quantitative manner. However, we gradually modify

sample length and thickness in order to make them more realistic. In addition, we consider an effect of distance between the transducer and the crack on the image quality.

2.1. Geometry and parameters

To imitate a configuration similar to the experiment, we consider a fragment of a much thinner plate of 3 mm and, later, of 2 mm thickness, add again the low-reflecting boundary conditions at the left and right edges, and drop the assumption of fixed low boundary (see Fig. 3). The center C_{cr} of a crack of fixed size L_{cr}=3 mm is located at 3 mm from the left edge.

To start with, we keep same values of elastic properties and the roughness-related coefficient C as in the previous numerical tests: the Young's modulus $E = 7 \cdot 10^{10}\ Pa$, Poisson's ratio ν = 0.33, density of 2700 kg/m³, and roughness-related coefficient $C = 10^{10}\ Pa^{1/2} m^{-1}$. However, ten times decrease in all sample dimensions make it possible to use more realistic values of bulk and shear viscous damping coefficients, $\eta_b = 16.7\ Pa \cdot s$, $\eta_v = 6\ Pa \cdot s$, while keeping the same rate of transient process decay measured in excitation periods. In this situation, the transducer generates Lamb waves in the presence of attenuation.

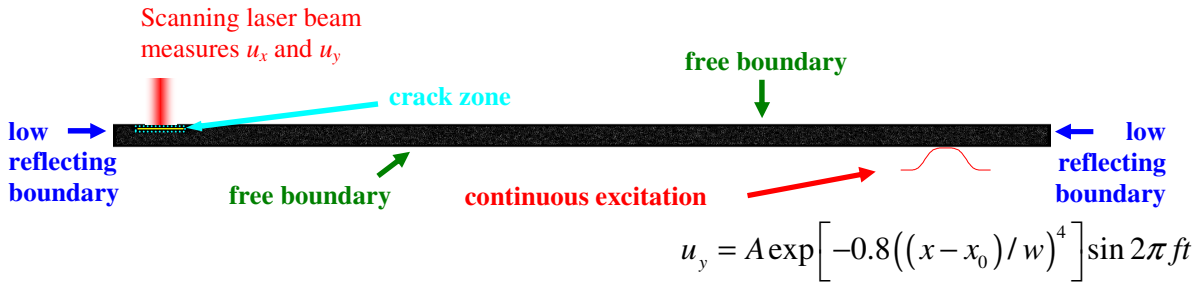

Fig. 3. Sample of 60x2 mm² dimensions containing a crack. Free boundaries are indicated together with a zone of continuous excitation (amplitude A and frequency f) by vertical displacement u_y. The excitation zone (transducer) has the length 2w and is centered at x_0.

2.2. Simulated nonlinear images

Based on the previous study presented in Chapter III with a substantial sample size, this study aims to optimize geometry and frequency settings to achieve qualitative validation, aligning with real experimental samples. To accomplish this, a series of computational results are presented to streamline experimental parameters. Following the methodology outlined in Section 2.1 of Chapter III for computing the nonlinear criterion $I_{x,y}$, and contrast $C_{x,y}$, Fig. 4 depicts a set of damage images "scanned" on the x-coordinate at the upper surface.As before, the excitation amplitude is maintained at a level that sustains a potent yet typical acoustic

strain $\varepsilon_{cra} \sim 10^{-6}$ value in the proximity of the crack. In what follows, we keep the same amplitude A of vertical displacement.

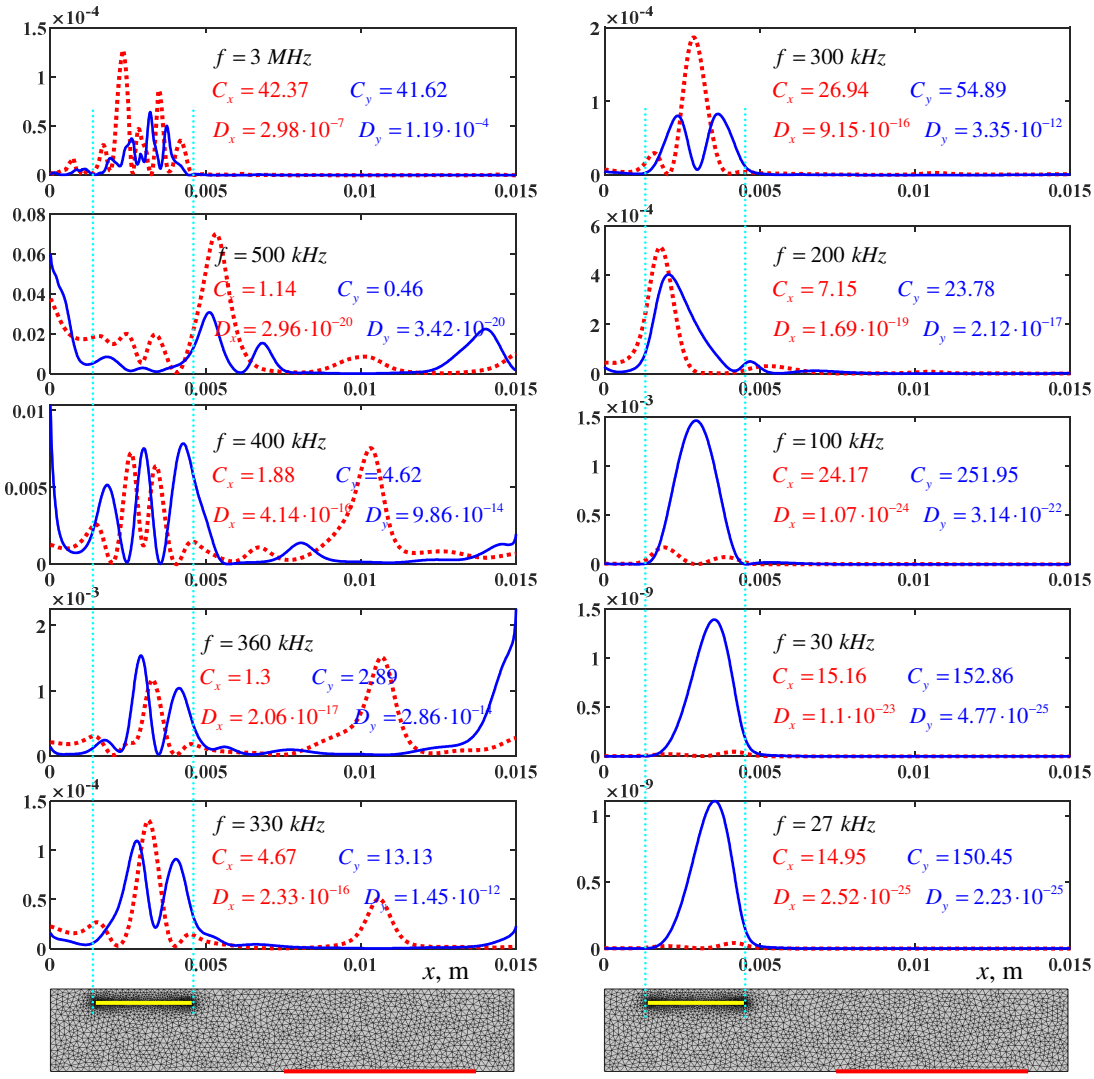

Fig. 4. Nonlinear images of damage calculated in accordance to Eq. (2) of Chapter III at the top surface of samples (3x60mm) with 3 mm crack buried at 0.5 mm excited by a continuous harmonic wave of a frequency ranging from 27 kHz to 3 MHz via a transducer depicted as a red line.

The results depicted in Fig. 4 reveal that the success of detection, characterized by C_x or C_y attaining values of 10^1, 10^2 or higher, exhibits a strong dependence on frequency. Notably, our examples demonstrate that certain frequencies, such as 100 kHz, facilitate successful imaging for the considered crack size. The choice of frequencies up to 3 MHz is due to the previous experience (Section 2 of Chapter III, larger sample) when f=300 kHz was found optimal (remember of 10 times scaling). At the same time, the low value of f=27 kHz corresponds to the experimentally established LDR frequency. Certainly, due to the difference in geometry and parameters this optimum frequency will not hold in the numerical case, but such a radical decrease in frequency would be of interest to consider. Indeed, even for such

low frequencies corresponding to long wavelengths of 23 cm (longitudinal) and of 12 cm (transverse), the successful detection is still possible. Note that 10-times scaling with respect to the previous case do not provide the exactly same results since we have modified the boundary condition at the bottom surface. Generally, for frequencies between 27 kHz and 100 kHz a reliable detection is possible.

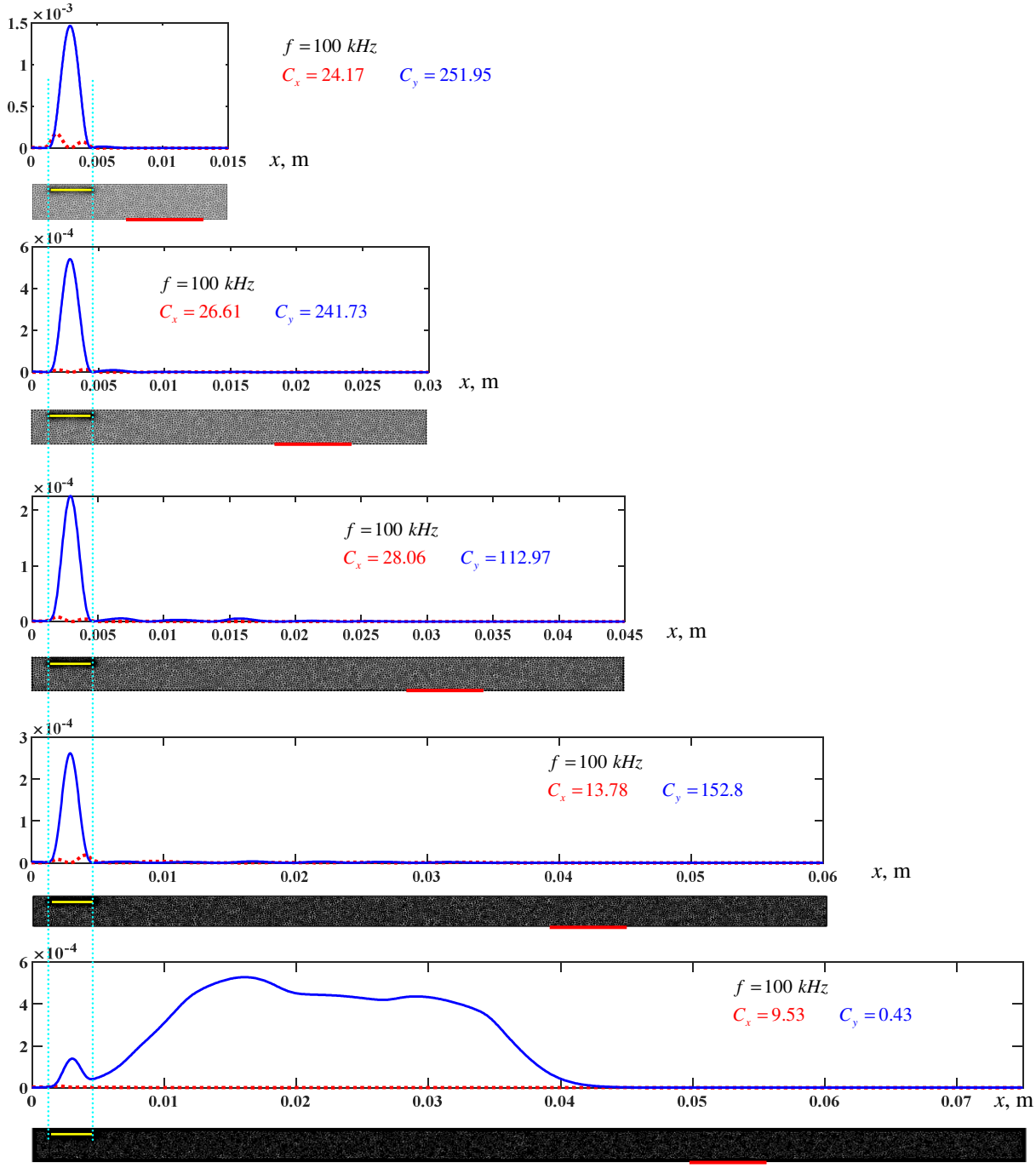

Fig. 5. Nonlinear imaging: effect of sample length variation on detecting a 3 mm-long crack buried at 0.5mm depth, excited by a continuous wave of 100 kHz frequency. Note that the excitation zone shifts following the extension in size.

Fig. 5 illustrates the effect of sample size and the distance between the transducer and the crack on the detection success. It is curious that the clear detection is possible once the distance does not exceed a value of about 4 cm and fails at distances of about 5 cm. The effect should be related not only to attenuation but also to features of nonlinear stationary waves emitted by the crack. At the same time, we remark that MDD-FEM modeling still accepts a relatively high aspect ratio of the sample that equals 20 (3x60 mm²) for this specific frequency.

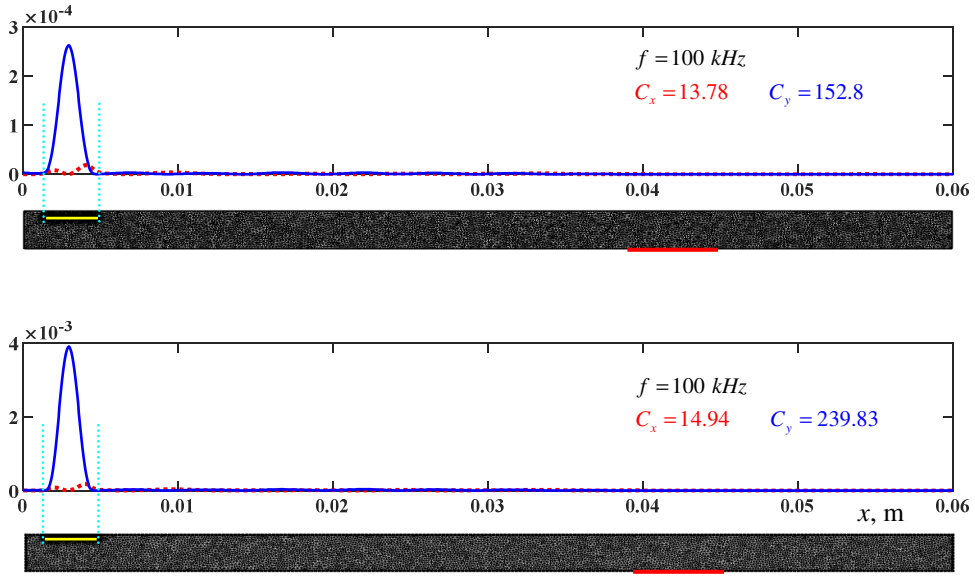

Fig.6. Nonlinear imaging of a 3 mm-long crack buried at depths of 0.5 mm (top) and 0.25 mm (bottom).

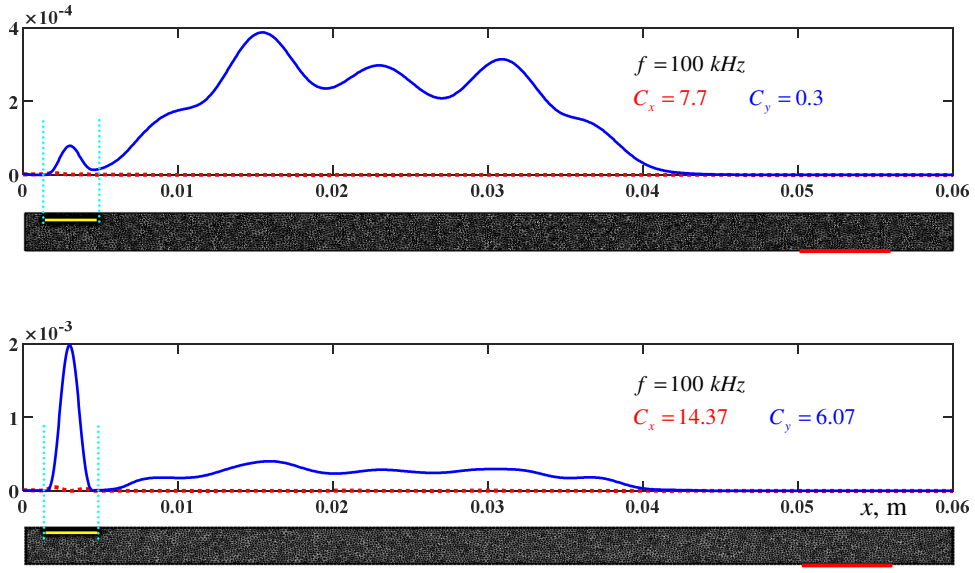

Fig. 7. Similar to Fig. 6, but with the excitation source positioned at a considerable distance.

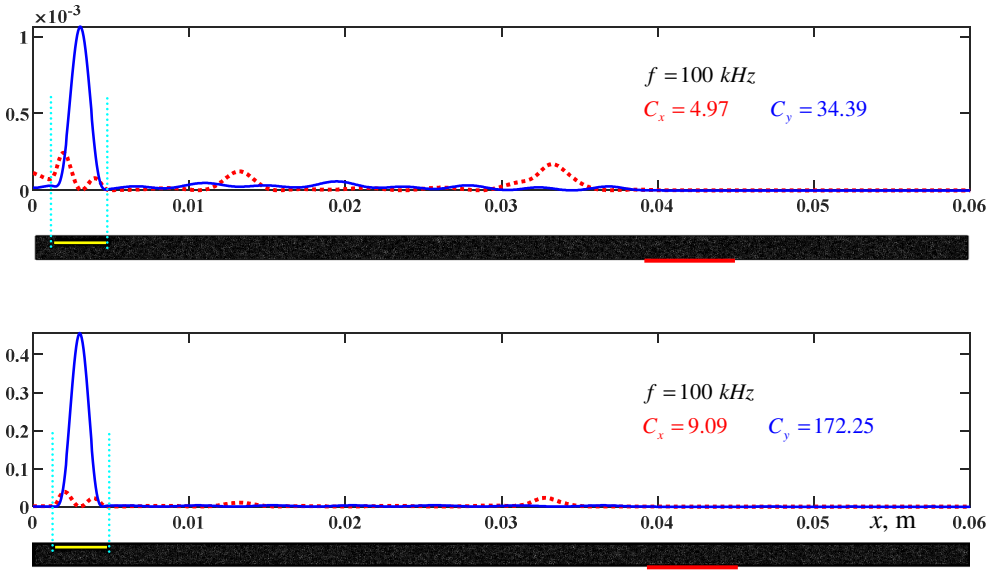

Fig. 8. Nonlinear imaging of 3 mm-long cracks buried at 0.5 mm (top) and at 0.25 mm (bottom) in the sample of 2mm thickness. The distance between the transducer and the crack is about 4 cm.

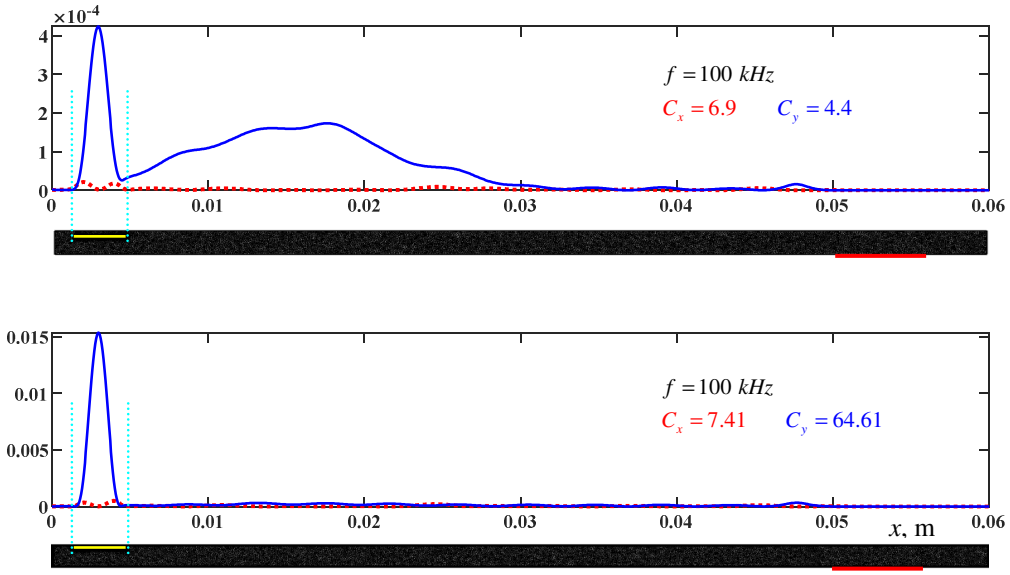

Fig. 9. Similar to Fig. 8, but with the excitation source positioned at a considerable distance.

The revealed particular threshold effect deserves more attention. Maintaining the sample size, subsequent investigations focused on varying crack depths and experimenting with an excitation source positioned at a considerable distance. In Fig. 6 we see that at a shorter distance of 4 cm a shallow (0.5 mm depth) and a very shallow (0.25 mm depth) crack are equally detected, whereas in Fig. 7, at longer distance, only a very shallow crack is seen. Such examples illustrate a combined effect of various factors influencing the imaging success; "worsening" one of them can be compensated by a favorable change in another one. Of

course, such dependences are also affected by features of the nonlinear stationary wave patterns, as it was frequently seen before.

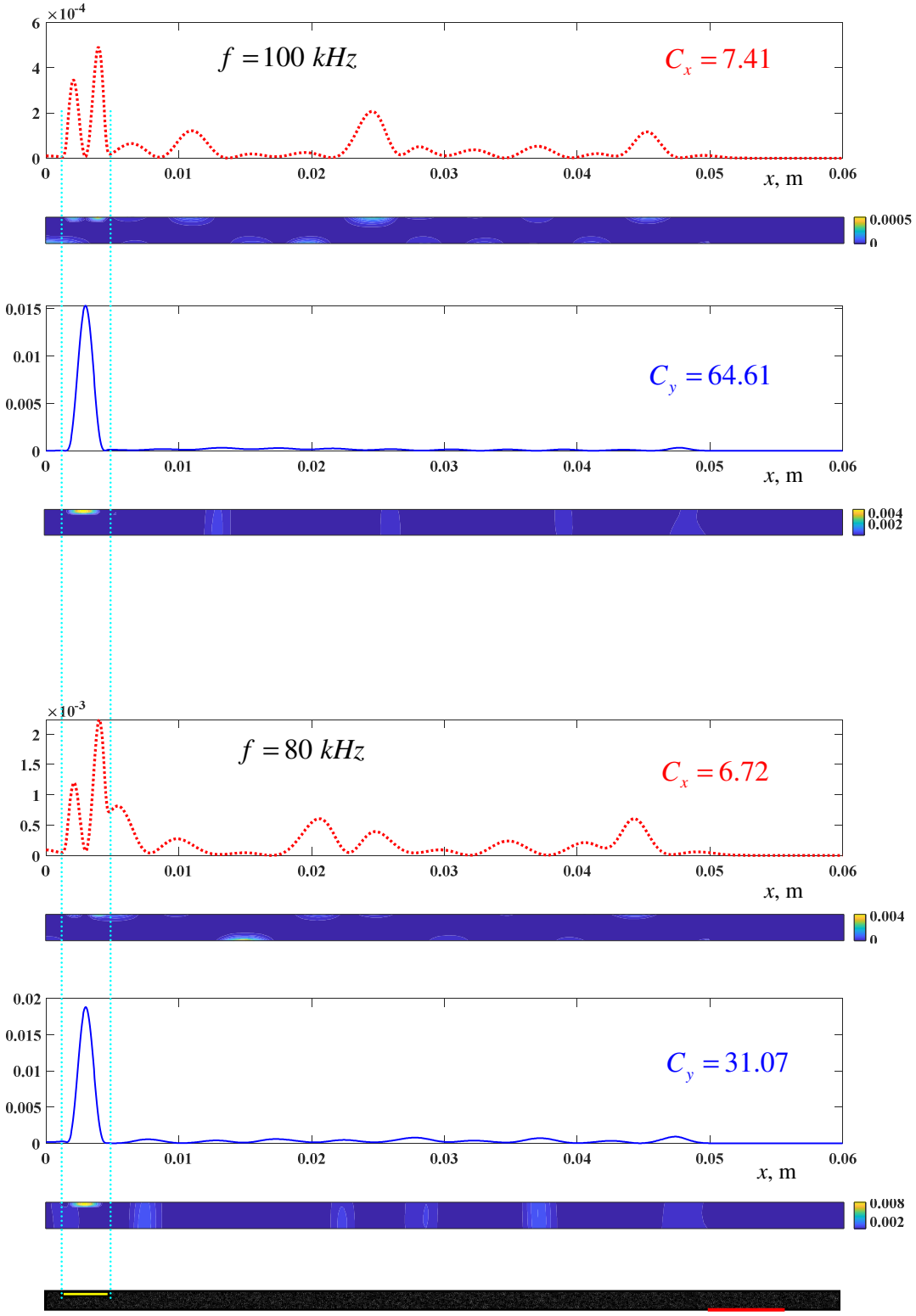

Fig. 10. Same geometry as in Fig. 9 for a shallow crack (at the bottom), nonlinear images presented at the top surface and in the entire calculation domain at frequencies f=100 and 80 kHz.

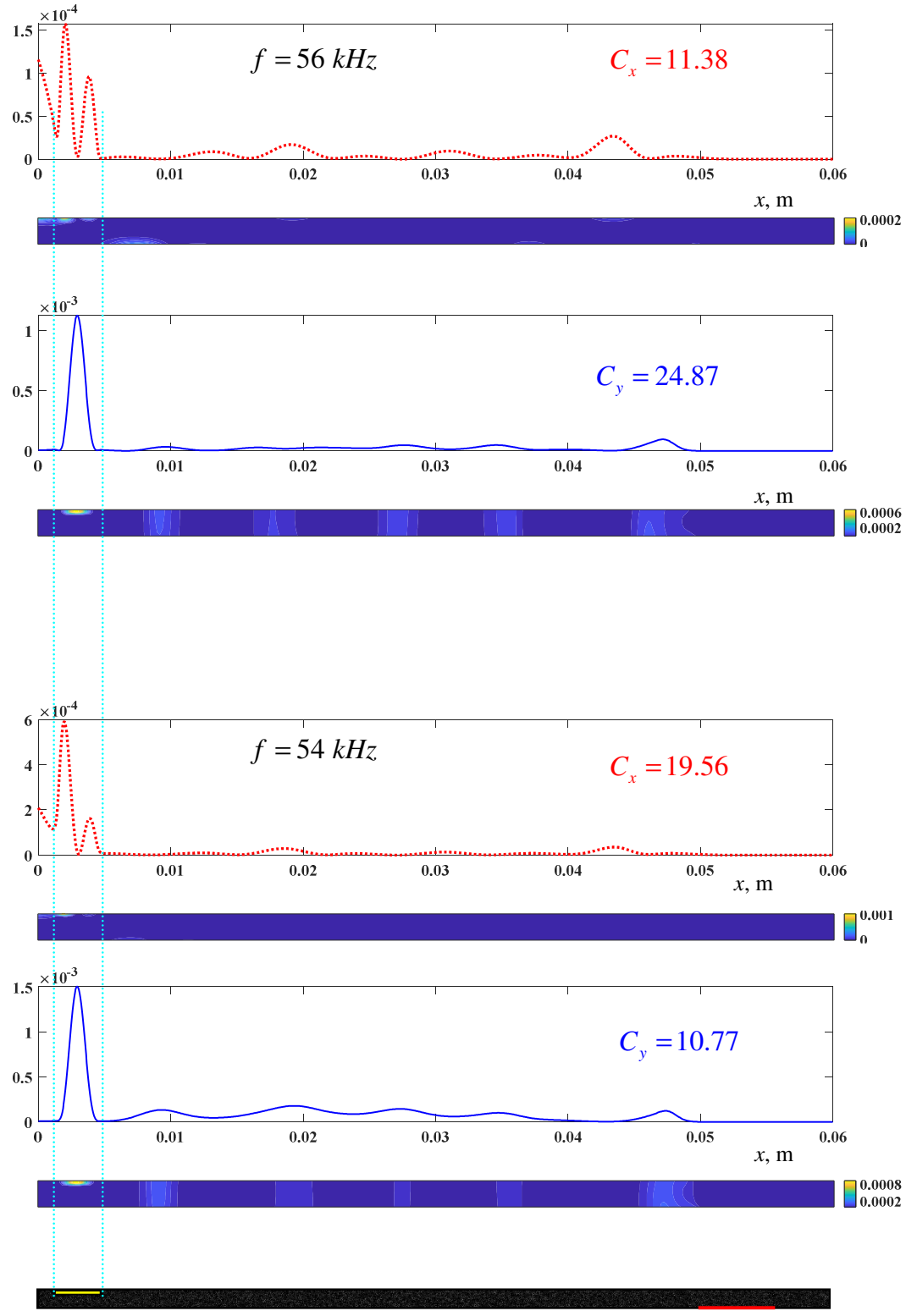

Fig. 11. Same as Fig. 10 but for the excitation frequency 56 kHz and 54 kHz.

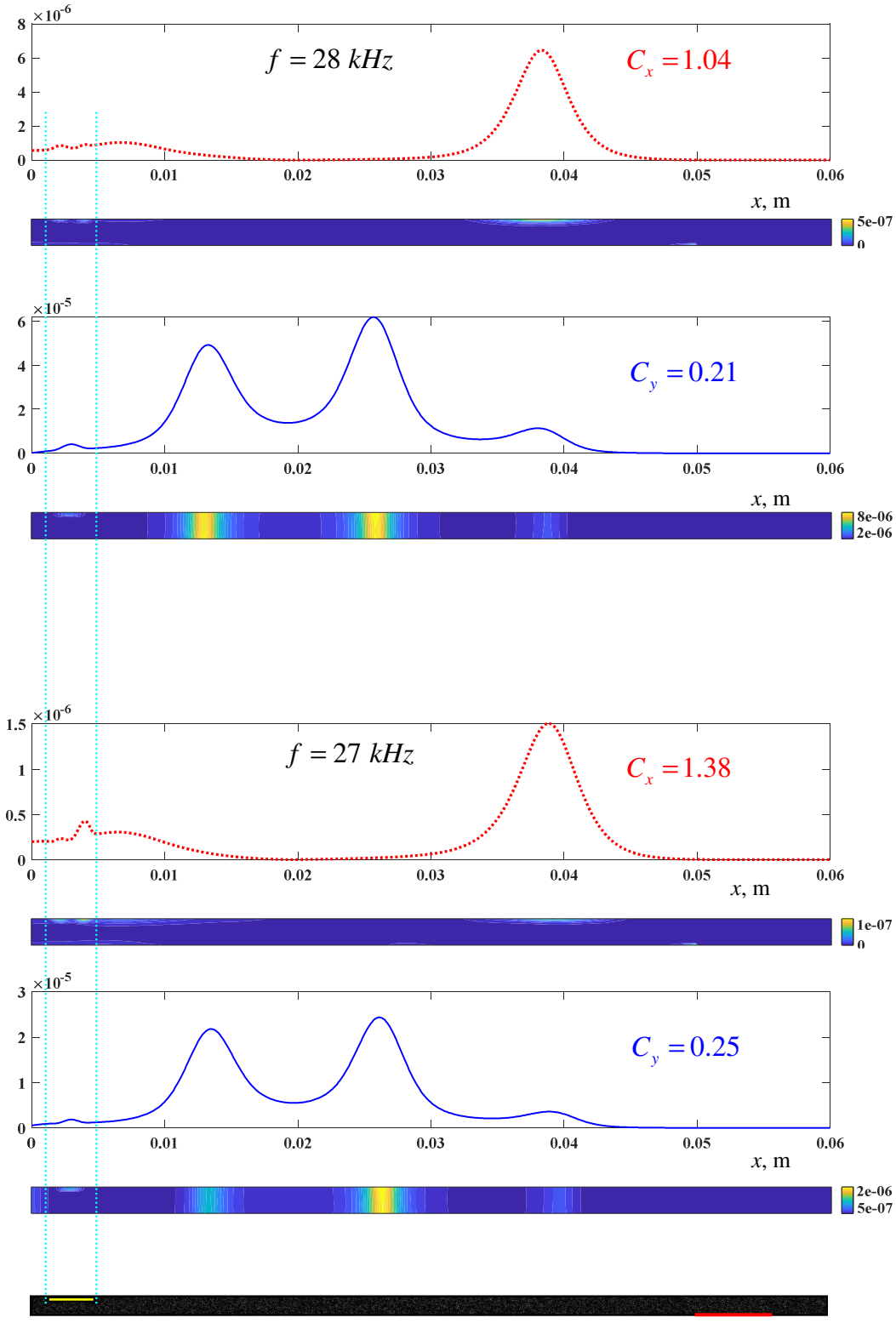

Fig. 12. Same as Fig. 10 but for excitation frequency 28 kHz and 27 kHz.

The encountered situation is further illustrated in Figs. 8 and 9 plotted in the same case as Figs. 6 and 7, but for the plate thickness of 2 mm instead of 3 mm. The MMD-FEM code is still functional at that high aspect ratio; however, a significantly altered structure of extenuative Lamb modes affects the result. Indeed, a crack at 0.5 mm depth becomes detectable, although with a strong parasite peak.

The last series of computations (Figs. 10-12) concerns the closest to the SLDV experiment geometry ever considered in this thesis. We investigated a sample with a height of 2 mm and length of 6 cm excited by harmonic signals with frequencies ranging from 100 kHz down to 27 kHz. The lowest frequency chosen if formally equal to the LDR frequency in the experiment presented in Section 1, although the structure of resonances in the modeled situation should be absolutely different. It can be seen that generally the defect is detectable under frequencies reasonable from the experimental point of view with the contrast of about 10^1-10^2. A comparison of Figs. 10-12 and Fig. 1 allows one to establish a qualitative conclusion between modeling and experiment. Potential further progress and the necessary actions are discussed in the concluding part of the thesis.

2.3. Conclusion

Initially, we downsized the geometry by a factor of 10 (Section 1, Chapter III), analyzing results across a frequency spectrum. Encouraged by satisfactory outcomes, we extended the sample length, exploring crack position with varying excitation sources with positive results.

In the subsequent step, we optimized the sample thickness to better approximate real plate dimensions and conducted simulations with the excitation source positioned at a significant distance. Successfully identifying shallow cracks, we lowered the excitation frequency to reach the low-frequency range while maintaining the same crack position. Despite variations in parameters compared to real experiments, our results demonstrated some satisfactory outcomes.

Discussion and perspectives

In the concluding part of the thesis, we draw general conclusions by outlining the conducted research actions and results, as well as discuss a numerous difficulties encountered. Then potential further progress is sketched; in that purpose, we identify additional factors that were neglected in the present study whereas the account for them can substantially improve things. Finally, this research can be placed in more a global context of a program that would lead from traditional detection of damage to novel modeling-assisted diagnostics-prognostics.

1. General conclusions

The **theoretical** part of this thesis is based on the semi-analytical contact model of the Cattaneo-Mindlin type i.e. applicable for axisymmetric or similar contact geometries with friction accounted for as the Coulomb friction law. An obvious conclusion should be made concerning the efficiently of the explicit local procedure of load-displacement boundary conditions calculation. Indeed, it does not require adjusting elastic fields in a neighborhood in order to satisfy the Coulomb friction condition at a given point.

As an **experimental** component, we enhanced the clarity on experimental in nonlinear laser vibrometry tests. By integrating [Seg-20]'s findings, we established key connections in terms of geometric similarities (in 2D) despite variations in simulation conditions. Segers's results, particularly concerning delamination in CFRP composite material, could have been detectable on both the shallow and deep sides of the sample with proper excitation through the LDR frequency. Since we did not specifically address the LDR frequency in our study, our primary focus is to align geometric criteria with Segers's work, marking the initial phase of our comprehensive investigation.

The principal part of the thesis concerns **numerical** modeling with the help of the MMD-FEM code. A vast variety of cases have been considered with parameters' values and conditions ranging from highly idealized to more and more realistic. It is important to note that due to numerous technical difficulties a gap in geometric parameters between modeling and experiment still remains. The most important difference is in the number of dimensions (2D modeling vs 3D experiment). However, with those remarks made, it is possible to establish a qualitative agreement at the level of synthetic and real nonlinear images of damage.

A particular feature of modeling results is related to generation of constant acoustic field i.e. zero harmonic for single frequency excitation. In the dual frequency numerical tests, strong

low frequency components also appear. A possible reason for that is the consideration of barely opened cracks those faces experience no prestress but touch each other at the entire interface length. Such a contact system “prefers” to stay in open state with no contact interaction rather than be stressed by the acoustic field. This highly pronounced bi-modality in the normal and related tangential responses can disappear once crack faces are prestressed at least partially.

From the **practical** point of view, a conclusion is the necessity of further efforts in the purpose of establishing more quantitative modeling-experiment agreement. An experimentally validated code opens a number of opportunities including better identification of crack properties or an eventual possibility to add a prognostics tool capable of predicting further evolution of damage.

2. Encountered difficulties and possible solutions

Certainly, our novel approach based on a physically plausible model of contact acoustic nonlinearity including interface roughness encounters a number of difficulties of essential and technical character. The essential issues are related to unknown conditions or factors which are accounted for in a simplified way for now.

2.1. Unknown factors

One of the important difficulties is unknown properties of the inner roughness represented here as parameter C. Indeed, in the absence of proper data, we use a value measured in a different case while the real magnitude can deviate substantially. Remember that C characterizes not roughness of a single crack face but composite roughness i.e. statistical properties of a random gap between faces. Additional mechanical measurements can help estimate this parameter for a given sample containing a crack.

Another problem we encountered is related to possible prestress of crack faces. In reality, even in the absence of external action, the crack surfaces are prestresses due to cracking process itself. Indeed, once separated, the crack faces will not be ideally conforming at the atomic scale, while globally they can match. This feature can be described as an appearance of a thin layer of material between the crack coasts or spontaneous thickening of material in vicinity of a crack. The thickness of this effective layer depends on an atomic-size mismatch and is to be evaluated separately. An attempt to virtually insert a sheet of material inside a delamination will result in clamping near the tips i.e. prestress application whereas at a central zone a nonzero aperture can appear. In the same way, for a surface breaking crack the atomic-scale mismatch will produce prestress at the crack tip while the part ending up at the surface

will open. This behavior is easily seen in images generated by the nonlinear phased array technique **[Oha-20]**.

Partial prestress can considerable decrease the intensity of the zero harmonic that reaches extremely high values (see Fig. 25 of Chapter III) in our modeling for barely open cracks. Indeed, distributed prestress means that some fragments of the crack will always be in contact, and the tendency for the system to "prefer" the contact loss state can disappear. At the same time, central fragments which are always open will not produce any nonlinear signal, same as strongly prestressed crack tips in which friction is disabled. All those effects depend on the crack size and the atomic mismatch level and should be evaluated to get more realistic description.

2.2. Technical issues

We also faced a bunch or technical difficulties related to limited computational resources, both in terms of calculation time and disk space. On a modern "average good" PC COMSOL files larger than 30-40 Gb are hard to process. The computation time is seriously affected by multiple switching between MATLAB and COMSOL calculations that drastically reduces the efficiency of MMD-FEM code in the current implementation. Programming in a unique environment e.g. using open source implementations of the Discontinuous Galerkin Method **[Hes-08]** can be a huge relief. Indeed, boundary conditions are set on a geometrical entity having one dimension less than the equation in volume and should not increase the calculation time considerably. Using the current MATLAB-COMSOL version of the code, calculations for a cracked sample are approximately 13-15 longer than for an intact one.

Besides, in the current MATLAB-COMSOL version there is a feature we encountered during the optimization stage and call boundary condition error (Fig. 11 of Chapter II). This error is coming from the fact that between the boundary condition and the same variables at the crack interface but processed by the FEM code in the volume there is an internal time stepping. To keep the boundary condition error low we have to use very dense mesh which can be made coarser otherwise as we do for intact samples. This inefficiency factor can also be dealt with by using a single programming environment.

The mentioned disadvantages of the current implementation give rise to a number of technical limitations. One of them is the difficulty of treating very long signals. Existing in numerical acoustics in general, this factor becomes important once stationary waves are considered which is required by the chosen methodology. To shorten the transient process, we are forced to limit ourselves to materials with high attenuation. Whereas in real experiments waiting for a second to make sure that the transient process is over is no problem at all, in modeling long

acoustic signals become hard to operate. High attenuation, in turn, leads to a situation different from the case of classical Lamb waves in plates and make the known analytical results hardly applicable, etc.

The relative inefficiency resulting from switching between two programming subsystems also makes if difficult to perform simulations in 3D which is necessary for a more qualitative modeling and experiment comparison.

3. Perspectives of computer assisted nonlinear acoustic imaging

In this thesis we made a step towards an experimental validation of the MMD-FEM modeling and established a qualitative agreement. Moving in the same direction and achieving a quantitative agreement would open new perspectives outlined below.

Suppose we have a validated code capable of producing synthetic nonlinear data for a known damage configuration. Then, by comparison of modeling and actual experimental data it would be possible to reconstruct damage in a more precise way. Indeed, experiments produce images that approximately indicate damage location and extent. More detailed information such as vector data on the measured fields or energy repartition between the generated harmonics is not used. Hypothetically, it would be possible to adjust the location, orientation, and extent of the crack to better match the available data ignored by the existing imaging methods. Generally speaking, it is expected that known link between damage and its measured signatures can help better reconstruct the former.

An obvious next step will not require nonlinear acoustic measurements or modeling but the applications of fracture mechanics methods. Once damage is identified, its further evolution in known conditions can be predicted by using modern methods describing crack growth under certain stresses or factors of environmental character. The creation of a prognostics tool on the basis of nonlinear acoustic imaging would complete the NDT strategy and produce a number of practical benefits.

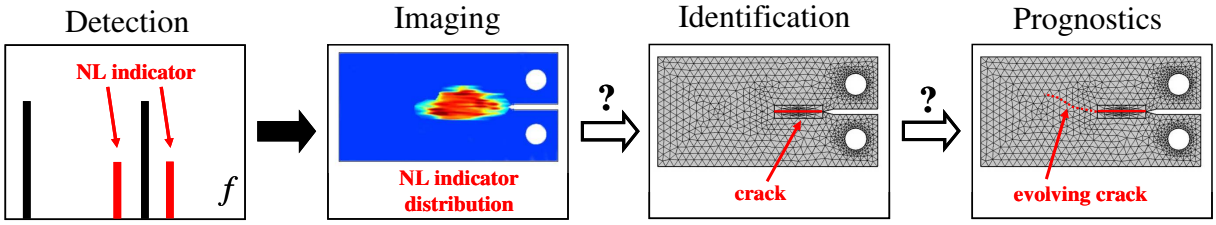

Fig. 1. A validated MMD-FEM tool can open new perspectives: known techniques of damage detection and imaging can be upgraded by adding a possibility of more precise damage identification followed by the creation of a prognostics tool using modern methods of fracture mechanics.

References

[Aki-75] Aki, K., Chouet, B., 1975. Origin of coda waves: Source, attenuation, and scattering effects, J. Geophys. Res., 80, 3322–3342.

[Ale-04] Aleshin, V., Gusev, V., Zaitsev, V., 2004. Propagation of acoustics waves of non-simplex form in a material with hysteretic quadratic nonlinearity: analysis and numerical simulations. J. Comput. Acoust., 12(3), 319–354.

[Ale-05] Aleshin, V., Van Den Abeele, K., 2005. Micro-potential model for stress-strain hysteresis of micro-cracked materials. J. Mech. Phys. Solids, 53(4), 795.

[Ale-07a] Aleshin, V., Van Den Abeele, K., 2007. Friction in unconforming grain contacts as a mechanism for tensorial stress-strain hysteresis. J. Mech. Phys. Solids, 55, 765–787.

[Ale-07b] Aleshin, V., Van Den Abeele, K., 2007. Microcontact-based theory for acoustics in microdamaged materials. J. Mech. Phys. Solids, 55, 366–390.

[Ale-08] Aleshin, V., Desadeleer, W.,Van Den Abeele, K., 2008. Characterization of hysteretic elasticity in materials using the integrated Preisach density. Int. J. Nonlin. Mech., 43, 151–163.

[Ale-15] Aleshin, V.V., Matar, O.B., Van Den Abeele, K., 2015. Method of memory diagrams for mechanical frictional contacts subject to arbitrary 2D loading. Int. J. Solids Struct., 60-61, 84–95.

[Ale-16] Aleshin, V.V.; Matar, O.B., 2016. Solution to the frictional contact problem via the method of memory diagrams for general 3D loading histories. Physical Mesomechanics, 19(2), 130-135.

[Ale-18] Aleshin, V.V., Delrue, S., Trifonov, A., Bou Matar, O., and Van Den Abeele, K., 2018. Two dimensional modeling of elastic wave propagation in solids containing cracks with rough surfaces and friction - Part I: theoretical background. Ultrasonics, 82, 11–18.

[Ale-19] Aleshin, V., Pylypenko, A., Truyaert, K., Delrue, S., Van Den Abeele. K., 2020. 3D modeling for acoustic waves and vibrations in solid structures with frictional cracks. Proceedings of Meetings on Acoustics, 38, 022003.

[Ale-20] Aleshin, V., 2020. On applications of semi-analytical methods of contact mechanics. Frontiers in Mechanical Engineering, 6, 30.

[Ale-23] Aleshin, V., Verma, R., Truyaert, K., 2023. Modeling for nonlinear acoustic imaging of an isolated crack via standing waves in a 2D solid. Ultrasonics, 133, 107023

[Bai-20] Bai, L., Velichko, A., Calre, A.T., Dryburgh, P., Pieris, D., Drinkwater, B.W., 2020. The effect of distortion models on characterisation of real defects using ultrasonic arrays. NDT & E International, 113, 102263.

[Bal-02] Ballad, E.M., Korshak, B.A., Solodov, I.Y., Krohn, N., Gusse, G., 2002. Local nonlinear and parametric effects for non-bounded contacts in solids. Nonlinear Acoustics at the Beginning of the 21st Century 2, 727-734.

[Biw-04] Biwa, S., Nakajima, S., Ohno, N., 2004. On the acoustic nonlinearity of solid-solid contact with pressure-dependent interface stiffness, J. Appl. Mech., 71(4), 508-515.

[Bla-14] Blanloeuil, P., Meziane, A., Bacon, C., 2014. Numerical study of nonlinear interaction between a crack and elastic waves under an oblique incidence. Wave Motion, 51 (3), 425–437.

[Bow-39] F. Bowden, D. Tabor, 1939. The area of contact between stationary and between moving surfaces, Proceedings of the Royal Society of London: Mathematical, Physical and Engineering Sciences, 169, 391–413.

[Can-21] Cantero-Chinchilla, S., Aranguren, G., Royo, J.M., Chiachio, M., Etxaniz, J, Calvo-Echenique, A., 2021. Structural health monitoring using ultrasonic guided-waves and degree of health index. Sensors, 21(3), 993.

[Car-08] G. Carbone, F. Bottiglione, 2008. Asperity contact theories: do they predict linearity between contact area and load? J. Mech. Phys. Solids, 56, 2555-2572.

[Cat-38] Cattaneo, C., 1938. Sul contatto di due corpi elastici: distribuzione locale degli sforzi. Rendiconti dell'Accademia Nazionale dei Lincei, 27, 342–348, 434–436, 474–478.

[Che-22] Chen, D., Huo, L., Song, G., 2022. High resolution bolt pre-load looseness monitoring using coda wave interferometry. Structural health monitoring, 21 (5), 1959-1972.

[Chi-10] Chigarev N., Gusev, V., 2010. Nonlinear frequency-mixing photoacoustic imaging of a crack: Theory. Journal of Applied Physics, 107, 124905.

[Cia-18] Ciampa, F., Mahmoodi, P., Pinto, F., Meo, M., 2018. Recent advances in active infrared thermography for non-destructive testing of aerospace components. Sensors, 18, 609.

[Dav-38] Davidenkov, N., 1938. Energy dissipation in vibrations. Journal of Technical Physics, 8(6).

[Del-18] Delrue, S., Aleshin, V.V., Truyaert, K., Bou Matar, O., Van Den Abeele, K., 2018. Two dimensional modeling of elastic wave propagation in solids containing cracks with rough surfaces and friction – Part II: Numerical implementation. Ultrasonics, 82, 19-30.

[Des-15] Desplanques, Y., 2015. Amontons-Coulomb friction laws, a review of the original manuscript. SAE International Journal of Materials and Manufacturing, 8, 98-103.

[Ehr-17] Ehrhardt, D.A., Allen, M.S., Yang, S., Beberniss, T.J., 2017. Full-field linear and nonlinear measurements using continuous-scan laser Doppler vibrometry and high speed three-dimensional digital image correlation. Mechanical Systems and Signal Processing, 86 (B), 82-97

[Fie-20] Fierro, G.P.M., Meo M., 2020. Non-linear phased array imaging of flaws using a dual and tri frequency modulation technique. Frontiers in Built Environment, 6, 68.

[Fin-00] Fink, M., Casssereau, D., Derode, A., Prada, C., Roux, P., Tanter, M., Thomas, J.L., Wu, F., 2000. Time-reversed acoustics. Reports on Progress in Physics 63, 1933.

[Gad-84] Gadala, M.S., Dokainish, M.A., Oravas, G.A., 1984. Formulation methods of geometric and material nonlinearity problems. International Journal for Numerical Methods in Engineering, 20(5), 887–914.

[Gal-61] Galin, L.A., 1961. Contact problems in the theory of elasticity. Raleigh, North Carolina State College.

[Gol-20] Golchinfar, B., Ramezani, M.G., Donskoy, D., Saboonchi, H., 2020. Vibro-Acoustic Modulation technique comparison with conventional nondestructive evaluation methods, Conference Paper: SPIE 11381, Health Monitoring of Structural and Biological Systems XIV, 113811W

[Gra-56] Granato, A., Lucke, K., 1956. Theory of mechanical damping due to dislocations. J. Appl. Phys., 27, 583–593.

[Gre-66] Greenwood, J.A., Williamson, J.B.R., 1966. Contact of nominally flat surfaces. Proc. Roy. Soc. London A, 295(1442), 300-319.

[Gus-05] Gusev, V.E., Tournat, V., 2005. Amplitude- and frequency- dependent nonlinearities in the presence of thermally-induced transitions in the Preisach model of acoustic hysteresis. Phys. Rev., 72.

[Guy-97] Guyer, R., McCall, K., Boitnott, G., Hilbert Jr, L.B., Plona, T., 1997. Quantitative implementation of preisach–mayergoyz space to find static and dynamic elastic moduli in rock. J. Geophys. Res., 102(B3), 5281–5293.

[Hal-06] Haller, K., Hedberg, C., 2006. Frequency sweep rate and amplitude influence on nonlinear acoustic measurements. 9th Wespac Seoul, Korea.

[Hau-17] Haupert, S., Renaud, G., Schumm, A., 2017. Ultrasonic imaging of nonlinear scatterers buried in a medium, NDT&E International, 87, 1-6.

[Hau-19] Haupert S., Ohara, Y., Carcreff, E., Renaud, G., 2019. Fundamental wave amplitude difference imaging for detection and characterization of embedded cracks. Ultrasonics, 96, 132-139.

[Hel-01] Helbig, K., Rasolofosaon, P.N.J., 2001. A theoretical paradigm for describing hysteresis and nonlinear elastricity in arbitrary anisotropic rocks. Anisotropy 2000. Soc. Expl. Geophysics, 6, 383–398.

[Her-17] Ehrhardt, D.A., Allen, M.S., Yang, S., Beberniss, T.J., 2017. Full-field linear and nonlinear measurements using Continuous-Scan Laser Doppler Vibrometry and high speed Three-Dimensional Digital Image Correlation. Mechanical Systems and Signal Processing, 86, 82-97.

[Hes-08] Hesthaven, J.S., Warburton, T., 2008. Nodal discontinuous Galerkin methods. Springer Science+Business Media, LLC.

[Hon-20] Honarvara, F., Varvani-Farahani1, A., 2020. A review of ultrasonic testing applications in additive manufacturing: Defect evaluation, material characterization, and process control. Ultrasonics 108 (2020) 106227

[Hyu-07] S. Hyun, M. Robbins, 2007. Elastic contact between rough surfaces: Effect of roughness at large and small wavelengths, Tibol. Int., 40, 1413–1422.

[Jäg-95] Jäger, J, 1995. Axi-symmetric bodies of equal material in contact under torsion or shift Archive of Applied Mechanics, 65, 478-487.

[Jäg-98] Jäger, J., 1998. A new principle in contact mechanics. J. Tribol., 120(4), 677-684.

[Jäg-05] Jäger, J., 2005. New solutions in contact mechanics. WIT Press, Southampton.

[Jha-20] Jhang, K.Y., Lissenden, C.J., Solodov, I., Ohara, Y., Gusev, V., 2020. Measurement of nonlinear ultrasonic characteristics. Springer series in measurement science and technology, Singapore.

[Kal-88] Kalker, J. J., 1988. Contact mechanical algorithms. Communications in applied numerical methods, 4, 25-32.

[Kho-13] Khoei, A.R., Eghbalian, M., Moslemi, H., Azadi, H., 2013. Crack growth modeling via 3D automatic adaptive mesh refinement based on modified-SPR technique. Appl. Math. Modelling, 37, 357-383.

[Kra-89] Krasnosel'skii, M.A., Pokrovskii, A.V., 1989. Systems with Hysteresis. Springer.

[Lan-93] Landau, L.D., Lifshitz, E.M., 1993. Theory of elasticity. Pergamon Press, Oxford.

[Law-98] Lawn, B.R., Marshall, D.B., 1998. Nonlinear stress–strain curves for solids containing closed cracks with friction. J. Mech. Phys. Solids, 46(1), 85–113.

[Lee-21] Lee, Y., Cho, Y., 2021. Defect Imaging Enhancement through Optimized Shape Factors of the RAPID Algorithm Based on Guided Wave Beam Pattern Analysis. Sensors 2021, 21, 4029.

[Len-24] Lennard-Jones, J.E., 1924. On the determination of molecular fields. Proc. R. Soc. Lond. A, 106(738), 463–477.

[Liv-18] LiveLink™ forMATLAB® User's Guide© 2009–2018 COMSOL

[Loi-22] Loi G., Aymerich, F., Porcu, M.C., 2022. Influence of sensor position and low-frequency modal shape on the sensitivity of vibro-acoustic modulation for impact damage detection in composite materials. J. Compos. Sci., 6(7), 190.

[Maj-91] Majumdar, A., Bhushan, B., 1991. Fractal model of elastic-plastic contact between rough surfaces, Journal of tribology, 113/1.

[Mar-19] Martens, A., Kersemans, A., Daemen, J., Verboven, E., Paepegem, W.V., Delrue, S., Van Den Abeele K., 2019. Characterization of the orthotropic viscoelastic tensor of composites using the Ultrasonic Polar Scan. Composite Structures, 230, 111499.

[May-85] Mayergoyz, I.D., 1985. Hysteresis models from the mathematical and control theory points of view. J. Appl. Phys., 57(1), 3803–805.

[May-88] Mayergoyz, I.D., 1988. Vector preisach hysteresis models (invited). J. Appl. Phys., 63, 2995.

[Mez-20] Meznil, S., Chigarev, N., Tournat, V., Gusev, V.E., 2020. Nonlinear frequency-mixing photoacoustic characterisation of a crack. In book: Measurement of Nonlinear Ultrasonic Characteristics, 235-281.

[Min-53] Mindlin, R.D., Deresiewicz, H., 1953. Elastic spheres in contact under varying oblique forces. J. Appl. Mech., Trans. ASME 20, 327–344.

[Mun-94] Munisamy, R. L., Hills, D. A., and Nowell, D., 1994. Static axisymmetrical Hertzian contacts subject to shearing forces. ASME J. Appl. Mech., 61, 278–283.

[Naz-89] Nazarov, V., Sutin, A., 1989. Harmonic generation in the propagation of elastic waves in nonlinear solid media. Sov. Phys. Acoust., 35,410–413.

[Naz-03] Nazarov, V.E., Radostin, A.V., Ostrovsky, L.A., Soustova, I.A., 2003. Wave processes in media with hysteretic nonlinearity. part i. Acous. Phys., 49, 344–353.

[Naz-09] Nazarov, V.E., Kolpakov, A.B., Radostin, A.V., 2009. Amplitude dependent internal friction and generation of harmonics in granite resonator. Acoustical Physics, 55, 100–107.

[Nih-00] Nihei, K.T., Hilbert Jr, L.B., Cook, N.G.W., Nakagawa, S., Myer, L.R., 2000. Frictional effects on the volumetric strain of sandstone. Inter. J. Rock Mech. Min. Sci., 37, 121–132.

[Oha-19] Ohara, Y., Nakajima, H., Tsuji, T., Mihara, T., 2019. Nonlinear surface-acoustic-wave phased array with fixed-voltage fundamental wave amplitude difference for imaging closed cracks. NDT & E International, 108, 102170.

[Oha-20] Ohara, Y., Remillieux, M.C., Onuma, T., Tsunoda, K., Tsuji, T., 2020. Toward an ultra-high resolution phased-array system for 3D ultrasonic imaging of solids. Applied Physics Letters, 117, 111902.

[Ost-91] Ostrovsky, L.A., 1991. Wave processes in media with strong acoustic nonlinearity. J. Acoust. Soc. Am., 90(6), 3332–3337.

[Ost-01] Ostrovsky, L.A., Johnson, P.A., 2001. Dynamic nonlinear elasticity in geomaterials. Rivista del Nuovo Cimento, 24(7), 1–46.

[Pag-10] M. Paggi, M. Ciavarella, 2010. The coefficient of proportionality between real contact area and load, with new asperity models, Wear, 268, 1020–10.

[Pag-14] M. Paggi, R. Pohrt, V. Popov, 2014. Partial-slip frictional response of rough surfaces, Scientific Reports, 4, 5178.

[Pap-15] Papangelo, A., Ciavarella, M., 2015. Cattaneo–Mindlin planeproblemwithGriffith friction, Wear, 342-343, 398–407

[Per-02] Persson, B., Bucher, F, Chiaia, B., 2002. Elastic contact between random rough surfaces: Comparison of theory with numerical results, Phys. Rev. B, 65(18), 184106.

[Pfl-04] Pfleiderer, K., Stoessel, R., Solodov, I., Busse, G., 2004. Acoustic imaging with surface and lamb waves for NDE and material characterisation. In: Arnold, W., Hirsekorn, S. (eds) Acoustical Imaging. Acoustical Imaging, 27, Springer, Dordrecht.

[Poh-12] Pohrt, R., Popov, V., 2012. Normal contact stiffness of elastic solids with fractal rough surfaces. Phys. Rev. Lett., 108, 104301.

[Poh-13] Pohrt, R., Popov, V., 2013. Contact stiffness of randomly rough surfaces. Scientific Reports, 3, 3293.

[Pop-15] Popov, V.L., Heß, M., 2015. Method of dimensionality reduction in contact mechanics and friction. Springer Heidelberg New York Dordrecht, London.

[Pre-35] Preisach, F., 1935. Über die magnetische nachwirkung. Z. Phys., 94, 277.

[Ras-98] Rashid, M.M., 1998. The arbitrary local mesh replacement method: An alternative to remeshing for crack propagation analysis. Computer Methods in Appl. Mech. Engg., 154, 133-150.

[Rot-17] Rothberg S.J., Allen, M.S., Castellini, P., Maio, D.D., Dirckx, J.J.J., Ewins, D.J., Halkon, B.J., Muyshondt, P., Paone, N., Ryan, T., Steger, H., Tomasini, E.P., Vanlanduit, S., Vignola, J.F., 2017. An international review of laser Doppler vibrometry: Making light work of vibration measurement. Optics and Lasers in Engineering, 99, 11-22.

[Seg-20] Segers, J., Hedayatrasa,S., Poelman, G., Van Paepegem, W., Kersemans, M., 2020. Backside delamination detection in composites through local defect resonance induced nonlinear source behavior. Journal of Sound and Vibration, 479, 115360.

[Seg-21] Segers, J., & Hedayatrasa, S., & Kersemans, M., 2021. Full-field elastic wave imaging and processing for non-destructive inspection of fiber-reinforced polymers. Ghent University, Faculty of Engineering and Architecture.

[Sha-94] Sharma, M.M., Tutuncu, A.N., 1994. Grain adhesion hysteresis: a mechanism for attenuation of seismic waves. Geophys. Res. Lett., 21(21), 2323–2326.

[She-12] Sheen B., Cho Y., 2012. A study on quantitative lamb wave tomogram via modified RAPID algorithm with shape factor optimization. Int. J. Precis. Eng. Manuf., 13, 671-677.

[Sma-20] Smagin, N., Trifonov, A., Bou Matar, O., Aleshin, V., 2020. Local damage detection by nonlinear coda wave interferometry combined with time reversal. Ultrasonics, 109, 106226.

[Sne-51] Sneddon, I., 1951. Fourier Series. Routledge & Kegan Paul, New York.

[Sni-02] Snieder, R., Grêt, A., Douma, H., Scales, J., 2002. Coda wave interferometry for estimating behavior in seismic velocity. Science, 295, 2253–2255.

[Sol-02] Solodov, I., Krohn, N., Busse, G., 2002. An example of non-classical acoustic nonlinearity in solids. Ultrasonics, 40, 621–625.

[Sol-04] Solodov, I., Wackerl, J., Pfleiderer, K., Busse, G., 2004. Nonlinear self-modulation and subharmonic acoustic spectroscopyfor damage detection and location. Appl. Phys. Lett. 84, 5386–5388.

[Sol-11] Solodov, I., Bai, J., Bekgulyan, S., Busse, G., 2011. A local defect resonance to enhance acoustic wave-defect interaction in ultrasonic nondestructive evaluation. Appl. Phys. Lett., 99, 211911.

[Sol-13] Solodov, I., Bai, J., Busse, G., 2013. Resonant ultrasound spectroscopy of defects: Case study of flat-bottomed holes. J. Appl. Phys., 113(22).

[Sol-19] Solodov I., Kreutzbruck M., 2019. Mode matching to enhance nonlinear response of local defect resonance. Journal of Sound and Vibration, 461, 114916.

[Sol-20] Solodov I., Kreutzbruck M., 2020. Ultrasonic frequency mixing via local defect resonance for defect imaging in composites. Ultrasonics, 108, 106221.

[Tal-79] Tallon, J.L., Wolfenden, A., 1979. Temperature dependence of the elastic constants of aluminum. Journal of Phy. and Chem. of Solids, 40(11), 831-837.

[Ter-21] Terzi, M., Chehami, L., Moulin, E., Smagin, N., Aleshin, V., 2021. Reference-free damage localization based on pump-probe measurements. e-Forum Acusticum, Lyon, France, 67-72.

[Tor-02] Torre, E.D., Bennett, L.H., Fry, R.A., Ducal, O.A., 2002. Preisach-arrhenius model for thermal aftereffect. IEEE Transactions on Magnetics, 38(5), 3409–3416.

[Tri-17] Trifonov, A., 2017. Nonlinear acoustic nondestructive testing for aeronautical applications. Central Lille, Micro and Nano Technologies, Acoustics, and Telecommunications.

[Tru-22] Truyaert, K., Aleshin, V., Van Den Abeele, K., 2022. Qualitative analysis of a 3D multiphysics model for nonlinear ultrasonics and vibration induced heating at closed defects. Research in nondestructive evaluation, 33:1, 17-32.

[Vak-05] Vakhnenko, O.O., Vakhnenko, V.O., Shankland, T.J., 2005. Soft-ratchet modelling of end-point memory in the nonlinear resonant response of sedimentary rocks. Phys. Rev., 71.

[Van-00] Van Den Abeele, K., Carmeliet, J., Ten Cate, J.A., Johnson, P.A., 2000. Nonlinear elastic wave spectroscopy (NEWS) techniques to discern material damage, part II: Single-mode nonlinear resonance acoustic spectroscopy. Research in Nondestructive Evaluation, 12, 31–42.

[Van-12] Van Den Abeele, K., Delrue, S., Haupert, S., Aleshin, V., 2012. Modeling nonlinear response from distributed damage and kissing bonds. Proceedings of meetings on acoustics, 16.

[Vol-23] User guide for CONTACT, Rolling and sliding contact with friction Technical Report20-01, version ‘v23.1’DateMay 1, 2023Author(s)Dr.ir. E.A.H. Vollebregt

[Whi-70] Whitehouse, D.J., Archard, J.F., 1970. The properties of random surfaces of significance in their contact, Proc. Roy. Soc. Lond A., 316, 97-121.

[Wri-13] Wright, J.R., Armitage, P.R., Mottram, T.D., 2013. Non-linear acoustics techniques for NDT. Theta technologies ltd. innovation centre, Rennes drive, Exeter, UK.

[Yan-98] Yan, W., Komvopoulos, K., 1998. Contact analysis of elastic-plastic fractal surfaces, Journal of Applied Physics, 84, 7.

[Yas-13] Yastrebov, V.A., 2013. Numerical methods in contact mechanics. A book published printed by ISTE Ltd and John Wiley & Sons, Inc.

[Yua-15] M. Yuan, J. Zhang, S. Song, H. Kim, 2015. Numerical simulation of Rayleigh wave interaction with surface closed cracks under external pressure. Wave Motion, 57, 143–153.

[Zha-17] Zhang, Y., Tournat, V., Abraham, O., Durand, O., Letourneur, S., Le Duff, A., Lascoup, B., 2017. Nonlinear coda wave interferometry for the global evaluation of damage levels in complex solids. Ultrasonics, 73, 245-252.

[Zhu-40] Zhuravlev, V.A., 1940. On the question of theoretical justification of the Amontons–Coulomb law for friction of unlubricated surfaces. Journal of Technical Physics, 10 (17), 1447–1452.